

**The effect of thermal fluctuations
on
elastic instabilities of biopolymers**

**The effect of thermal fluctuations
on
elastic instabilities of biopolymers**

PROEFSCHRIFT

ter verkrijging van de graad
van Doctor aan de Universiteit Leiden
op gezag van Rector Magnificus
prof. mr . P. F. van der Heijden,
volgens besluit van het College voor Promoties
te verdedigen op 4 Juli 2012
klokke 4:15 uur

door

Marc David Emanuel

geboren te Den Haag in 1958

Promotiecommissie:

Promotor : Prof. dr. H. Schiessel

overige leden : Prof. dr. E. Frey

Ludwig-Maximilians-Universität München

Prof. dr. T. Odijk

Delft University of Technology

Dr. V. Vitelli

Prof. dr. E.R. Eliel

Typeset in L^AT_EX fonts: Times NR with MathTime pro2 lite
Cover design by **æmi**, (www.aemi.nl)

Casimir PhD series, Delft-Leiden 2012-17
ISBN 978-90-8593-128-7

Contents

1	Introduction	1
2	On the organization of DNA in eukaryotes	7
2.1	Introducing DNA in its environment	7
2.2	The 30 nm chromatin fiber	8
2.2.1	Old models	9
2.2.2	Ribbon model	9
2.2.3	Energetics: elasticity and electrostatics	12
2.2.4	Energetics: Nucleosome attraction	12
2.2.5	The 30 nm fiber <i>in vivo</i>	13
2.2.6	Conclusion: the 30 nm fiber	14
2.3	Large scale structures	14
2.3.1	Experiments and models	14
2.3.2	The loop and the globule	15
2.3.3	Conclusion: large scale structure	20
2.4	Mechanism behind compactification	21
2.4.1	Enclosure	21
2.4.2	Specific binding sites	21
2.4.3	Non specific compactification	22
2.5	Conclusion	24
3	Euler Buckling	27
3.1	Motivation	27
3.2	The Partition Sum of a WLC under Compression	29
3.3	Euler buckling	30
3.4	Semiclassical Buckling	32
3.4.1	Harmonic fluctuations below the Euler transition	33
3.4.2	Harmonic fluctuations above the Euler transition	35

3.5	Quartic order	42
3.6	Comparison with the simulation	45
3.7	Discussion	47
4	The Writhe of a Curve	49
5	Plectoneme formation of double-stranded DNA under torsion	57
5.1	Motivation	57
5.2	The mechanistic Plectoneme	58
5.3	Linear elasticity	60
5.4	The Plectoneme	65
5.4.1	Geometry	65
5.4.2	Elasticity	66
5.4.3	Electrostatics	67
5.4.4	Summing up	69
6	Free energy of a confined worm like chain under torsion	71
6.1	Chain under tension	71
6.2	Confined chain: isotropic case	75
6.3	Non isotropic confinement	83
6.3.1	Almost isotropic case	85
6.3.2	Strong anisotropy	87
7	Thermal Fluctuations and the Multi-Plectoneme Phase	91
7.1	Short wave length fluctuations	92
7.2	Instantons	98
8	Comparison with experiments and conclusions	103
8.1	Conclusions	113
A	Elliptic functions and the generalized Lamé equation	115
A.1	Elliptic functions	115
A.2	Solving the generalized Lamé equation	116
B	Writhe of a plectoneme	121
C	Thermal fluctuations and plectonemes	125
C.1	Fluctuations of the strands in a plectoneme	125
C.2	Multi-plectoneme Entropy	126
D	Matlab code	129
	Bibliography	141

List of Tables	157
-----------------------	------------

List of Figures	159
------------------------	------------

Marc groet 's morgens de dingen

*Dag ventje met de fiets op de vaas met de bloem
ploem ploem
dag stoel naast de tafel
dag brood op de tafel
dag visserke-vis met de pijp
en
dag visserke-vis met de pet
pet en pijp
van het visserke-vis
goeiendag*

Daa-ag vis

*dag lieve vis
dag klein visselijn mijn
— Paul van Ostaijen*

Chapter 1

Introduction

This introductory chapter does not try to be complete in any sense. Neither is it original since all material is covered in many of the excellent books available [1, 2, 3, 4, 5]. The main purpose is to set some of the background that has influenced my research. And to highlight some points in polymer physics that sometimes are neglected.

Polymers have intrigued physicists and physical chemists for a long time, partly because they bring the molecular origin of matter become closer to our reality. The models that have been developed, and this is a theme that can be seen as a red thread throughout this thesis, have to cope with interactions between extended objects, that are all of the order of the thermal energy, $\beta^{-1} = k_B T$. It is this interweaving of interactions, over varying distances, with the thermal environment that makes this field surprisingly complex, and from the earliest models to the deep connections to spin systems, field theories and thermo elastic theories, new concepts had to be created to be able to find the right language, and degrees of freedom, that make a treatment possible. In this introduction we will touch upon a few of them to illustrate this.

The first polymer revolution came from Paul Flory, who introduced a new way to look at the swelling of polymers [6]. The starting point was the concept of a random walk of N segments of length b . Since a true random walk does not remember its previous step, it describes a flexible polymer of contour length $L_c = Nb$. One of the easy properties to calculate is the average size of the chain as function of the number of segments. Symmetry makes all odd moments disappear, so we use the square root of the 2nd moment as a measure of its size. Since the probability distributions of segment orientations, given as a unit vector \mathbf{r} , are by assumption independent, the end to end distance is a simple probability calculation

$$\sqrt{\langle \mathbf{R}^2 \rangle} = \left\langle \left(\sum_{i=1}^N b \mathbf{r}_i \right)^2 \right\rangle^{1/2} = b \left(\sum_{i,j=1}^N \langle \mathbf{r}_i \cdot \mathbf{r}_j \rangle \right)^{1/2} = bN^{1/2} \quad (1.1)$$

and we find the well known result that the size scales with the square root of the number of segments. In general the monomers, the polymer building blocks, have links that are not that flexible and in most biopolymers there is on the monomer level hardly any flexibility left. In that case one natural choice is the Kuhn length, a segment length on a length scale that equals the directional correlation length. The probability distribution of the end to end distance will have a Gaussian distribution with variance given by the expectation value of the extension squared (1.1). This is the central limit theorem, which one can understand considering the entropy of the sum of a large number of random segment-orientations. The Gaussian distribution is the distribution that maximizes the entropy [7] for a given standard deviation. The intuitive reason is simply that there are only two parameters that determine the distribution: the mean and the standard deviation. Any other distribution will necessarily have more parameters and thus contains more information. The resulting probability distribution of end to end distance is apparently given by:

$$P(\mathbf{R}) = \mathcal{N} \exp\left(-3 \frac{\mathbf{R}^2}{2Nb^2}\right), \quad (1.2)$$

\mathcal{N} is for normalization, the factor 3 because we consider the chain in 3 dimensions. There are 2 remarkable properties of this distribution. The first is the scale invariance: dividing the segment length by some factor while multiplying the number of segments by that factor *squared* does not change the distribution, although the contour length increases by that same factor. To define a point in the coil, its distance along the contour from the start is not an invariant concept as long as we are not interested in the properties on a local scale, but the variance at that point is. Think of this as an n dimensional lattice. When we rescale the length of the lattice unit, it is the 2 dimensional lattice that describes the coil. The scaling dimension is 2. This

A second point is the interpretation of equation (1.2) as a Boltzmann factor. The argument of the exponent represents a harmonic potential with a “spring constant” of $3k_B T/(b^2 N)$. What is remarkable is that it increases with temperature. The reason is that the apparent resistance, against a force that squeezes or stretches the coil, is of purely entropic nature. It explains why a rubber strip, stretched by a weight, shrinks when it gets heated. Other examples of “entropic interactions” are depletion, in its most basic form the force that pushes colloids together in a dilute solution of polymers [8], repulsion of the two strands in a plectoneme see Chapter 7, and in the recently put forward theory of gravity as an emergent force [9].

A random walker has no mechanism that stops it from traversing the same point twice. A polymer, being a physical object all along its path can not do this. We have to change the model to that of a self avoiding random walk (SAW). But traversing the path and knowing which point is already occupied by a random walker is a very nonlocal thing to do as seen from the perspective of the walker. As a result the coil will swell. The relation we found between the size of the coil and the number of segments (1.1) will change. The precise value will depend on the interactions between the segments, but if they are effectively of short

range, as compared to the chain length, we expect a relation of the form: $R \sim N^\nu$, with the exponent ν somewhere in between $1/2$ (random walk) and 1 (stretched chain). A logical step to describe the interactions is a self consistent mean field way. This is what Flory did. He considered the monomers of the chain as an ideal gas in an average repulsive potential caused by the other monomers. The stabilizing factor is the previously introduced harmonic spring. We perform the calculations in d -dimensions. The entropic spring potential does not change except for a prefactor. Writing the reduced¹ free energy as the sum of the 2 opposing contributions and minimizing with respect to R , omitting numerical prefactors :

$$\beta \frac{d\mathcal{F}(R)}{dR} = \frac{d}{dR} \left(Nv \frac{N}{R^d} + \frac{R^2}{N} \right) = 0 \Rightarrow R \sim N^{3/(d+2)} \quad (1.3)$$

where v is the excluded volume, actually a second virial coefficient, setting the strength of the interaction. It has the dimensions of a volume so it can be seen as the volume that a segment is excluded from due to the presence of other segments. In case it turns negative the chain will finely collapse into a globule, although in that case other virial coefficients have to be included. In this introduction we will consider only chains with repulsive interactions. We find the Flory exponent of a SAW of $3/(d+2)$. For 1 dimension it is obviously exact since the stretched chain is the only configuration.

For dimensions higher then 4 the exponent would be lower than the random coil one. Thermal fluctuations will dominate and the exponent will stick at $1/2$. It is instructive to pause a bit to understand this better from the free energy point of view. Replacing R by N^ν in the repulsive term of equation (1.3) we find an energy contribution that scales with $N^{2-d\nu}$. Since $\nu \geq 1/2$ we see that for $d > 4$ and a long enough chain it will be smaller than the thermal energy. This can be seen as a golden rule when making this kind of scaling arguments: always compare contributions to the thermal energy. One can also understand this in a geometrical way: we have seen that the random coil is like a $2d$ object. The subspace of configurations where 2 of them intersect in a 5- or higher dimensional Euclidean space has measure 0, loosely speaking because there are always directions in which any movement will tear them apart.

In 4 dimensions the exponent does not seem to be affected although the excluded volume can not be neglected.

For us the 2 and 3 dimensional cases are the most important and here the Flory argument seems to work surprisingly good. From renormalization group calculations one finds in $3d$ $\nu \simeq 0.589$ [10] as compared to the Flory result : $\nu = .6$. In 2-dimensions the Flory exponent coincides with the exact result as calculated from conformal field theory [11]. It is somewhat surprising that the exponents are this good, since chain connectivity affects both the repulsive and the attractive term in the free energy. In the repulsive part the ansatz was that the density of segments around a segment is the average density. Normally in mean field theory this assumption is not valid because of short scale correlations. For a polymer the situation is

¹reduced free energy is the free energy scaled by the the thermal energy

more severe. Because of the connectivity of the chain is the density around a segment not only lower because of its own presence, but also because of the segments to which it is directly connected. This overestimation of the repulsive energy gets canceled by the overestimation of the entropic contribution. The presence of other segments considerably decreases the number of configurations and so does its change upon expansion. The almost exact cancellation of the two errors is coincidental.

These last mentioned precise calculations were based on a correspondence found [12] between $O(n)$ spin systems and SAW's in the limit $n \rightarrow 0$, by noting that the expansion of the Laplace transform of the total number of chains on a lattice had the same diagrammatic structure as Wilson's ϵ -expansion of a spin model on the lattice [13] when one sets n to zero. In a way for $n=1$, the Ising model, it was already known for a long time that the partition sum could be written as a summation over closed loops on the lattice where each edge could be traversed only once. On a square lattice this means that vertices can be visited twice.

The success of scaling theories where a polymer is viewed as a critical system, has been directing the field since. Especially the beautiful exposition by deGennes [1] has led to the belief that everything could be calculated using scaling arguments. There is a danger that these scaling arguments are wrong for the same reason Flory's argument breaks down in dimensions larger than 4, namely that terms taken into account have an energy below the thermal energy.

When Watson and Crick discovered the structure of double stranded DNA [14], later followed by actin, microtubules and others, it was immediately clear that an understanding of polymer physics is crucial in biology. What all these biopolymers have in common is that on the monomer scale they are very stiff losing their directional correlation over a distance that is long compared to the monomer size. Since the molecule is resistant against bending the right description is to lowest order one of linear elasticity, the worm like chain model (WLC). Originally it was set up [15] as limit of a chain where only the angle between neighboring segments tangents is fixed. Since that leaves the freedom for one segment to rotate around the axis of the other it is called a freely rotating chain. The limit is now taken where the segment size and the angle between neighboring tangents go to zero, while increasing at the same time the number of segments in such a way that Nb and b/θ^2 stay constant. The first limit keeps the contour length constant, the second the angle-angle correlation length. The model was created to explain the röntgen diffraction measurements when changing from small angles to large angles and is often named after their discoverers the Kratky-Porod chain. For a long time the WLC was not considered to be very useful mainly because it does not directly relate to a critical system. It was considered more practical to use a Gaussian model that comes close in reproducing the WLC behavior [2]. Using as parametrization the contour length s , one defines the persistence length, P_b , as the length scale of exponential decay of the tangent-tangent correlation function:

$$\langle \mathbf{t}(s_1) \mathbf{t}(s_2) \rangle = \exp\left(-\frac{|s_1 - s_2|}{P_b}\right) \quad (1.4)$$

It is straightforward to integrate this equation twice over the contour length to find that for large lengths the coil size is $R = \sqrt{2L_c P_b}$. But that is the equation for a random coil with Kuhn length $2P_b$ and $L_c/(2P_b)$ segments. Although at scales long enough it behaves as a flexible chain, a large difference between chain diameter and Kuhn length makes the excluded volume relatively small in the following sense: as was shown in a famous paper by Onsager [16], a long slender rod, with diameter d and length P_b has a 2nd virial coefficient of $\sim d P_b^2$. We want to find the contour length up to which excluded volume can be neglected. The volume of the coil is $R^3 = (P_b L_c)^{3/2}$ and demanding the first term in the reduced free energy of equation (1.3) to be 1 results in a contour length of $L_c = d^2/P_b$. DNA for example has a diameter of 2 nm and a persistence length of 50 nm. It starts to feel excluded volume effects only for contour lengths above 30 μm or almost 100.000 base pairs. This is in a good solvent and a dilute solution, but it shows how one should take care in treating semi flexible polymers as being flexible. In the first chapter, based on a review that appeared in Physical biology [17] we will give an overview of our understanding of some of the physics of DNA in the eukaryotic cell. It covers aspects on the basepair level, the persistence length scale, and on the large scale level where questions on the influence of excluded volume become essential. As a final warning: in most calculations we will be rescaling energies by the thermal energy. The forces have as a consequence the dimension of $[\text{nm}^{-1}]$.

²we don't care here about the precise numerical factors

On the organization of DNA in eukaryotes

2.1 Introducing DNA in its environment

The human genome contains approximately $6 \cdot 10^9$ basepairs, two copies of which lead to roughly 2 meters DNA per cell. On scales larger than the helical repeat length, 3.5 nm, the double helix is well described as a wormlike chain with a persistence length of about 50 nm. Disregarding volume interactions the diameter of the coil in a theta solvent would be around $\sqrt{2 \times 50\text{nm} \times 2\text{m}} \approx 450 \mu\text{m}$. That is an order of magnitude larger than the $10 \mu\text{m}$ diameter of the nucleus of a typical cell in which the DNA is always confined.

As a first level of organization the eucaryotic DNA is wrapped around protein spools, each a cylindrical wedge of diameter of 6 nm and maximal height of 6 nm. About 147 basepairs wrap along a left-handed wrapping path of 1,67 turns around the octamer. These spools are composed of 4 pairs of histone proteins, named H2A, H2B, H3 and H4. This octamer, together with the DNA wrapped around, is called the nucleosome core particle (NCP). Its structure is known in great detail from high resolution X-ray crystallography [18]. It is noteworthy to mention that the histone proteins that make up the core, although existing with some variations, are remarkably well conserved between eukaryotes. An important feature of the histones are their tails, flexible positively charged extensions. Through modifications, like acetylation and phosphorylation, it is possible to neutralize charges on the tails. These modifications form a way to regulate the organization of the DNA in the nucleus, as we will discuss in the next sections. There are also other modifications, that do not directly influence the spatial distribution of DNA but influence the binding of proteins. We will not consider them in this thesis. For a discussion of the energetics and dynamics involved in single nucleosomes we refer to other reviews [19, 20].

There is one spool for every 160 to 240 basepairs. This so called repeat length varies over species, but also over cells within one species. The stretches of DNA connecting two neighboring NCPs is called linker DNA. As a result one obtains a bead-on-a-string structure, sometimes referred to as 10 nm fiber. This structure is, however, only observed *in vitro* at

subphysiological salt concentrations. If we nevertheless assume that such a fiber exists in the nucleus with the same stiffness as for naked DNA, then we find a coil diameter of around $\sqrt{50/200} \times 450 \mu\text{m} \approx 225 \mu\text{m}$ – a value that is still much larger than the diameter of the nucleus.

In most eukaryotes a fifth histone is thought to bind the two outgoing double strands at each NCP resulting in a denser structure. From EM measurements it is concluded that the linker histone assembles the two outgoing strands in a stem of 3 nm length [21]. This linker histone has a couple of variants (named H1 and H5), but is also very well conserved. That all the histone proteins are so well conserved through evolution indicates that their functional properties are rather intricate. In the presence of linker histones and for physiological salt concentrations one observes dense fibers, usually referred to as 30 nm or chromatin fibers, that are known through *in vitro* experiments for over 30 years. They typically feature around 30 nm diameter, independent of whether they are extracted from cells or whether they are reconstituted. These fibers have a contour length that is only about 1/50th of the contour length of the DNA that it contains but seem to be much stiffer than naked DNA. Assuming a fiber persistence length of 240 nm [22] leads to a coil size of $\sqrt{2} \times 240 \text{ nm} \times 2 \text{ m} / 50 \approx 140 \mu\text{m}$. If these stiff chromatin fibers really exists *in vivo* this would call for another level of organization/condensation before the genetic material fits into the nucleus. This larger scale organization will be the main issue we will address in this chapter.

The rest of this chapter is organized as follows. In Section 2.2 we discuss the local fiber structures of *in vitro* 30 nm fibers and the relation with the fibers *in vivo*. In Section (2.3) we discuss some of the polymer models that were introduced to describe the organization of the chromatin fiber on large scales. We argue that the simplest way to describe the fiber is by separating the condensation itself from the organization and show that the resulting model is good enough to explain the existing data. Finally, in Section (2.4) we discuss possible mechanisms for the condensation of the fiber.

2.2 The 30 nm chromatin fiber

Most of what is known about the 30 nm fiber is known through *in vitro* experiments. A large number of theoretical models for the 30 nm fiber has been put forward, all of them being more or less compatible with the experimental data. Only very recently, the assembly of very regular reconstituted fibers brings such high demands on the models that many of them can be invalidated. In this section we will comment on the various models that have been proposed. Furthermore we stress the important role of the energetics of linker DNA bending and of nucleosomal interaction in determining the fiber structure. We discuss how the tails play an important part here and how a cell via their modifications can regulate the degree of fiber condensation.

2.2.1 Old models

Since 30 nm fibers are rather dense, EM-images are open to a plethora of interpretations (cf. Ref. [23] for a recent review on some of the proposed models). Early EM-images, obtained by Finch and Klug in 1976 [24], showed repetitive bands with a spacing of around 110 Å that were almost orthogonal to the fiber axis, whereas no substructures seemed to be present along these bands. This observation suggested a solenoidal arrangement of the nucleosome and with this *solenoidal* model the first chromatin fiber model was born. In order to have successive nucleosomes along the helical path in contact, the linker DNA has to be strongly bent, especially for “short” linker lengths. Structural stability requires thus strong NCP-NCP interactions with the result that the fiber diameter is expected to be independent of the linker length. Although there is no specific argument known why the solenoidal arrangement has a specific diameter, experiments indicating a diameter that is independent of the linker length is seen as supporting the solenoid model. Recent single molecule experiments by Kruithof et al [25] showing a linear force-extension relation of the chromatin fiber over a rather large range of extensions also point in the direction of a solenoid arrangement.

Recurring patterns where nucleosomes seem to stack along two rows, with linker DNA tracing out a *zig-zag* pattern, both in intact [26] and nuclease-digested isolated chromatin [26, 27] led Worcel et al [27] and Woodcock et al [26] to propose so-called *twisted ribbon* models. Cryo-electron microscopy indicated that linker DNAs are essentially straight [21], at least at low salt concentrations. This information gave support to the so-called *crossed-linker* models [28] that assume non-sequential folding of the NCPs connected via straight linkers that criss-cross the interior of the fiber. Such a fiber structure is set by the linkers and not by the NCPs, so that the fiber diameter depends continuously on the linker length (for details cf. the discussion of the two-angle model in Ref. [19]). Slight variations in linker length produce irregular fibers similar to the ones observed for native chromatin [29]. By cross-linking the nucleosomes before digesting the linker DNA with nuclease Dorigo et al [30] came to the conclusion that the fiber must be of the two start type.

2.2.2 Ribbon model

The models we discussed so far do not predict the diameter of the fiber (solenoid model) or they predict a diameter that varies with the linker length (crossed-linker model). The state-of-the-art experiment [31] on the dependence of the fiber diameter on the linker length makes use of the fact that the affinity for nucleosomes depends on the specific sequence of basepairs that wrap around the octamer [32]. This fact allows one to construct DNA templates on which equally spaced nucleosomes are formed [33]. Based on this method Robinson et al [31] produced regular reconstituted chromatin fibers with varying repeat lengths of 177 to 237bp, increasing in steps of 10bp. Their EM measurements revealed a constant diameter of 33nm, and a nucleosome line density (NLD) varying between 0.9 and 1.2 nucleosome per nm, for repeat lengths from 177 up to 207 bp. For the longer repeat lengths the diameter was

Table 2.1: Relation between number of ribbons, fiber diameter and Nucleosome line density.

Ribbons	Diameter (nm)	NLD (nucleosomes/nm)
3	23	0.54
4	28	0.74
5	33	1.0
6	38	1.2
7	44	1.5

44nm, the NLD increasing to a range of $1.3 - 1.5\text{nm}^{-1}$. These results suggest that it is not the length of the linker DNA that sets the fiber diameter, contrary to the prediction of the crossed linker model. Instead these findings support the view that it is the arrangement of the nucleosomes that somehow favors a discrete set of fiber diameters (namely 33 and 44 nm). The linker DNA length enters only as a second order effect that determines which one of the two fiber diameters is chosen.

This leads to the important question of why there is a discrete set of preferred nucleosomal arrangements. To answer this question Depken and Schiessel [34] studied all possible fibers with densely packed nucleosomes. By mapping the chromatin cylinder to a strip with the long sides identified, it is straightforward to show that dense packings are achieved by placing the nucleosomes in ribbons. Different possible dense packings can then be characterized by the number of ribbons. This leads to a discrete set of ribbon models, all of them, however, still having an infinite, continuous range of possible diameters. What changes locally on the nucleosome level, when the diameter is changed is the effective wedge angle between neighboring nucleosomes in a ribbon. It is known from experiments that NCPs under certain conditions form arcs made out of a stack of NCPs where each NCP acts as a wedge with a wedge angle of 8 degrees [35]. Assuming that this is also the ideal wedge angle inside a chromatin fiber, one can predict a discrete set of diameter/NLD combinations depending exclusively on the number of ribbons, see Table 2.1. Note that two of the predicted fibers, the 5 ribbon and the 7 ribbon structures, have diameters that coincide precisely with the experimental values 33 and 44 nm. The 5 ribbon nucleosomal shell can be seen in Figure 2.1.

In addition, one has also to specify the connectivity of the nucleosomes. If one assumes a regular connection which is identical for each pair of connected nucleosomes and where the fiber is not built out of disjoint filaments, the connectivity can be characterized by two numbers, N and m . An (N, m) -fiber is then a fiber with N ribbons where the linker DNA connects ribbons that are m steps apart. One can then show that for fibers with 1, 2, 3, 4 and 6 ribbons the only possible connectivity is the one where neighboring ribbons are

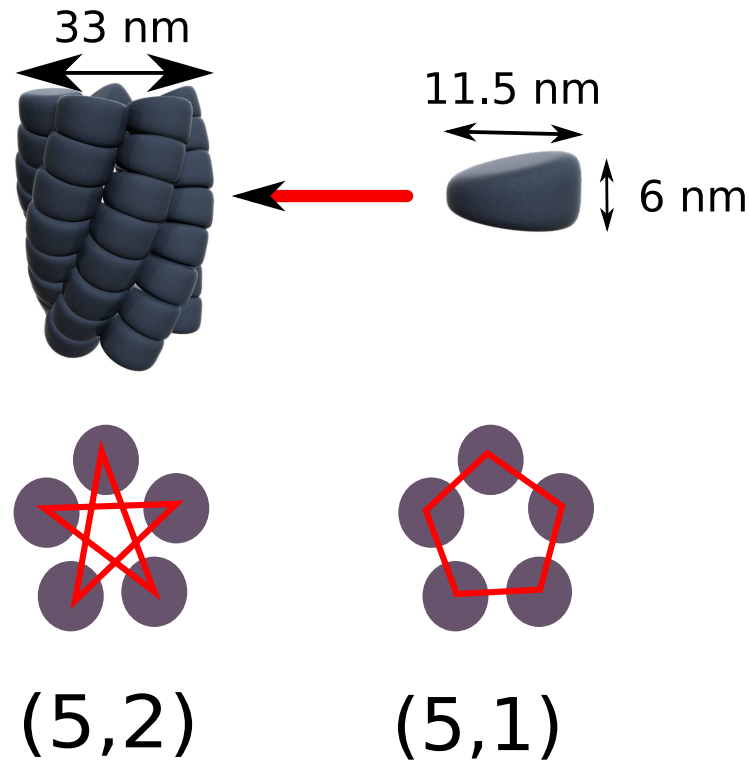


Figure 2.1: A 5-ribbon fiber with two connection schemes, (5,2) and (5,1)

connected, $m = 1$. In this notation the solenoid model is a (1, 1)-fiber and a twisted ribbon is a (2, 1)-fiber. The 5 ribbon structure has besides its nearest neighbor connectivity, (5, 1), also the next nearest neighbor, (5, 2), available. The 7 ribbon model allows for (7, 1), (7, 2) and (7, 3).

Why do the experiments of Robinson et al [31] indicate fiber diameters compatible to a dense 5 ribbon fiber for shorter linker lengths and of a 7 ribbon fiber at longer lengths? In Ref. [34] it is argued that the best of all possible structures is (5, 2) since this, at least for the shortest repeat length, allows for relatively straight linkers. However, when a repeat length of 217 bp is reached the estimated volume of the linker DNA becomes larger than the volume available inside a 5 ribbon shell. At that value of the linker length the linker is just long enough to form a (7, 3) structure with straight linkers whereas the only available 6 ribbon fiber would require strong linker bending. Finally, let us mention that in a recent experiment also a 167 bp repeat length was probed, resulting in a 21.3 nm wide fiber with a NLD of 0.56 nucleosome/nm [36]. This might point to a 3 ribbon structure. The small discrepancy can be attributed to the approximations involved in the model that start to matter at such small fiber diameters.

2.2.3 Energetics: elasticity and electrostatics

One important property we need to address is the energetics involved in the models. It is usually inferred from experiments that the linker histones are crucial [37, 36]. For example Routh et al [36] deduced from EM measurements and sedimentation rates, that reconstituted chromatin fibers with 197 bp repeat length *without* linker histones do not condense into a 33 nm fiber, but into a less dense structure. Pulling experiments in the picoNewton range [25] suggest nonetheless that at low forces such fibers have the same force extension behavior with or without linker histones. Fibers without linker histone show, however, a transition to a more open structure at a lower force value than fibers with linker histones. This suggests a stabilizing role of the linker histones. The conflicting results of Routh et al might reflect the preparation for the EM measurements and the floppiness of the structure in case of the sedimentation measurements.

In both cases, solenoid and crossed-linker model, the energy needed to bend the linker DNA can be estimated, assuming that DNA behaves like a wormlike chain for these contour lengths. The linker lengths range from 3.3 nm to 13 nm for the 30 nm fibers with linker histones and are, except for the shortest value, clearly longer than the helical repeat of the double helix. For the solenoid model the elastic energy can be as high as 35 kT per nucleosome. This high value actually suggests that the solenoidal structure, especially its diameter, would change with linker length to reduce the elastic penalty. At first sight a 5 ribbon structure would encounter similar problems, but here the ribbons can slide with respect to each other without changing the fiber diameter or NLD, lowering the elastic energy to a few kT's per nucleosome, the exact value depending on parameters like stem length and the exit angle by which the linker DNA leaves the stem.

It is not only the elastic energy that needs to be accounted for, but there is also a strong electrostatic repulsion between the negatively charged linkers. The above mentioned picoNewton pulling experiments by Kruithof et al indicate that the presence of magnesium ions is indispensable for the formation of a 30 nm fiber. This can be most likely attributed to the strong electrostatic repulsion that affects the linkers in a dense fiber. What the high density of nucleosomes suggest is that there is an effective attraction between NCPs that dictates the fiber condensation. This is the subject of the next section.

2.2.4 Energetics: Nucleosome attraction

In the experiments by Dubochet and Noll in 1978 [35] it was found that isolated NCPs in controlled ionic conditions show a strong tendency to self-assemble into arcs and cylinders, and this in the absence of magnesium. The NCPs are stacked “face-to-face”, indicating the importance of nucleosome interactions in the formation of higher-order structures. As a possible mechanism behind the nucleosomal attraction was later put forward the formation of tail bridges where positively charged tails of one nucleosome interact with negative charges on the core of a NCP closeby.

The tail conformations result from a competition between electrostatics and entropy. For low salt concentrations tails are condensed onto their nucleosome, whereas for higher salt concentrations, the entropic contribution of the tails to the free energy becomes more important. The tails gradually unfold with increasing ionic strength and the effective diameter of the NCP saturates around physiological salt concentrations [38]. Osmometric measurements on dilute solutions of NCPs show a minimum in the 2nd virial coefficient around the same salt concentration [39]. This led Mangenot et al [39] to suggest that the tails give the dominant contribution to the interaction between nucleosomes. More recently Bertin et al [40] found that tail-intact NCPs show attraction in the absence of magnesium, with a 2nd virial coefficient in qualitative agreement with Mangenot et al, whereas it approached the hard-sphere repulsive interaction for NCPs where the tails were removed with trypsin. Moreover, for trypsinized oligonucleosomes it has been observed that no higher order folding occurred for an increase in monovalent salt [41] or magnesium concentration [42].

To understand better how the tails induce an effective attraction Mühlbacher et al [43] modelled the NCPs as freely rotating spheres with a homogeneous surface charge distribution representing the histone-DNA core of the NCP. The eight tails were modelled as identical flexible chains grafted onto the sphere at the vertices of a cube inscribed in the sphere. The screened electrostatics was approximated by the Debye-Hückel interaction. For an appropriately chosen effective sphere charge the pair potential showed an effective attraction of a few $k_B T$ around physiological salt concentrations. Importantly this attraction disappeared when a small fraction of the tail charges was removed – hinting at a possible biochemical mechanism through which the cell can control the nucleosomal interaction.

2.2.5 The 30 nm fiber *in vivo*

Until now we have discussed an idealized 30 nm fiber, mostly based on very regular reconstituted fibers in clean static conditions. It is an open question how relevant these structures are for the properties of chromatin within the nucleus. Bystricky et al [44] measured how the spatial distance (SD) depends on the chemical distance (CD) along the DNA double helix in budding yeast, using fluorescence in situ hybridization (FISH) for CDs from 14 kb (kilo basepairs) up to 100 kb. We will adhere here to the convention of expressing the CD in the number of basepairs, each basepair contributing a "length" of 0.35 nm.

Before we discuss the FISH data we need to address the reliability of 3d-FISH measurements. The main steps of FISH consists of a fixation step (using buffered formaldehyde), a denaturalization step (by heating up the sample to 75 °C for 2 minutes) followed by a hybridization step where a fluorescent probe is matched to a specific sequence of the (denatured) DNA. Obviously these procedures are rather harsh. Recent experiments [45, 46] set up to evaluate the reliability of FISH experiments came to the conclusion that large scale structures, down to light microscope resolution, are reasonably well preserved for this 3d-FISH. The older "2d-FISH", based on methanol/acetic acid fixation seems to be significantly less reliable. On a smaller scale both procedures are destructive and reliability suffers.

Keeping these restrictions in mind, Bystricky et al [44] could fit their data with the curve of a wormlike chain with a persistence length of 170 – 200 nm and a NLD of 0.64 – 0.91 nucleosomes/nm. Apparently a rather stiff condensed fiber is formed but how it relates to the original *in vivo* structure is an open question. Nonetheless the persistence length inferred from the experiment is in relatively good agreement with coarse grained models of the 30 nm fiber [22, 47]. Especially from the simulation in Ref. [22] one can draw the not so surprising conclusion that the worm like chain model is only appropriate for small bends. Kinks can be formed with relative low cost. This last point has to be kept in mind when discussing large scale structures to which we will turn in the next session.

2.2.6 Conclusion: the 30 nm fiber

The existing models of the 30nm fiber should be regarded as a description of a groundstate of the chromatin fiber in the nucleus. The reconstituted fibers form an interesting playground to get a grip on the possible energies that play a role in the formation. It is important to realize that in the nucleus the chromatin fiber gets synthesized in a way different from that of reconstituted fibers. The *in vivo* fiber is also not as regular and static as the reconstituted fibers. Although the fiber is often thought of as a wormlike chain, it should be kept in mind that a notion of persistence length is only valid as some kind of rough average. The flexibility has most likely large variations and the fiber is highly extensible. We will not rely on any specific persistence length for the next section. When there is a need to compare values with the value of the Kuhn length of the chromatin fiber we will use a value of 300 nm, realizing that one could argue as well for lengths ranging from 60 [48] to 400 [44] nm.

2.3 Large scale structures

By analyzing local radiation damage of chromosomes [49] Cremer et al concluded – contrary to the general picture at that time – that during interphase chromosomes are segregated within their own domain. Most of the evidence for the existence of these separate chromosome domains comes from FISH data. As we have discussed before, the resolution of these data is restricted to the optical one, not only because of the measurement apparatus but also due to the preparation procedure. Although there is some evidence that intermingling of chromatin domains does occur [50], recent experiments point in the direction of domains that at least do not intertwine [51]. This section discusses the structure of chromosomes in their own domain.

2.3.1 Experiments and models

The use of FISH to examine the distribution of chromatin in interphase nuclei dates back to van den Engh et al [52]. They measured via 2d-FISH the SD versus the CD for many pairs of probes. In a first analysis of their data they noticed that they could fit it to a Gaussian chain up

to 2 Mbp of CD. For longer CDs a flattening of the curve was found indicating the existence of some constraint. This analysis was worked out in greater detail by Hahnfeldt et al [53] where the data were fitted to a Gaussian chain within a spherical confinement. Extension of these 2d-FISH measurements on the same chromosomes up to 190 Mbp [54] showed for larger CD's again the footprint of a random walk but with a considerable smaller slope of CD versus the squared SD. The data were fitted to a fixed Mbp giant loop model with the loop nodes forming a long distance random walk. It was argued that this is the simplest model to explain the new data.

These same data led Mönkel and Langowski [55] to propose their multi-loop subcompartment model as a Gaussian chain with a non-hardcore volume interaction together with harmonic bonding into loops. A compartment of loops is then attached to the next compartment by a chromatin link. Their idea was first of all to emulate the formation of clearly separated subcompartments within a chromosome territory. Several characterizations of these subcompartments exist. We will use the terminology euchromatin for the less dense, gene active regions and heterochromatin for the denser, inactive regions. Other not fully compatible terms are R-band/G-band (based on Giemsa staining) [56], ridge (regions of increased gene expression)/antiridge [57], depending on one's taste, measurement technology or functionality. A special feature of this model is that, according to the authors, it replicates the scaling of the SD as a function of the CD over large distances, *not* as a polymer at its θ -point (a random walk with exponent $1/2$), *nor* as a polymer in a good solvent (a self avoiding random walk with exponent $3/5$), but with an exponent of $1/3$, from which they inferred that it behaves as a globule.

More recent 3d-FISH measurements [58, 59] differentiated between distances within euchromatin and heterochromatin regions of chromosomes in human fibroblast cells. The authors noted that they could fit their data to a globular state with exponent $1/3$ but observed also a levelling off to a constant value for larger CDs. The size of this levelling off was significantly different for different regions, strengthening the idea that non active regions are considerably denser than active ones. The above mentioned levelling off led Bohn et al [60] to propose yet another loop based model: the random loop model. A Gaussian chain without volume interactions but with harmonic attraction of the same strength as the chain links is introduced between non-neighboring beads whose separation is chosen with a fixed probability. The authors claimed that such a random loop configuration is needed to explain the levelling off.

2.3.2 The loop and the globule

In this subsection we attempt to critically analyze the models that we briefly discussed in the previous subsection. Our starting point is the fact that the chromatin fibers within the nucleus and also within their compartments are highly confined. We now separate this notion of confinement from the spatial distribution of the chromatin, somewhat in the spirit of the spherical confinement model. The possible mechanism behind this confinement will be

discussed in the next section. The logic behind this approach is that it is not known what causes the confinement, let alone the details behind it. As will become clear we also do not need this knowledge to explain the data presented so far. This also means that we will not assume any loop formation, leaving the causality between confinement and loop formation open.

To set the stage let us estimate the density of the chromatin fiber in a human cell. Human lymphocytes have a nuclear volume between 380 and 525 μm^3 [61]. Let us assume that the chromatin is spread throughout the nucleus, neglecting the space taken up by nuclear organelles like the nucleoli or other non chromatin domains. We expect this approximation to be sufficient in view of the precision of the experiments we aim to describe here. With a NLD of 0.7 nm^{-1} , repeat length of 200 bp and a fiber diameter of 33 nm, a 380 μm^3 nucleus corresponds to a chromatin volume fraction of almost 0.1. The first fact that needs to be understood is why a pure random walk can explain the data this well (up to lengths before confinement/loop forming sets in). After all, the chromatin fiber has a high cross section. It could be a coincidence that attractive forces just balance the repulsive forces and the Kuhn length could be much shorter than what we would conclude from a persistence length of around 150 nm. In that case it makes one wonder how this could be achieved with varying density. It is appropriate to introduce some (old) polymer physics at this point.

Let us suppose that chromatin is highly confined but in a reasonably good solvent. When we start to follow the chromatin fiber from a given point, for length scales up to its persistence length, the relation between SD and CD will be linear. For longer contour lengths there will be a crossover first to a random walk followed by a crossover to a self avoiding random walk. For length scales larger than that correlation length, density-fluctuations disappear and there is no preferred direction. The correlation length is just set by the distance where collisions with segments closeby in CD and segments far away, i.e. for large CD's, are as likely. This length scale can be derived following Ref. [62] that we use in the following.

The expectation value for the segment density, C_0 , is constant within a compartment. This is in fact only true neglecting boundary effects, but with the relatively high densities in the nucleus this is a reasonable assumption. Starting from one segment at the origin, in its proximity the segment distribution can be divided into a contribution coming from segments close by along the backbone, c_c , and segments far away, c_f , both strongly fluctuating on small scales:

$$C_0 = \langle c_c(r) + c_f(r) \rangle = \langle c_c(r) \rangle + \langle c_f(r) \rangle. \quad (2.1)$$

Suppose now that the solution is dilute enough such that excluded volume effects become important before the semi-diluteness of the solution becomes relevant. Close to the origin the density is dominated by the first term and the presence of far away segments can be neglected.

N segments of the chain with volume interactions have then a radius of gyration that scales as

$$R \approx a \left(\frac{v}{a^3} \right)^{1/5} N^{3/5}, \quad (2.2)$$

where a is the Kuhn length and v the excluded volume. From this expression follows as segment density:

$$\langle c_c(r) \rangle \approx \left(\frac{a^3}{v} \right)^{1/3} a^{-3} \left(\frac{r}{a} \right)^{-4/3} \quad (2.3)$$

The far away contribution kicks in when the first term becomes of the order of the overall density. This defines the correlation length ξ :

$$\frac{\xi}{a} \approx \left(\frac{a^3}{v} \right)^{1/4} (C_0 a^3)^{-3/4}. \quad (2.4)$$

On length scales larger than ξ , the density fluctuations are minimal and the chromatin is in the globular state. Although it is true that the size of a globule scales as $(\# \text{monomers})^{1/3}$ it is a misconception that locally the distance between segments scales with $(\# \text{ of connecting segments})^{1/3}$. It is an old argument by Flory [3] that points to an exponent of $1/2$ in this case: namely because of the homogeneity of the globule is the pressure from all directions the same and so there are no effective volume effects. The chain forms thus a random walk of "blobs" with the blob size given by the correlation length. Although there are some deviations at short length scales to this "Flory ideal chain hypothesis", it was recently shown by Lua et al [63] – using an ingenious counting algorithm on a lattice – to hold more than well enough. The only drawback of that simulation when applied to our problem is that it presupposes that the system is ergodic and that the system has time to thermalize. That last point might be important, as we will discuss at the end of this section.

Let us consider in this context the more recent 3d-FISH data for chromosome 1 in human fibroblast [58]. The only data available are the average SD as function of the CD *and* the standard deviation, both depicted in Figure 2.2. Knowing other moments might reveal more details. As mentioned before the SD levels off at larger CDs. We expect that the height of the plateau corresponds to the average distance between two points in the compartment:

$$\langle SD \rangle = \frac{1}{V^2} \int_V d^3 \mathbf{r}_1 \int_V d^3 \mathbf{r}_2 |\mathbf{r}_1 - \mathbf{r}_2| \quad (2.5)$$

For example for a spherical compartment of radius R we find an average of $(36/35)R$ and a standard deviation of $\sigma = (\sqrt{174}/35)R \approx 0.38R$, while for a flat disk with radius R the average distance is $0.9R$ with a standard deviation of $0.42R$. Human fibroblast has an almost 2d nucleus as can be inferred also from the FISH measurements over the whole chromosome 1 [58]. For a length of 30 Mb there is a levelling off around $1.8 \mu\text{m}$. Using a volume fraction

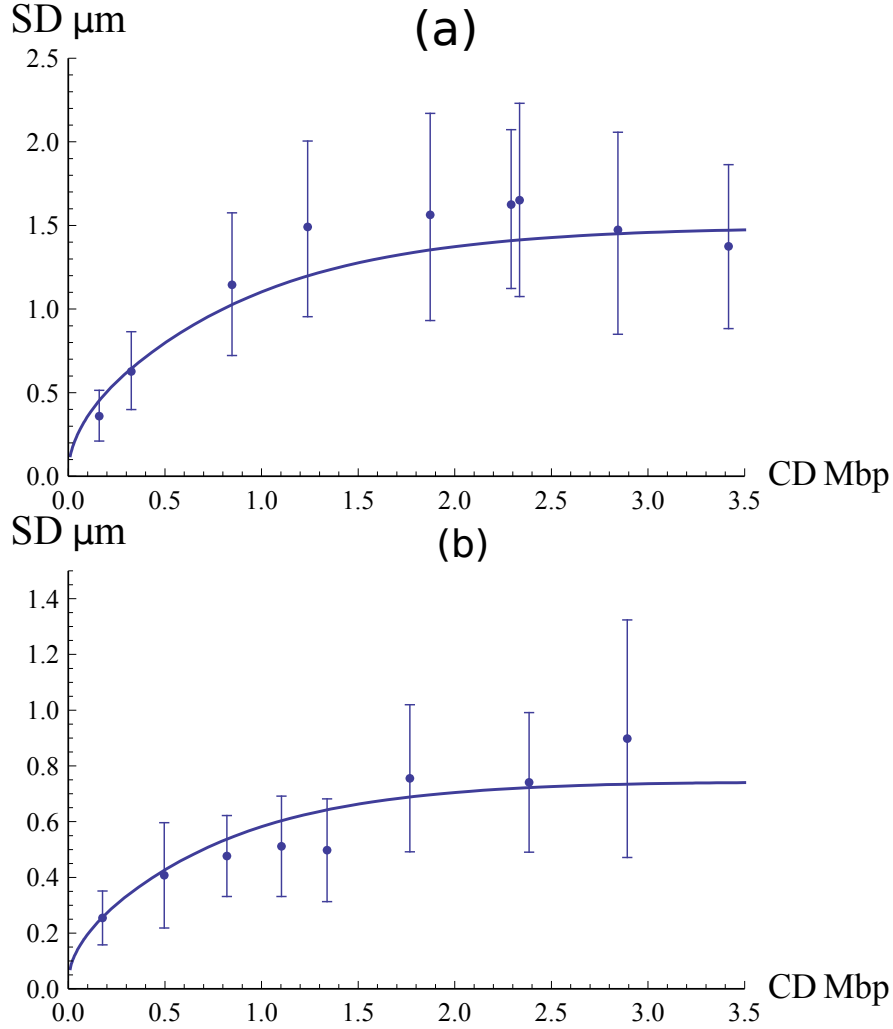


Figure 2.2: 3d-FISH data from [58] for the (a) active and (b) non active regions of chromosome 1 in fibroblasts. The error bars are the standard deviations. The curves use (2.7) with the parameters given in the main text.

of 0.1, a repeat length of $r_l = 200$ bp, and an NLD of 0.7 nm^{-1} one predicts a value of the thickness for a disk-shaped compartment of 150 nm.

It is important to realize that although the globular state has local Gaussian behavior, it is not to be confused with a Gaussian chain confined to the region of a globule, the structure assumed in [53]. The latter has a strong density peak in the center of the confinement [3], while here we have a constant density profile. The reason for this difference is that the confined Gaussian is Gaussian because of the *lack* of volume interactions while in the case of a globule it is Gaussian *because* of volume interactions. This distinction is not always appreciated. Would we repeat the calculation for the average distance and standard deviation using the

confined Gaussian probability, $\rho(r) = \sin(\frac{\pi r}{R})/(\pi R r^2)$, we would find for the height of the plateau and its standard deviation:

$$\langle SD(CD \rightarrow \infty) \rangle_{\text{Gauss}} \approx 0.7R \quad \sigma_{\text{Gauss}} \approx 0.14R \quad (2.6)$$

We would clearly get a higher estimate of the size of the compartment. It is interesting to note that the *relative* standard deviation is 0.2, considerably smaller than the 0.38 for the globule. When we compare this with the plateau of chromosome 1, for both eu- and heterochromatin compartments, we see a relative standard deviation of 0.37 indicating that the picture of a globule describes this in a satisfactory way.

In the following we model the chromatin within its compartment as a Gaussian chain within a rectangular box. To ensure a flat density profile we have to choose reflecting boundary conditions. The mean squared SD is then given by:

$$\langle (SD(CD))^2 \rangle = \frac{1}{V} \left(\frac{3}{2\pi L(CD)b} \right)^{3/2} \int_V d^3\mathbf{r}_1 \int_V d^3\mathbf{r}_2 (\mathbf{r}_1 - \mathbf{r}_2)^2 \quad (2.7)$$

$$\sum_{n_x, n_y, n_z = -\infty}^{\infty} \left[\exp \left(-\frac{3(\mathbf{r}_1 - f_{\mathbf{n}}(\mathbf{r}_2))^2}{2L(CD)b} \right) \right], \quad (2.8)$$

where

$$f_{\mathbf{n}}(\mathbf{r})_i := (-1)^{n_i} (r_i - n_i L_i) \quad (2.9)$$

takes care of the reflections. The number of reflections is counted by \mathbf{n} in each direction. The quantity b is the step length of the random walk and $L(CD)$ is its length. A natural choice for b is the correlation length. In that case $L(CD)$ would be the contour length of the random walk of correlation blobs. The problem here is that we do not know the functional relationship $L = L(CD)$. Let us use the contour length of the chromatin fiber, using the same values as above. The size of the box we choose to be $3.1 \times 3.1 \times 0.15 \mu\text{m}$. Fitting the curve of $\sqrt{\langle (SD(CD))^2 \rangle}$ to the 3d-FISH data [58] we extract a step size of $b = 80 \text{ nm}$. We can also estimate the correlation length using equation (2.4). We assume $a = 300 \text{ nm}$ as Kuhn length and a rigid rod excluded volume a la Onsager [16] of $v = a^2 d$ where we take $d = 30 \text{ nm}$ as diameter. This results in an effective segment volume of $\pi d^2 a / 4 \text{ nm}^3$. If we assume again a volume fraction of 0.1 we recover a correlation length of 80 nm. This seems to be good to be true, especially after realizing that the correlation length is *shorter* than the Kuhn length on which we based the calculation. In fact we find for the thermal blob size, the size up to which a non-confined chain can be considered ideal, using the same fiber parameters as above, a value larger than $1 \mu\text{m}$. We have apparently overestimated the segment density in deriving equation (2.4). Using instead ideal chain scaling up to the correlation length results in a correlation length as follows

$$\frac{\xi_{\text{ideal}}}{a} \approx \frac{1}{C_0 a^3} \quad (2.10)$$

With the same values as before we now find a correlation length of 24 nm, a value much smaller than before. This point illustrates nicely that the data available at the moment do not justify detailed models.

We can repeat the same calculations for a heterochromatin region. The resulting fit for a correlation length of 20 nm is depicted in Figure 2.2 (b). The compaction of the heterochromatin is, depending on the excluded volume parameter, $4^{(3/4)} \cong 2.8$, equation (2.4), to 4, equation (2.10), times higher in this naive view.

Although the concept of a globule seems to fit the data well, this is somewhat deceptive. First of all FISH data are not very reliable. Higher moments might reveal more structure than a globular state. One should also not forget that the nucleus is never in equilibrium. Active processes do influence the distribution of chromatin and the cell is continuously evolving through its cell cycle. An interesting example is a recent simulation by Rosa and Everaers [64] where the interphase structure is a consequence of the fast decondensation of structured mitotic chromosomes within the confinement of the nuclear envelope, whereas the timescale of equilibration is much longer than the duration of interphase. The consequence is that the chromatin fiber is not thermalized. Although they compare their simulations with rather unreliable 2D-FISH data, the authors demonstrate how the nonequilibrium conditions in the nucleus can influence the spatial distribution of chromatin.

2.3.3 Conclusion: large scale structure

The techniques available, in the time the paper on which this chapter is based was written, to reveal the large scale organization of chromatin do in our opinion not justify any detailed polymer model. Most features one can capture with the statement that chromatin exists in a condensed state. A new development is the 5C (chromosome conformation capture carbon copy) technique, developed by Job Dekker [65], where the cell is fixated for some time allowing parts of the chromatin that are in close proximity to attach. Statistical analysis on the contact points gives an indication of what parts of the chromosome are structurally in close proximity. Based on this analysis it is argued, that the chromatin fiber is ordered as a fractal. The benefit would be the lack of entanglement. This possible fractal structure was hinted at by Grosberg [66] already in 1988. His ideas were based on theoretical arguments from deGennes [67] that a collapsed linear polymer does not collapse immediately to a globule in the Flory sense, but collapses first, in a cascade of smaller globules that have no time to thermally mix, into a fractal globule. The weak point of this line of thought is that in reality the chromatin never collapses from a good solvent, but is continuously in a more or less condensed globular state. A weaker statement is that the chromatin happens to be in a non-entangled conformation as a result of its history, and that the time scale of entanglement is much longer than the cell cycle referring again to the simulations [64] mentioned in the last subsection

2.4 Mechanism behind compactification

As we have seen the chromosomes within the nucleus are more or less confined, each in its own domain. These domains are much smaller than the typical size of a chromatin fiber in a good solvent. The amount of compactification in interphase is furthermore not constant but varies considerably between regions containing active genes and less active regions.

Within the cell cycle a dramatic increase of compactification is apparent when the cell enters metaphase. This change from dispersed interphase chromosomes towards compactified mitotic chromosomes during prophase is fast and remarkably synchronous.

The question one has to ask is what are the forces involved in compactifying the chromatin inside the nucleus, depending on its activity during interphase and into mitotic chromosome during mitosis, while keeping different chromosomes separated. At the same time these forces might be also somehow relevant for sister chromatid segregation after replication.

One factor we will not consider here are active processes that could take part in condensing or decondensing chromatin. We like to think that these factors are working on top of a more general mechanism.

2.4.1 Enclosure

At first thought one might think that the chromatin is confined by the nuclear envelope, the double membrane encapsulating the nucleus. This was assumed in a recent simulation where it was also pointed out that the time scale of the cell cycle is too short for the expanded chromatins to thermalize [64] and especially to mix. This is an attractive scenario, especially reminding us that the organization of chromatin is probably never in equilibrium.

Purely by enclosing the nucleus it is, however, not possible to regulate the densities depending on gene activity. Especially, some regions in the nucleus seem to be chromatin-free without any membrane separating them from the chromatin containing regions [68, 51]. Finally there is still the need for a mechanism to condense the chromatin for mitosis.

2.4.2 Specific binding sites

Two somewhat overlapping models start from a more or less rigid backbone of proteins or protein filaments.

Nuclear Matrix

The nuclear matrix (for a review see [69]) is conceived to be a network of filaments that span the nucleus reminiscent of the cytoskeleton in the cytoplasm. The idea is that this network is responsible for the organization in chromatin compartments. The chromatin is supposed to be attached to this network through specific sequences along the genome appropriately named MAR's or Matrix Attachment Regions, some not precisely known, presumably AT

rich regions. An important problem with this model is that the network itself has never been indisputably detected and it is often defined as “the stuff that is left behind within the nuclear envelope when all other material has been extracted.” The electron microscope images suggesting such a structure could suffer from artifacts caused by sample preparation. A second objection is the variable position of each chromosome from cell to cell [49] that makes the existence of such a well defined nuclear matrix less likely.

Finally a large number of specific MAR's slightly contradicts the notion of robustness under mutation and of the constrained diffusion of chromatin observed during interphase [70]. It is nonetheless very well possible that some parts of the chromosome are localized with respect to the nuclear envelope. Conceptually this seems likely at least for the centromere, being the only part of the chromatin that needs to be localized during mitosis.

Scaffold

The idea that a rigid protein scaffold organizes the chromosomes originates from EM pictures of mitotic chromosomes depleted from histones using high salt concentrations [71]. A core of non-histone proteins in the shape of the original mitotic chromosome remains with a halo of bare DNA loops attached to it. The main constituents of this scaffold were later found to be topoisomerase II [72] and condensin [73], the former being a protein complex responsible for disentangling DNA, the latter being a complex closely related to the cohesin complex that keeps the two sister chromatids bound together up to telophase [74]. The picture that evolved was that of loops of chromatin attached to the protein scaffold through specific AT rich regions called SAR's (scaffold attachment regions). The notion of a scaffold has some overlap with the previously mentioned nuclear matrix and not too surprisingly the weak points of the matrix concept carry over to the scaffold.

A strong argument against the structural importance of a mitotic scaffold can be drawn from experiments by Poirier and Marko in 2002 [75], where it was found that the mitotic chromosome loses its structural integrity by gradually cutting the DNA with nuclease, showing that the chromatin fiber defines the structure of the chromosome, making the existence of a scaffold unlikely. Moreover, it was already known that topoisomerase II was not needed for the formation of the mitotic structure [76]. In 2006 it was found, surprisingly, that the same holds for condensin. The main function of condensin seems to be the stabilization of the mitotic chromosome during telophase [77].

2.4.3 Non specific compactification

Electrostatics

An alternative to these local types of mechanisms is the idea that attractive interactions between segments of the chromatin fiber dominate the hardcore like repulsive forces in such a way that the 2nd virial coefficient becomes negative, turning the effective background of the chromatin into a poor solvent. This attraction could be caused by a tail bridging effect, as

we have discussed above between nucleosomes, and/or mediated by dynamically chromatin binding proteins.

There are some suggestions in the literature [78] that the environment in the nucleus is such that most counterions of even strong polyelectrolytes are condensed, caused by the lack of free water. Measurements on several cell types do not support this view:

- The water content of the nuclei of amphibian oocytes was measured to be around 74 – 80% of mass [79] and of rat liver cells over 85% [80].
- NMR measurements [81] of frog (*Xenopus Laevis*) oocytes showed that almost 90% of the water present in the nucleus can be considered free.
- Even the water content of the highly condensed mitotic chromosome was estimated to be at least one third of the volume [82].

There is at this stage no reason to believe that the electrochemical conditions within the nucleus differ much from what one considers physiological:

- The nuclear envelope contains a large number of nuclear pores, typically around 3000, but in certain oocytes up to 50 million [83]. These pores are fully permeable for particles up to 9 nm in diameter [84].
- The 30 nm chromatin fiber as seen *in vitro* in “physiological” conditions closely resembles the fiberlike structure seen in FISH experiments [44], as explained before.
- As mentioned above NCPs seem to be tuned for minimizing their second virial coefficients at ‘physiological’ salt concentrations.
- Extracted mitotic chromosomes appear to have their *in vivo* dimensions at “physiological” conditions, reversibly condensing or decondensing with a change in salt concentration [82].
- Upon hypertonic shock the chromatin partly condenses [51], indicating a strong dependence on salt concentration.

The change in the level of compactification is correlated with some of the histone modifications. A typical example is an H3 phosphorylation during mitosis [85]. The same phosphorylation is correlated with the formation of heterochromatin [86]. It is possible that some of the modifications have a direct effect on the interaction between segments of the chromatin fiber through changes in the charge of the tails. Alternatively they could affect the binding of proteins that mediate the electrostatic interaction.

A somewhat puzzling feature is the formation of the aforementioned hypercondensation caused by an increase of salt concentration, a condition that weakens the range of the electrostatic forces through increased screening. Another point that still is hard to understand is how this subtle balance between attractive and repulsive forces can be maintained over such a large variety of cells and organisms.

Crowding

The notion of crowding in biology [87] corresponds roughly to the notion of depletion in colloid physics. For the case that the colloids are much larger than the polymers, the so-called colloid limit, the effective attraction between the colloids is reasonably well understood [8]: When two colloids are separated by a distance shorter than the size of the polymer coils, the osmotic pressure of the polymers pushes the two colloids together. Subtleties arise from the ease with which two polymers can overlap [3] and from the appearance of a repulsive barrier when incorporating higher order interaction terms, but the main picture remains.

In the protein limit where the colloid is much smaller than the polymer, the situation is not that clear. This is the limit of interest for the condensation of chromatin in the nucleus. If we think of the chromatin fiber as being dilute in a good solvent or in a semi-dilute solution, the relevant length scale characterizing the fiber, namely the radius of gyration or the correlation length, is considerably larger than the typical size of the proteins (around 2.5 nm). In that case it was shown by DeGennes [1] that purely by excluded volume effects polymers and nanoparticles with the size of an average protein are highly miscible. The conceptual reason is that then the range of the depletion is set by the size of the protein [88]. Since the cost of placing the nanoparticle within the polymer is expected to be proportional to the segment concentration, a scaling argument shows that this requires little work. In that case is also the minimum of the depletion potential between two nanoparticles not deep enough to cause phase separation. This was also confirmed in experiments, where non-DNA binding proteins from E-coli extracts alone could not condense DNA [89], even not with concentrations considerably higher than what is found in eukaryotic nuclei. Another experiment that indicates that nanoparticles of the size of the average protein easily diffuse within the densest chromatin regions, even within the mitotic chromatin fibers, was conducted by Verschure et al. [90].

Unless other effects decrease the excluded volume parameter of the chromatin fiber and/or increase the interaction between DNA and nanoparticles, depletion interactions seem to be too small to cause condensation of the chromatin fiber. A recent paper [91] discusses the possibility that charged nanoparticles, with the same charge as the polymer, could cause condensation in the spirit of Odijk's osmotic compaction [92] of the supercoiled DNA in E-coli. The negatively charged protein fraction needed seems to be too high to be realizable, without further ingredients, in the nucleus, where overall non-histone protein fractions are 0.1 – 0.15.

2.5 Conclusion

It is clear that the eukaryotic nucleus is an extremely complex system. The biophysical approaches have made progress in the description of chromatin by building the models from a detailed picture. At some point the barriers to overcome seems, however, to be too hard to continue in that way. On the other hand it seems logical that the robustness of the eukaryotic nucleus against changing conditions and mutations must have a general physical explanation.

In this chapter we have discussed the strengths and the weaknesses of the common approaches towards an understanding of the cell cycle. We have shown that no detailed model is needed to explain the large scale organization of chromatin observed so far. This notion makes it possible to separate the physics behind the organization from the detailed structure. We hope that this approach will lead in the near future to a better understanding of the cell cycle.

Euler Buckling

3.1 Motivation

As we have seen when reviewing the natural environment of DNA, there are many levels of abstraction where the physics, although still poorly understood, can have a large impact. The level of abstraction depends of course a lot on the questions one wants to answer. And those questions change over time. New experimental methods are often a driving force to improve models or calculations. During the last few years, the advent of single molecule nanomanipulation [93] has allowed to study the elastic properties of DNA and other biopolymers under different physical conditions. In these experiments, the extension of single molecule versus an applied stretching force is measured by a variety of techniques including magnetic beads [94, 95], optical traps [96, 97], micro-needles [98], hydrodynamic flow [99] and AFM [100]. While the statistical mechanics of unconstrained DNA under tension is theoretically well understood in the framework of the WLC model [101, 102, 103, 104, 105] the presence of topological constraints like supercoiling that we will study in more detail in Chapter 5 or geometrical constraints like protein induced kinks and bends [106, 107, 108, 109, 110] renders analytical results more difficult.

Instead of studying the elastic properties of biopolymers under stretching, mechanical properties can also be studied by using compression, as long as the chains are smaller than the persistence length. This has been used for example in experiments targeted to measure the force-velocity relation of microtubule growth [111] and in determining the force produced by actin filaments [112] and more recently in analyzing the force generation by polymerizing of actin bundles [113].

With the exception of the work of Odijk [114] who studied a semi-classical evaluation of the partition function in the linear regime (Figure 3.1 (a)), i.e., below the buckling transition, no calculations have been done that consider the non-linear regime of external forces above the critical force (Figure 3.1 (b)). Furthermore these calculations are only valid well below the transition, although it is the behavior close to the transition on which the force calculations

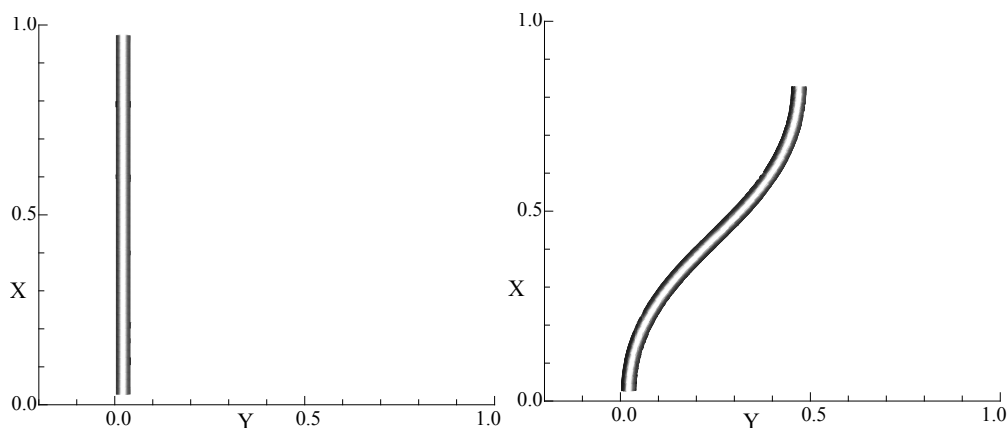


Figure 3.1: Force below (a) and above (b) the Euler transition.

are based. In this paper we study thermal fluctuations up to the transition in order to evaluate the scaling of the point of buckling with increasing length. We note that the concept of a phase transition-like sharp transition disappears for finite temperatures, as follows from the one dimensionality of the system. The transition region effectively broadens with increasing length at finite temperatures.

A computer simulation for 2 and 3 dimensional configurations shows that the thermal fluctuations decrease the extension in the buckled state of the polymer in 3 dimensions, but increase it in 2 dimensions (Figure 3.4). In this chapter we show analytically how this happens, by doing a harmonic perturbation calculation around the buckled state.

As a final note we mention that recently the properties of DNA, like its stiffness and its sequence-specific pairing have been exploited to build different kinds of nanostructures [115]. In particular a DNA tetrahedron which has been already synthesized could be the building block of extended nanostructures [116]. Our calculations can be used to estimate the forces these structures can withstand.

We will continue as follows: we start by describing the geometry and the model used in Section 3.2, briefly treating its classical elastica solutions in Section 3.3. The main body of this chapter is in Section 3.4. It consists of a semi-classical calculation of the force extension behavior for a WLC with finite length and persistence length below and above the Euler transition. We extend these calculations to quartic order below the transition in Section 3.5, in order to analyze the change in the buckling transition caused by thermal fluctuations. In Section 3.6 we compare our calculations with simulations. We end the chapter in Section 3.7 with a discussion of our results in the light of several recent experiments with stiff biopolymers.

3.2 The Partition Sum of a WLC under Compression

We model a stiff polymer as a WLC, without a twist degree of freedom. In this case, the polymer configuration is completely characterized by specifying the unit vector $\mathbf{t}(s)$ along the chain, where s is the contour parameter length with $0 < s < L_c$. When the chain is submitted to a compressive force f the total (as a reminder: reduced) energy is

$$\mathcal{E}[\mathbf{t}] = \int_0^{L_c} \left[\frac{P_b}{2} \left(\frac{d\mathbf{t}}{ds} \right)^2 + f \cdot \mathbf{t} \right] ds \quad (3.1)$$

From an elasticity point of view the persistence length is related to the bending modulus as $A = P_b k_B T$. It is the coefficient of the linear constitutive equation for bending. Seen from this perspective the persistence length is temperature dependent. Since the temperature range in which biopolymers are functional is limited, temperature dependence is usually not important; for example for DNA at room temperature $P_b \approx 50$ nm [117]. All the statistical properties of interest can be deduced from the configurational partition sum which is a non-trivial quantity to evaluate because of the local constraint $\mathbf{t}^2(s) = 1$ that assures the inextensibility of the chain:

$$Z = \int \delta^{(3)}(\mathbf{t}^2 - 1) \mathcal{D}^3[\mathbf{t}] e^{-\mathcal{E}[\mathbf{t}]} \quad (3.2)$$

This partition function is nothing but the Euclidean path integral of a quantum particle with mass P_b , moving on a unit sphere under the influence of an external constant force. We are interested in the thermal fluctuations around a “classical path”. These are easiest found in polar coordinates. We will fix the force along the x -axis (see Figure 3.1 (a),(b)) to avoid the chart singularity at the poles. For notational convenience we will choose the polar angle $\vartheta \in [-\pi/2, \pi/2]$ such that the uncompressed chain has the coordinates $(\vartheta(s), \varphi(s)) = (0, 0)$. In these coordinates the energy has the form:

$$E[\vartheta(s), \varphi(s)] = \int_0^{L_c} \left\{ \frac{P_b}{2} \left(\cos^2 \vartheta(s) \dot{\varphi}^2(s) + \dot{\vartheta}^2(s) \right) + f \cos \vartheta(s) \cos \varphi(s) \right\} ds \quad (3.3)$$

We can rewrite the energy in dimensionless variables as:

$$\mathcal{E}[\theta(s), \phi(s)] = \frac{1}{h} \int_0^1 \left\{ \frac{1}{2} \left(\cos^2 \theta(t) \dot{\phi}^2(t) + \dot{\theta}^2(t) \right) + G^2 \cos \theta(t) \cos \phi(t) \right\} dt \quad (3.4)$$

$$\phi(t) := \varphi(t L_c), \theta(t) := \vartheta(t L_c)$$

where we have introduced the fluctuation parameter

$$h := \frac{L_c}{P_b}$$

and the coupling strength

$$G := L_c \sqrt{\frac{f}{P_b}}$$

The square root in the last expression is in fact the reciprocal of the deflection length [118] of the chain. We are interested in the small fluctuation regime and use h as an expansion parameter. The classical path will be the dominant path for $h \rightarrow 0$, i.e., in the rod limit, and thermal fluctuations are taken into account by expanding the partition function in fluctuations around this classical path. The partition function will now be a path integral in curvilinear coordinates [119]:

$$Z = \int \mathcal{D}^2 [\theta, \phi] \sqrt{g(\theta)} e^{-\mathcal{E}[\theta(t), \phi(t)]} \quad (3.5)$$

The determinant of the metric in these coordinates is given by $g(\theta) = \cos^2 \theta$. The square root of this determinant, as present in the path integral measure, formally takes care of the coordinate independence (chart independence) of the measure. It can be understood in a time sliced version, although not without subtleties [119]. This measure term can also be formally exponentiated resulting in an extra energy term:

$$Z = \int \mathcal{D}^2 [\theta, \phi] e^{-\mathcal{E}[\theta(t), \phi(t)] - \mathcal{E}_m[\theta(t), \phi(t)]} \quad (3.6)$$

with the measure energy term:

$$\mathcal{E}_m[\theta(t)] = -\delta(0) \int_0^1 dt \log \cos \theta(t) \quad (3.7)$$

The delta function in front of the integral should be understood as being finite using some regularization scheme. The classical solutions are obtained through the Euler-Lagrange equations in the next section. We will then proceed by incorporating small fluctuations around these classical solutions in Section 3.4.

As we will see there are values of the coupling strength where several classical solutions exist with comparable Boltzmann weight. These give rise to a bifurcation point in the groundstate. Also since the potential term in (3.4) is positive, there are values of G for which the actual groundstate breaks the rotational symmetry around the direction of the applied force. The associated goldstone modes can be excluded by explicitly fixing a direction.

3.3 Euler buckling

In this chapter we consider as in Ref. [114] a molecule that has its two ends clamped at fixed orientations $\phi(0) = \phi(1) = \theta(0) = \theta(1) = 0$, while the ends can freely move in the plane

perpendicular to the force. In the zero fluctuation parameter limit the partition function gets only contributions from the classical paths, that minimize the energy. The Euler-Lagrange equations are:

$$\ddot{\theta}(t) = -\cos \theta(t) \sin \theta(t) \dot{\phi}^2(t) - G^2 \sin \theta(t) \cos \phi(t) \quad (3.8)$$

$$\frac{d}{dt} \left(\cos^2 \theta(t) \dot{\phi}(t) \right) = -G^2 \cos \theta(t) \sin \phi(t) \quad (3.9)$$

These equations can be integrated resulting in two classes of solutions: the straight rod solution

$$\theta(t) = 0 \quad \phi(t) = 0 \quad (3.10)$$

and the buckling solutions that read by choosing $\theta(t) = 0$

$$\dot{\phi}^2(t) = 2G^2(\cos \phi(t) - 1 + 2m), m \in [0,1) \Rightarrow \quad (3.11)$$

$$\phi(t) = 2 \arcsin(\sqrt{m} \operatorname{sn}(tG|m)) \Rightarrow \quad (3.12)$$

$$\cos \phi(t) = 1 - 2m \operatorname{sn}^2(tG|m) \quad (3.13)$$

Here $\operatorname{sn}()$ is an elliptic Jacobi function [120]. Solutions with $m > 1$ are solutions containing loops. They have a higher energy in our case. Using the periodicity properties of sn we find for buckling solutions with the boundary condition $\phi(1) = 0$ the following relation between m and f

$$G = L_c \sqrt{\frac{f}{P_b}} = 2n K(m) \quad n \in \mathbb{Z} \quad (3.14)$$

Here $K(m)$ is the complete elliptic integral of the first kind. We will label the solutions as ϕ_n , ϕ_0 corresponding to the straight rod. Since $K(m)$ is a monotonously increasing function of m we find a smallest force that permits a given buckling solution [121]:

$$f_c = G^2 \frac{P_b}{L_c^2} = n^2 \frac{4K(0)^2}{L_c^2} P_b = n^2 \frac{\pi^2}{L_c^2} P_b \quad (3.15)$$

It is straightforward to calculate the end-to-end distance along the z -axis by integrating the solution along the chain. The result is:

$$X = L_c \int_0^1 dt \cos \phi(t) = L_c \left(\frac{2E(m)}{K(m)} - 1 \right) \quad (3.16)$$

The value of the extension becomes negative under large enough compression. In practice we will be interested in the region where the force is small enough that the WLC model is still

reasonable. It is easy to see from the buckling solution (3.13) that the compressed chain will be a monotone curve as long as $m < 1/2$. For higher values of m the chain forms an s -shaped curve.

The energy of the buckling solution is found from equation (3.3) to be:

$$\begin{aligned}\mathcal{E}_n(m) &= \frac{G^2}{h} \left(2\frac{X}{L_c} + 2m - 1 \right) \\ &= \frac{4n^2 K^2(m)}{h} \left(4\frac{E(m)}{K(m)} + 2m - 3 \right)\end{aligned}\quad (3.17)$$

with m depending on the force, f , and n through equation (3.14). $E(m)$ is the complete elliptic integral of the second kind.

When comparing the energy of the buckled state with the straight rod configuration we notice that the buckled state is always energetically favorable once it is allowed by equation (3.15). This transition from straight rod to the buckled state is referred to as the Euler transition. When no other constraints are imposed on the solutions the first buckling solution, $n = 1$, will be the favorable solution under compression once the first critical value for the force has been reached [121]. When the end of the chain is constrained to be fixed in the origin of the YZ -plane, making both ends fixed on the z -axis, it is the one loop solution that, when there are no constraints on the rotation of the chain around its axis, is the favorable solution. We will for the rest of this article restrict ourself to the unconstrained case.

3.4 Semiclassical Buckling

For finite values of the fluctuation parameter thermal fluctuations must be taken into account in the evaluation of the partition function. We will write the coordinates as:

$$\theta(t) = \theta_n(t) + \delta\theta(t) = \delta\theta(t) \qquad \phi(t) = \phi_n(t) + \delta\phi(t) \quad (3.18)$$

Here the index $n \in \mathbb{Z}$ differentiates between the classical solutions (3.12),(3.14), the straight solution corresponding to $n = 0$. By plugging these relations into the expression for the total

energy (including the measure term) we find order by order:

$$\begin{aligned}
& \mathcal{E}[\theta(t), \phi(t)] + \mathcal{E}_m[\theta(t)] = \\
& \frac{1}{h} \int_0^1 dt \left\{ \frac{1}{2} \dot{\phi}_n^2 + G^2 \cos \phi_n \right\} \\
& + \frac{1}{h} \int_0^1 dt \left\{ \dot{\phi}_n \delta \dot{\phi} - G^2 \sin \phi_n \delta \phi \right\} \\
& + \frac{1}{h} \int_0^1 dt \left\{ \frac{1}{2} (\delta \dot{\phi})^2 - \frac{1}{2} G^2 \cos \phi_n (\delta \phi)^2 + \frac{1}{2} (\delta \dot{\theta})^2 - \frac{1}{2} (G^2 \cos \phi_n + \dot{\phi}_n^2) (\delta \theta)^2 \right\} \\
& + \dots
\end{aligned} \tag{3.19}$$

The first term is just the energy as given by equation (3.17) for the buckled solutions. The second term is zero when we look at chains with fixed boundary conditions (Dirichlet boundary conditions). The third term represents the lowest order that accounts for thermal fluctuations and is in the focus of our attention. Note that the measure term will only show up in the quartic order fluctuations (of order h), since for the Gaussian distribution the fluctuations are of order \sqrt{h} .

3.4.1 Harmonic fluctuations below the Euler transition

We first consider the regime below the critical force f_c , $G < G_c = \pi$, where the classical solution is the straight rod. The partition function to lowest order around this ground state has the simple form:

$$\begin{aligned}
Z = \exp(-G^2/h) \int \mathcal{D}[\delta\theta, \delta\phi] \exp \left\{ -\frac{1}{h} \int_0^1 dt \left(\frac{1}{2} (\delta \dot{\theta})^2 - \frac{1}{2} G^2 (\delta \theta)^2 \right) \right\} \\
\exp \left\{ -\frac{1}{h} \int_0^1 dt \left(\frac{1}{2} (\delta \dot{\phi})^2 - \frac{1}{2} G^2 (\delta \phi)^2 \right) \right\}
\end{aligned} \tag{3.20}$$

The resulting path integral is the product of the partition sums, in Euclidean time, of 2 independent harmonic oscillators with a frequency squared of $-G^2$. When we consider first the azimuth, ϕ , contribution, it is in fact a harmonic oscillator on the circle where angles that differ a full period are equivalent. The pathintegral in that case can be expressed as a sum over the harmonic oscillator on the real line by summing over all equivalent end points (see

e.g. [119] chapter 6):

$$Z_{\text{circle}}(\phi(0) = 0, \phi(1) = 0) = \sum_{n=-\infty}^{+\infty} Z_{\text{line}}(\phi(0) = 0, \phi(1) = 2\pi n) \quad (3.21)$$

$$= \frac{1}{\sqrt{2\pi h}} \sqrt{\frac{G}{\sin G}} \vartheta_3(0, e^{-2\pi^2 G \cot G/h}) \quad (3.22)$$

The elliptic theta function, $\vartheta_3(0, q)$ [122] diverges for $G = \pi/2$, only half the critical force, which seems to be odd at first sight. The reason behind this is that for $G = \pi/2$ all equivalent paths have the same weight, there is no cost in increasing the winding number. As a first correction we note that higher order corrections considerably temper the potential abyss for larger fluctuations in which case we can neglect the contributions from the winding by taking the domain of ϕ to be the real line. This results in an improved estimate for the partition sum:

$$Z_\phi = \frac{1}{\sqrt{2\pi h}} \sqrt{\frac{G}{\sin G}} \quad (3.23)$$

The same kind of reasoning holds for the polar angle. Here we do not have winding, but formally an oscillator in a box. Since we again assume the fluctuations to be small it is possible to extend the domain to the real axis. Although we have the equivalence $(\theta, \phi) \sim (\pi - \theta, \phi + \pi)$ again the results do not hold for larger fluctuations that have a weight that does differ substantially from zero. So by taking the polar angle also covering the real line we are only overcounting configurations that do not contribute to the path integral. The final result is then:

$$Z = \exp(-G^2/h) \frac{1}{2\pi h} \frac{G}{\sin G} \quad (3.24)$$

This partition sum diverges at the caustics, $G = \pi$. Note that this is exactly the critical point for Euler buckling. Here it is caused by the harmonic potential being just strong enough to cancel the kinetic term (i.e. the bending energy), making large fluctuations favorable and thus invalidating the harmonic approximation. Unlike the ϑ_3 -function divergence here we can not just dismiss these larger fluctuations, since they do not come from a topological disconnected region in configuration space and as such are indeed an indication that the groundstate is suffering from an instability.

The force extension behavior is readily obtained, as an approximation, from the partition function:

$$X(f) = -\frac{1}{Z} \frac{\partial Z}{\partial f} = L_c \left(1 - \frac{h}{2G^2} (1 - G \cot G) \right) \quad (3.25)$$

This expression diverges again at the Euler transition. Since we have approximated the total extension $X = L_c \int dt \cos \theta \cos \phi$ to quadratic order in the fluctuations around the classical solution, the deviation of the above expression for the extension from the straight rod actually gives, up to a factor L , the variance of the fluctuations averaged over the chain. When this variance is large, not only the harmonic approximation to the partition sum breaks down but the force extension approximation breaks down as well. From these considerations we expect the above given force-extension relation to hold as long as $\pi - G \gg h/2\pi$. From this observation one is tempted to conclude that the rod will start to buckle at a force shifted downwards from the Euler transition force following a scaling law for small h of :

$$f_c \sim f_c^{(0)}(1 - Ch) \quad (3.26)$$

with C a constant of order 1. This is a well known result from reference [114]. We will have to adjust this picture when taking higher order terms into account, as we will see in Section 3.5, because the linear scaling tells us only something about the validity of the quadratic approximation.

For small forces, $G \ll 1$, we find from equation (3.25) for the extension of the chain:

$$X(f) \cong L_c \left(1 - \frac{h}{6} \left(1 + \frac{G^2}{15} \right) \right) \quad (3.27)$$

For $G = 0$ this is the extension of the chain shortened by thermal fluctuations alone.

3.4.2 Harmonic fluctuations above the Euler transition

The harmonic correction to the classical solution has again the form of an harmonic oscillator, but now with a “time” dependent oscillator frequency. The azimuth and polar part of the fluctuation factor again decouple:

$$Z = e^{-\mathcal{E}_1(m)} F_\phi F_\theta \quad (3.28)$$

The classical solution is given by equation (3.17). In principle we should sum over all classical buckling solutions that are allowed at a given force. The energy difference is nonetheless big enough that we can neglect the contribution of higher buckled configurations.

The azimuth contribution has the form (after partial integration):

$$F_\phi = \int \mathcal{D}[\delta\phi] \exp \left(-\frac{1}{2h} \int_0^1 dt \delta\phi \hat{\mathbf{T}}_\phi \delta\phi \right) \quad (3.29)$$

with the harmonic fluctuation operator given by

$$\hat{\mathbf{T}}_\phi = -\frac{d^2}{dt^2} - G^2 \cos \phi_1(t) \quad (3.30)$$

where $\phi_1(t)$ is the classical $n = 1$ buckling solution. The fluctuation factor can be written using Gaussian integration in terms of functional determinants as:

$$F_\phi = \frac{1}{\sqrt{2\pi\hbar}} \left[\frac{\det(-\frac{d^2}{dt^2})}{\det(\hat{\mathbf{T}}_\phi)} \right]^{1/2} \quad (3.31)$$

The determinant of the fluctuation operator can be calculated using the Gelfand-Yaglom method as outlined in [119]. To do so we have to find a solution $D_\phi(t)$ of the differential equation

$$\hat{\mathbf{T}}_\phi D_\phi(t) = 0 \quad (3.32)$$

with boundary conditions $D_\phi(0) = 0$ and $\dot{D}_\phi(0) = 1$. The determinant $\det(\hat{\mathbf{T}}_\phi)$ is then given by $D_\phi(1)$. Changing variables to $x = Gt$ the differential equation has the form of a Lamé equation [123] (the Laplacian in ellipsoidal coordinates):

$$\frac{d^2 y(x)}{dx^2} + \{1 - 2m \operatorname{sn}^2(x|m)\} y(x) = 0 \quad (3.33)$$

With the given coefficients there exists one double periodic solution (also called Lamé polynomial) given by a Jacobi elliptic function

$$y(t) = \operatorname{cn}(Gt) \quad (3.34)$$

This solution has not the right boundary conditions, but using D'Alemberts construction [119], that gives another independent solution, we can construct the solution with the right boundary conditions:

$$\begin{aligned} D_\phi(t) &= y(t)y(0) \int_0^t \frac{dt'}{y^2(t')} \\ &= \frac{\operatorname{sn}(Gt|m) \operatorname{dn}(Gt|m) - E(Gt|m) \operatorname{cn}(Gt|m)}{G(1-m)} + t \operatorname{cn}(Gt|m) \end{aligned} \quad (3.35)$$

Here we adhere to the notation for the Elliptic Integral of the second kind as used in [120], see also Appendix A.1. The function dn is the last Jacobi elliptic function we need.

With this solution to the Lamé equation we find the fluctuation determinant as:

$$D_\phi := \frac{\det(\hat{\mathbf{T}}_\phi)}{\det(-\frac{d^2}{dt^2})} = D_\phi(1) = \frac{\operatorname{sn}(G|m) \operatorname{dn}(G|m) - E(G|m) \operatorname{cn}(G|m)}{G(1-m)} + \operatorname{cn}(G|m) \quad (3.36)$$

Now we can make use of the relation $G = 2 K(m)$ (3.14) to simplify this result to

$$D_\phi = \frac{E(m) - (1-m) K(m)}{(1-m) K(m)} \quad (3.37)$$

from which we obtain the fluctuation factor:

$$F_\phi = \sqrt{\frac{(1-m) K(m)}{2\pi h(E(m) - (1-m) K(m))}} \quad (3.38)$$

Since for small m , $E(m) - (1-m) K(m) \sim m\pi/4$, the fluctuation factor diverges at the Euler transition. This is not too surprising since in the 2 dimensional configuration, there are with forces close to the buckling transition three classical solutions with comparable energies with only small barriers in between, allowing larger thermal fluctuations than admissible for a harmonic approximation. Would we forbid out-of-plane fluctuations the picture is that fluctuations would grow with increasing force just below the Euler transition. Just above the Euler transition the chain will fluctuate between the two possible buckled configurations, analogous to quantum tunneling. Finally the buckling will stabilize with increasing force to one of the two configurations.

We now come to the out-of-plane fluctuations. The fluctuation determinants can again be calculated using the Gelfand-Yaglom method. We are now looking for a solution of (with $x = Gt$):

$$\frac{d^2 y(x)}{dx^2} + \{1 + 4m - 6m \operatorname{sn}^2(x|m)\} y(x) = 0 \quad (3.39)$$

This happens to be again a Lamé equation with the right coefficients to have a double periodic Lamé polynomial as solution:

$$y_0(x) = \operatorname{sn}(x) \operatorname{dn}(x) \quad (3.40)$$

Since $y_0(0) = 0$ we immediately find for the fluctuation determinant:

$$D_\theta := \frac{\det(\hat{\mathbf{T}}_\theta)}{\det(-\frac{d^2}{dt^2})} = \frac{\text{sn}(G) \text{dn}(G)}{G} \equiv 0 \quad (3.41)$$

and the partition sum diverges. This is caused by the global rotations around the force direction connecting a continuum of groundstates. The buckling solution (3.13) was chosen to be lying in the xy -plane. Since the energy (as well as the pathintegral measure) is invariant under rotations around the x -axis we have a continuum of buckling solutions. We can make use of this symmetry by integrating only over paths where the angle θ averages along the chain to zero and then integrating separately over the rotation around the x -axis. This can be done in a consistent way using the Faddeev-Popov (FP) method [124] developed to fix internal symmetries in quantum field theory. A clockwise rotation of the chain by an angle γ around the x -axis changes the coordinates on the sphere to:

$$\begin{aligned} \cos \theta \sin \phi &\rightarrow \cos(\theta_\gamma) \sin(\phi_\gamma) = \cos \theta \sin \phi \cos \gamma + \sin \theta \sin \gamma \\ \sin \theta &\rightarrow \sin(\theta_\gamma) = -\cos \theta \sin \phi \sin \gamma + \sin \theta \cos \gamma \end{aligned} \quad (3.42)$$

Now we want to fix the average of the θ angle, $\bar{\theta} := \int_0^1 dt \theta(t)$, to zero. We define the FP “determinant” through:

$$\Delta_{FP}[\theta, \phi] \int_0^{2\pi} d\gamma \delta(\bar{\theta}_\gamma) = 1 \quad (3.43)$$

where the argument of the delta function is the average angle of the by γ rotated chain. Inserting “1” into the partition sum (3.5) results in:

$$\begin{aligned} Z &= \int_0^{2\pi} d\gamma \int \mathcal{D}^2[\theta, \phi] \sqrt{g(\theta)} \Delta_{FP} \delta(\bar{\theta}_\gamma) e^{-\mathcal{E}[\theta(t), \phi(t)]} \\ &= 2\pi \int \mathcal{D}^2[\theta, \phi] \sqrt{g(\theta)} \Delta_{FP} \delta(\bar{\theta}) e^{-\mathcal{E}[\theta(t), \phi(t)]} \end{aligned} \quad (3.44)$$

In the last step we have first performed a trivial change of variable of integration and then made use of the invariance under rotation of the energy and of the pathintegral measure. In fact just the invariance of the combination of the measure and the Boltzmann factor would

have been enough. The FP determinant can be found from the defining equation (3.43) :

$$\begin{aligned}\Delta_{FP}[\theta, \phi] &= \left(\int_0^{2\pi} d\gamma \delta(\bar{\theta}_\gamma) \right)^{-1} \\ &= \left| \int_0^1 dt \sin \phi(t) \right| \end{aligned} \quad (3.45)$$

Since we are interested in small thermal fluctuations around the classical solution we can assume the fluctuations to be such that $\int dt \sin \phi(t) > 0$ for all relevant paths. This apparently does not hold anymore close to the bifurcation point. Defining Z_0 to be the partition sum without the FP term, but including the angle fixing delta function, the lowest order contribution of the FP term to the partition sum is:

$$\begin{aligned}Z &= \int_0^1 dt \langle \sin \phi(t) \rangle Z_0 \\ &\cong \int_0^1 dt \sin \phi_1(t) Z_0 \\ &= 2\sqrt{m} \int_0^1 y_0(Gt) Z_0 =: Z_{FP} Z_0 \end{aligned} \quad (3.46)$$

The last step follows from the definition of $\phi_1(t)$, see equation (3.13). We now fix the global polar angle in the polar fluctuation factor:

$$F_\theta := 2\pi Z_{FP} \int \mathcal{D}[\delta\theta] d(\delta\bar{\theta}) \exp \left(-\frac{1}{2h} \int_0^1 dt \delta\theta \hat{\mathbf{T}}_\theta \delta\theta \right) \quad (3.47)$$

To see how this procedure formally gets rid of the divergence we note first that the fluctuation operator, as defined on the square integrable functions on $[0, 1]$ that are zero on the boundary, is symmetric and so we can find a real orthonormal basis $\{\tilde{y}_n\}$ that diagonalizes the operator. Using this basis we write $\delta\theta(t) = \sum_{n=0}^{\infty} x_n \tilde{y}_n(Gt)$. The normalized zero mode eigenfunction is given by $\tilde{y}_0(Gt) = (\int dt y_0^2(Gt))^{-1/2} y_0(Gt)$ and the eigenvalues are written as λ_n , e.g.

$\lambda_0 = 0$. We now integrate separately over the zero mode:

$$\begin{aligned}
 F_\theta &= \frac{2\pi Z_{FP}}{\sqrt{2\pi h}} \left(\prod_{n \geq 0} \int \frac{dx_n}{\sqrt{2\pi h}} \right) \int \frac{dx_0}{\sqrt{2\pi h}} \delta\left(\sum_n x_n \int_0^1 \tilde{y}_n(t)\right) \exp\left(-\frac{1}{2h} \sum_{n \geq 1} x_n^2 \lambda_n\right) \\
 &= \frac{\sqrt{2\pi} Z_{FP}}{\sqrt{h} \left| \int_0^1 dt \tilde{y}_0(Gt) \right|} \frac{1}{\sqrt{2\pi h}} \left(\prod_{n \geq 0} \int \frac{dx_n}{\sqrt{2\pi h}} \right) \exp\left(-\frac{1}{2h} \sum_{n \geq 1} x_n^2 \lambda_n\right) \\
 &= \frac{2\sqrt{2m\pi} \int_0^1 dt y_0^2(Gt)}{\sqrt{h}} \lim_{\epsilon \rightarrow 0} \sqrt{\frac{\lambda_0^\epsilon}{2\pi h D_\theta^\epsilon}}
 \end{aligned} \tag{3.48}$$

In the last step we regularized the determinant by adding a small linear term:

$$\hat{\mathbf{T}}_\theta^\epsilon := \hat{\mathbf{T}}_\theta + \epsilon \hat{\mathbf{1}} \tag{3.49}$$

in effect shifting all eigenvalues λ_n by ϵ to the new values $\lambda_n^\epsilon = \lambda_n + \epsilon$. The resulting determinant is then, in first order in ϵ , ϵ times the determinant of the reduced operator defined on the orthogonal complement of the zero mode eigenvector, since all other linear terms contain the zero mode eigenvalue. The resulting homogeneous differential equation has been solved for a similar case in [125]. The somewhat technical calculation is done in Appendix A.2. The resulting determinant is:

$$D_\theta^\epsilon = \frac{\epsilon}{K(m)3m} ((1-m)K(m) - (1-2m)E(m)) \tag{3.50}$$

Finally the integral over the zero mode squared is given by:

$$\left(\int_0^1 dt y_0^2(t) \right)^{1/2} = \left(\frac{2}{3} [(1-m)K(m) - (1-2m)E(m)] \right)^{1/2} \tag{3.51}$$

Combining (3.38), (3.48), (3.50) and (3.51) we find for the partition sum:

$$Z = e^{-\varepsilon_1} \frac{2m K(m)}{\pi} \sqrt{\frac{(1-m)}{h^3 [E(m) - (1-m)K(m)]}} \tag{3.52}$$

It is noteworthy that the partition sum does not diverge at the Euler transition, but goes to zero. By approximating the Faddeev-Popov determinant by its classical value we are in fact underestimating the amount of configurations the closer we come to the bifurcation point. The force extension corrections to the classical force extension curve $X_0(f)$, equation (3.16), defined as $X = X_0 + X_\phi + X_\theta$, with the subscript labeling the fluctuation part that causes the extension change, are given by:

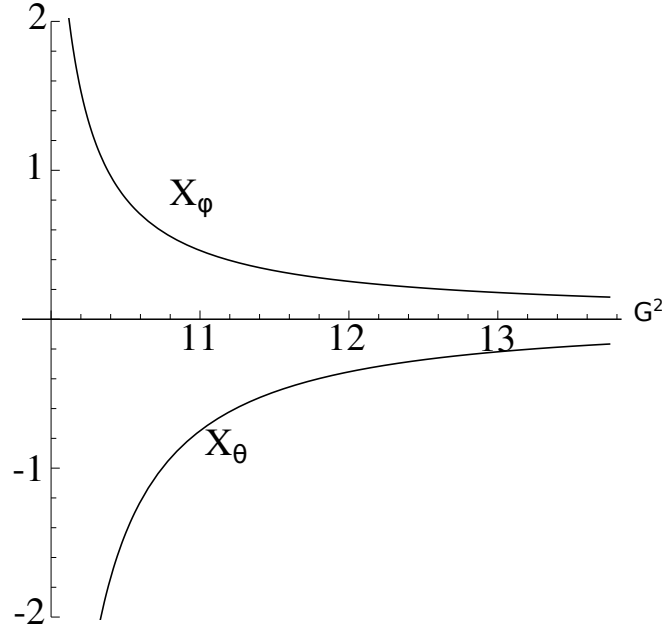


Figure 3.2: Relative extension shift from equation (3.53) with $h = L_c = 1$

$$\begin{aligned}
 X_\phi &\cong -\frac{1}{F_\phi} \frac{\partial F_\phi}{\partial f} = h L_c \frac{m K^2(m) - (K(m) - E(m))^2}{16 K^2(m)(E(m) - (1 - m) K(m))^2} \\
 X_\theta &\cong -\frac{1}{F_\theta} \frac{\partial F_\theta}{\partial f} = -h L_c \frac{E(m) + 3(1 - m) K(m)}{16 K^2(m)(E(m) - (1 - m) K(m))} \quad (3.53)
 \end{aligned}$$

These formula are not too illuminating. Plotting the two corrections (Fig. 3.2) reveals that the corrections to the extension caused by thermal fluctuations have an opposite sign. The out-of-plane fluctuations make the chain slightly shorter than the classical solution, as is to be expected. The in-plane fluctuations have the opposite effect. This can be understood as the extension change by fluctuations in the straight rod direction to be stronger than fluctuations away from the rod solution.

The total extension again diverges when approaching the bifurcation point, both for the X_ϕ and X_θ part separately. For the azimuth part the reason behind this is the same as in the straight rod case: near the bifurcation point fluctuations increase because the two classical solutions, of positive and negative angle, are close to each other and as such a quadratic approximation to the force term is not enough. For the polar angle this is not the case since we integrated out the fluctuations to equivalent states, but there the FP term (3.46) is underestimated: as long as the deviation of the expectation value of the end point of the chain (proportional to the FP term) from the straight rod is larger than its fluctuations we can expect that our results hold. Close to the bifurcation point however, we are not allowed to drop the absolute value sign by

going to equation (3.46) and find a lower bound of the FP term in the order of the standard deviation of the end point.

For small m , approaching the bifurcation point, we find from (3.53):

$$\begin{aligned} X_\phi &= \frac{h L_c}{\pi^2 m} \left(1 - \frac{m}{2} + \mathcal{O}(m^2) \right) \\ X_\theta &= -\frac{h L_c}{\pi^2 m} \left(2 - \frac{5m}{2} + \mathcal{O}(m^2) \right) \end{aligned} \quad (3.54)$$

Like below buckling the extension diverges because we make an approximation by taking the extension to be $-\partial_f \log Z$. This is not exact when approximating the potential. For the same reasons as below buckling we can expect the results not to hold for large relative extension shifts.

3.5 Quartic order

Below buckling it is fairly simple to get a good estimate of the force extension curve up to the Euler transition by taking higher order fluctuations into account. Since it is the lowest mode that is responsible for the blowing up of the partition sum, approaching the transition, we can significantly improve the calculations by including the quartic term for this mode. Quartic terms containing other modes hardly improve upon this. In 2 dimensions the corrected partition sum is:

$$\begin{aligned} Z &= \frac{e^{-G^2/h}}{\sqrt{2\pi h}} \sqrt{\frac{G(\pi^2 - G^2)}{\sin G}} \int_{-\infty}^{\infty} \frac{dx}{\sqrt{2\pi h}} \exp\left(-\frac{1}{2h}(x^2(\pi^2 - G^2) + x^4 \frac{G^2}{8})\right) \\ &= \frac{e^{-G^2/h}}{\sqrt{2\pi h}} \sqrt{\frac{G(\pi^2 - G^2)}{\sin G}} \frac{\gamma}{2\tau \sqrt{\pi h}} e^{\frac{\gamma^4}{2\tau^2}} K_{\frac{1}{4}}\left(\frac{\gamma^4}{2\tau^2}\right) \end{aligned} \quad (3.55)$$

with

$$\tau = \frac{G}{4\sqrt{h}} \quad \gamma = \frac{\sqrt{\pi^2 - G^2}}{2\sqrt{h}} \quad (3.56)$$

from which we find for the force extension relation:

$$\begin{aligned} X_\gamma = L_c \left\{ 1 - \frac{h}{2G} \left[\frac{\pi^2 - 3G^2}{2G(\pi^2 - G^2)} - \frac{\cot G}{2} + \frac{1}{\gamma} \frac{d\gamma}{dG} - \frac{1}{\tau} \frac{d\tau}{dG} \right. \right. \\ \left. \left. + \left(2 - \frac{K_{3/4}(\frac{\gamma^4}{2\tau^2}) + K_{5/4}(\frac{\gamma^4}{2\tau^2})}{K_{1/4}(\frac{\gamma^4}{2\tau^2})} \right) \frac{\gamma^4}{2\tau^2} \left(\frac{2}{\gamma} \frac{d\gamma}{dG} - \frac{1}{\tau} \frac{d\tau}{dG} \right) \right] \right\} \end{aligned} \quad (3.57)$$

These solutions can be continued up to the transition. The more practical use of these calculations is to make an estimate of the forces a rod can endure, before it collapses. Assuming $h \ll 1$, so that we are close to a buckling type of behavior, we can recognize two separate asymptotic regions of behavior, depending on the argument of the modified Bessel functions in (3.57):

- $\pi^2 - G^2 \ll G\sqrt{h}$ we find as asymptotic behavior:

$$X \simeq L_c \left(1 - \frac{2\sqrt{2}}{\Gamma(1/4)^2} \sqrt{h} + \left(\frac{2}{\pi} + \frac{2\sqrt{2}\Gamma(-1/4)}{\Gamma(1/4)^3} + \mathcal{O}(\sqrt{h}) \right) (\pi - G) + \mathcal{O}((\pi - G)^2) \right) \quad (3.58)$$

i.e. X exhibits a finite negative slope. The decrease of the extension with increasing force is substantial. The polymer can be considered to buckle.

- $\pi^2 - G^2 \gg G\sqrt{h}$: In this region the decrease of the extension is of order h , the force extension curve being almost flat. There is no buckling yet.

The crossover region and thus the region where one could speak of a buckling transition, is where this argument is of order unity. It is of course not possible to pinpoint a precise transition point, but the scaling of the transition shift follows from these observations: the force where the instability appears is shifted by thermal fluctuations according to:

$$f_c \sim f_c^{(0)}(1 - C\sqrt{h}) \quad (3.59)$$

with C of order unity. The results for 5 different values of h are drawn in Figure 3.3 together with the corresponding reduced transition forces using $C = 0.5$. We next consider the 3d case. The contribution from the θ part alone is the same as for the ϕ part, which would result in a doubling of the difference from the straight rod. But now we also have a term mixing the two lowest modes. The fluctuation part of the partition sum is (apart from a constant):

$$Z_{fl} = \frac{G(\pi^2 - G^2)}{\sin G} \iint_{-\infty}^{\infty} \exp\left(-\frac{1}{2h}(x^2\lambda_1 + x^4\frac{G^2}{8} + z^2\lambda_1 + z^4\frac{G^2}{8} + x^2z^2(\frac{3G^2}{4} - \frac{\pi^2}{2}))\right) dx dz \quad (3.60)$$

As first approximation we can use the expectation value of the square of one of the modes, resulting in a modified γ for the other mode given by:

$$\bar{\gamma} = \frac{1}{2\sqrt{h}} \sqrt{\pi^2 - G^2 + \langle z^2 \rangle \frac{(3G^2 - 2\pi^2)}{4}} \quad (3.61)$$

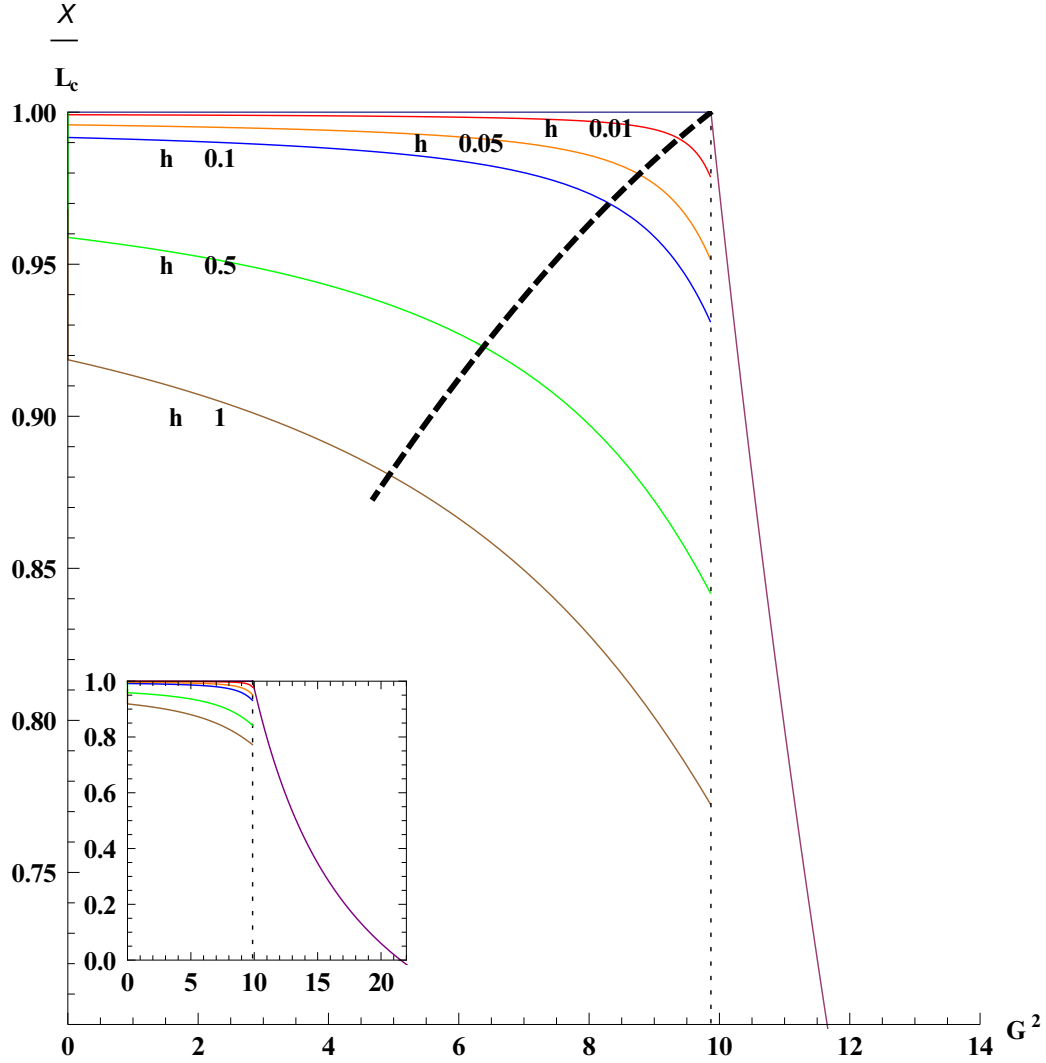


Figure 3.3: Details from the force extension plot in 2-d for $h = 0.01, 0.05, 0.1, 0.5$ and 1 calculated from equation (3.58). The inset shows the full plot. The purple line is the classical $h = 0$ curve, the thin dotted line the Euler bifurcation. The thick dashed line shows the trend of the transition force calculated from equation (3.59), with $C = .5$.

with:

$$\langle z^2 \rangle = \left(\frac{K_{3/4}(\frac{(\pi^2 - G^2)^2}{2hG^2}) + K_{5/4}(\frac{(\pi^2 - G^2)^2}{2hG^2})}{2 K_{1/4}(\frac{(\pi^2 - G^2)^2}{2hG^2})} - 1 \right) \frac{2(\pi^2 - G^2)}{G^2} - \frac{h}{\pi^2 - G^2} \quad (3.62)$$

The resulting extension is then given by:

$$X = X_\gamma + X_{\bar{\gamma}} - L_c \quad (3.63)$$

This approximation slightly overestimates the contribution of the mixing term close to the transition, where the behavior is far from Gaussian. A better result can be obtained by treating the mixing term as a perturbation and expanding equation (3.60). The resulting series expansion one obtains is:

$$Z_{fl} = \frac{G(\pi^2 - G^2)}{\sin G} \sum_{n=0}^{\infty} \frac{1}{n!} \left(-\frac{3G^2 - 2\pi^2}{8h} \right)^n \left(\frac{\tau \Gamma(\frac{2n+1}{4}) \Phi(\frac{2n+1}{4}, \frac{1}{2}, \frac{\gamma^4}{\tau^2}) - 2\gamma^2 \Gamma(\frac{2n+3}{4}) \Phi(\frac{2n+3}{4}, \frac{3}{2}, \frac{\gamma^4}{\tau^2})}{2\tau^{(2n+3)/2}} \right)^2 \quad (3.64)$$

with $\Phi(x, y, z)$ Kummer's function (confluent hypergeometric function). This series converges relatively fast just below the Euler transition and one can get a good approximation of the extension below the transition force. For practical purposes the first approximation is good enough to characterize the transition shift. It scales with increasing length in the same way as the $2d$ case. We will next compare the predictions of the force-extension relations, eqs. (3.25), (3.53), (3.58), (3.63) and (3.64), with simulations.

3.6 Comparison with the simulation

Molecular dynamics simulations coupled to a Langevin thermostat were performed to simulate the buckling of a semi-flexible polymer at finite temperature. The polymer was modeled with a bead spring model of length 50 beads (49 bond lengths). The beads were connected via harmonic bonds with stiffness constant $100 k_B T$. Additional simulations with a FENE potential [126, 127] instead of a harmonic potential gave qualitatively similar results (not shown). A cosine angular energy term was added to the model to obtain a semi-flexible chain with persistence length comparable to the chain length. The backbone stretching parameters were chosen such that fluctuations of the bond length are negligible compared to the bending fluctuations. Therefore, the inextensible worm-like chain model is expected to be a good approximation to the simulated chain.

The simulations and theoretical calculations are plotted in Figure 3.4. The value of h was taken rather high in order to have a more pronounced fluctuation contribution. The length scale is chosen such that the bond length in the simulation model is 1. The 3-d quartic curve was calculated using the modified quartic term.

The semi-classical results are in good agreement with the simulation data in the region where a semi-classical approximation is expected to be valid. It is noteworthy that the increase

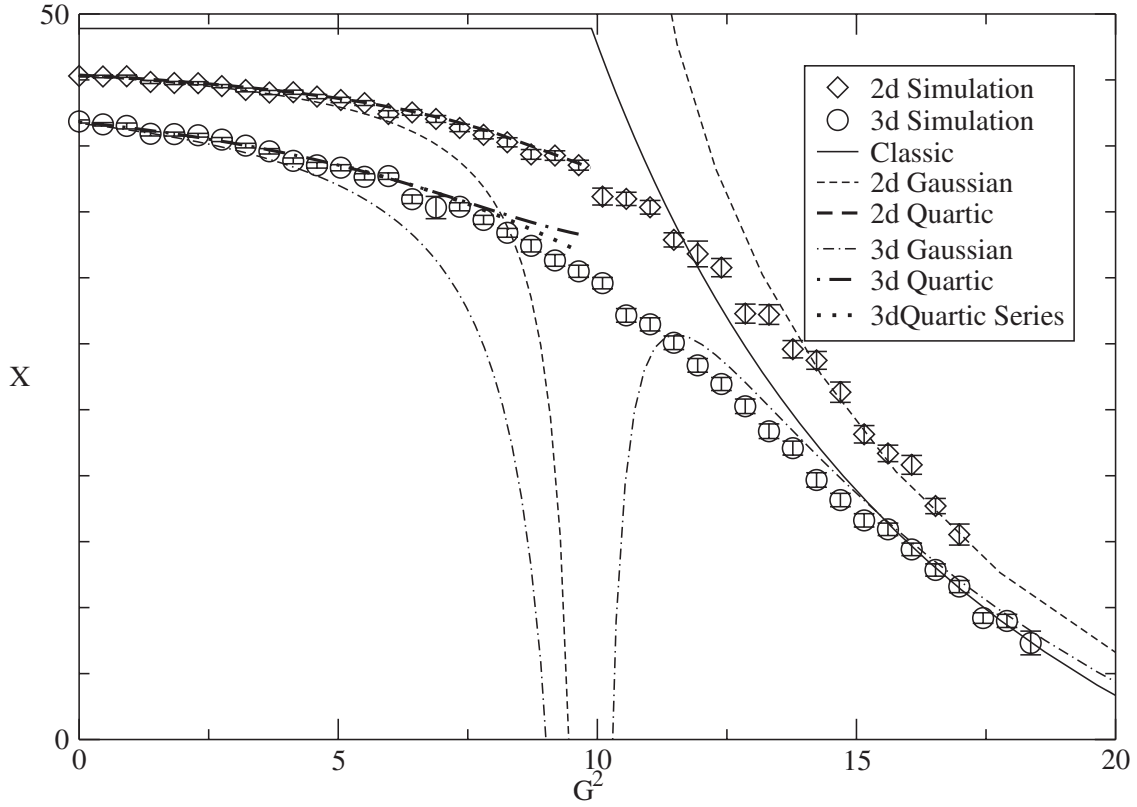


Figure 3.4: Comparison of the analytical force-extension with simulations for $L_c = 49$ and $h = 0.8$. The unit of length is the bond length in the simulation.

in extension as predicted by the calculations is indeed the same as observed in the simulation. In $2d$ the quartic corrections below buckling are seen to be, even for relatively large values of h , in good agreement with simulations. In $3d$, using the simplified approach of modifying the quartic interaction to account for the mode mixing (3.63) the reliability of the calculations close to the Euler transition decreases, although the qualitative behavior seems to be good enough for practical purposes. Better results are seen if the perturbation expansion (3.64) is used. The 3-d quartic series curve was calculated using this expansion with the first 20 terms. Note though that this last calculation was stopped slightly below the transition force, since it does not converge at the transition.

The effect of the bond length not being fixed is indeed small enough compared to the thermal fluctuations. The errorbars are caused by the finite number of simulation rounds.

3.7 Discussion

The parameter that determines whether a buckling transition is present is the ratio h of length and persistence length of the wormlike chain. One can roughly say that a buckling transition appears for ratios clearly smaller than 1. But it is crucial that one takes into account the shift of the apparent transition when a force is extracted from the onset of buckling. To illustrate the importance of thermal fluctuations we will discuss the influence they have in interpreting data from recent experiments with important biopolymers. Table 3.1 shows the persistence length of the 3 polymers, ds-DNA, actin and Microtubule together with some of the typical lengths and associated transition forces. The shifted transition force is calculated from equation (3.59) with $C = 1$.

The DNA tetrahedra synthesized by Goodman et.al. [116] have sides made of double stranded DNA of a length below 10 nm. As can be read of from the table, for a lengths of 10 nm the force the structure can endure is strongly reduced by thermal fluctuations. This has to be taken into account when designing nanostructures based on DNA.

F-actin is one of the main building blocks of the cytoskeleton. It has a persistence length in the order of 9 to 18 μm [128] (the higher value is in presence of the toxin Phalloidin). Actin can produce forces through polymerization. The maximum force it can produce, the stall force, was determined by Kovar et.al. [112] by measuring the shortest length of actin that showed buckling, when growing in between 2 fixed points. The lengths where this was observed are given in row 2 and 3 of the table. The force calculation based on classical buckling considerably overestimates the force needed to buckle for the measured length since it does not take the thermal fluctuations into account.

The other important structures in the cytoskeleton are microtubules, hollow highly regular assemblies of filaments, having persistence lengths in the order of several μm 's [128], the precise value depending on several factors, like the growth speed [111] and perhaps the contour length [129]. In buckling experiments by Janson et.al. [111], where the growth rate dependence on the applied force was studied, the lengths were such that in this case the shift by thermal fluctuations is negligible. Nevertheless, the increase of thermal fluctuations

when approaching buckling can also be observed in this case. These thermal fluctuations increase sharply just before buckling, followed by a strong damping of these fluctuations with increasing length (and thus increase of buckling) of the microtubule. Both these effects follow from our calculations.

The damping of the fluctuations after the onset of buckling can be inferred from the approach of the semiclassical solution towards the “zero temperature” classical solution. Below buckling the end point fluctuations increase from $\langle y^2 \rangle \cong L_c^2 h/3$, the classic result which follows from equation (3.27), for a chain with one free end to $\langle y^2 \rangle \approx 0.2 L_c^2 \sqrt{h}$ for an applied force corresponding to the Euler transition, as follows from equation (3.58). It should be noted that the geometry of the setup in those experiments is not immediately comparable to our calculations: in the experiments the microtubule has one end of the chain more or

Table 3.1: Reduction of the force needed to buckle for some biopolymers with finite length. The reduction is calculated from equation (3.59) with $C = 1$

	$P_b(\text{nm})$	$L_c(\text{nm})$	h	$f_c^{(0)}(\text{pN})$	$f_c(\text{pN})$
DNA	50	10	0.2	21	11
actin	9×10^3	1.2×10^3	0.13	0.26	0.16
actin with Phalloidin	18×10^3	0.75×10^3	0.04	1.3	1.0
Microtubule	3.3×10^6	9.4×10^3	0.028	1.5	1.4

less hinged in a fixed position. The resulting buckling force can be up to a factor 4 larger than in our case. Qualitatively though the results are comparable and for typical values of a persistence length of 3.3 nm and a chain length of 20 μm we expect the mean fluctuation of the end point to be amplified by a factor ≈ 7 . This indeed seems to be approximately the case, although a precise analysis of their measurements is outside of the scope of this paper.

Finally, a remarkable result of our calculations is the increase of end-to-end distance by thermal fluctuations of the buckled polymers, especially in 2 dimensions. In dense networks of actin filaments confined to the cell cortex, the buckling is approximately 2-dimensional. The lengthening of the buckled polymer causes then an apparent stiffening of the compressed network by the fluctuations.

The Writhe of a Curve

When an elastic rod is put under torsional stress, it responds by increasing the twist. To define twist we need more than just the tangent of the rod as it was done in the WLC model from the last chapter. There are two equivalent ways for describing a rod under torsional stress. One is to describe the rod as a ribbon: two space curves close to each other, for example one describing the mid-line of a semiflexible chain, the other along the outer surface of the chain. The other option is a framed curve: a space curve plus a smooth choice of a $3d$ orthonormal basis at each point of the space curve, one the tangent \mathbf{t} , the other two an orthonormal basis of the normal plane at that point. With a smooth choice we mean that the rotation of the basis when going along the chain is smooth, in mathematical terms a smooth section of the orthonormal frame bundle of \mathbb{R}^3 . We get the connection between the two definitions when we choose one of the vectors in the normal plane, \mathbf{u} , to point to the partner curve of the ribbon. The twist can now be defined as the integral over the differential rotation of the frame.

It is clear from the definition that the choice of the ribbon is arbitrary. From a physical point of view it is practical to choose the curves to be parallel when they are fully relaxed¹. But this last sentence makes only sense when the center curve is straight, or at most planar. This fact is a sign of the problems lying ahead.

When we keep one end of the rod fixed and start to rotate the other, twist will build up in the chain and the energy will go up, assuming linear elastic response, as:

$$\mathcal{E}_{tw} = \frac{P_c}{2} \int_0^{L_c} (\Delta\psi(s))^2 ds \quad (4.1)$$

The reduced modulus P_c is called the torsional persistence length for obvious reasons. $\Delta\psi := (\mathbf{t} \wedge \mathbf{u}) \cdot \dot{\mathbf{u}}$ is the differential change in the angle of the frames, the local twist angle. The twist is defined as the number of turns the frame rotates around the tangent

¹Most semiflexible polymers have a helical structure and it is a common choice to include the helical twist in the definition of the chain's twist, but we choose not to do so.

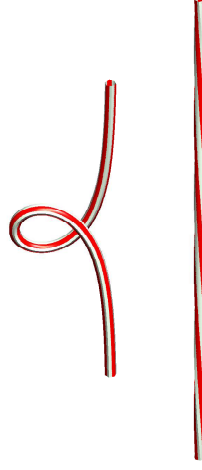


Figure 4.1: Applying one full turn to one chain end of a straight relaxed chain, while keeping the other end fixed, results in a loop but no twist on the left whereas the right hand side has all of the linking in the form of twist

direction integrated over the chain:

$$\text{Tw} = \frac{1}{2\pi} \int_{-L_c/2}^{L_c/2} ds \Delta\psi(s) \quad (4.2)$$

To start from ψ as an angle is not so useful since its value at some point along the curve can only be calculated relative to the value at another point by integration. There is no local way to measure it. That is why this notation was chosen. Next to twisting, the rod has also another option to respond to torsional stress: it can curve out of the plane, as shown in Figure 4.1. When following the local frame along the contour in the twisted chain, it is rotating gradually around the tangent vector. In the left hand configuration no such rotation occurs, nonetheless the two ribbon lines are in the same way entangled. The problem of how to know how much the lines of a closed ribbon are entangled was to a large extent solved by Călugăreanu [130, 131, 132], later refined by Pohl [133] and White [134]. The starting point was Gauss formula for the linking number of 2 links, or loops.

$$\text{Lk} = \frac{1}{4\pi} \oint_{S^1} \oint_{S^2} \frac{d\mathbf{r}_1 \wedge d\mathbf{r}_2 \cdot (\mathbf{r}_1 - \mathbf{r}_2)}{|\mathbf{r}_1 - \mathbf{r}_2|^3} \quad (4.3)$$

The integral is an integer counting the number of times one link crosses the other when projected in a general direction, counting with sign which link passes on top. There are several ways to prove this. A physical way is to use standard vector identities [135] to write it as the integral over the surface spanned by one loop over a signed delta function that

counts the passing over the other link through it [136]. The expression closely resembles the Biot-Savart law of magneto-statics and one can think of the links as representing magnetic flux [137]. An astronomer would perhaps think of the measurement of the solid angle a planet orbit describes as seen from earth [138] as follows:

Imagine you are watching the motion of a distant comet in its orbit around the sun. Assume for the moment that your planet has a fixed position. In that case follows the unit vector pointing in the comets direction a closed path enclosing some area on the unit sphere. Now your planet is moving in its own orbit. The area that you measure from another point along your orbit changes. To be able to know how big a map is needed to draw the movement of the comet, it is worthwhile to keep track of the differential change in orbit area. Since also your orbit is closed, it seems to be that the integral should add up to zero when going around your orbit. But when the orbit of the comet at some point goes over your head, the area swept out growing over 2π , there are two possibilities: either at another point it shrinks again below 2π , or it keeps on growing reaching the complement of the original area when returning to the start position. That last case happens when the orbits are linked.

A more modern way to understand this is by way of the degree of an orientation preserving map f from an oriented closed surface M to the unit-sphere:

$$f : M \rightarrow S^2 \quad \deg f = \frac{1}{4\pi} \int_M f^* \omega, \quad (4.4)$$

with ω being the volume 2-form on S^2 , f^* the pullback to M . The degree of a map is an important concept with many useful applications in physics. In case M is a regular surface embedded in three dimensional Euclidean space and f the Gauss map, mapping each point of M to the outward surface normal, the integral is the Gaussian curvature integrated over the surface. The degree of this map tells us that this integrated Gaussian curvature integrated over the closed surface is quantized. This is the Gauss-Bonnet theorem [139]. It has important consequences for the physics of membranes and shells for it makes it possible to drop the Gaussian curvature elasticity contributions from the Hamiltonian from one component liquid membranes to crystalline virus shells.

To make the connection with the linking number we refer to the astronomer observing another orbit from its own. M is in this case the Cartesian product of the two orbits and f maps to the unit vector on the direction sphere pointing from one orbit to the other:

$$f : C_1 \times C_2 \rightarrow S^2 \quad f(\mathbf{r}_1(s), \mathbf{r}_2(t)) = \mathbf{e}_{12}(s, t) = \frac{\mathbf{r}_1(s) - \mathbf{r}_2(t)}{|\mathbf{r}_1(s) - \mathbf{r}_2(t)|}. \quad (4.5)$$

The infinitesimal change of $\mathbf{e}(s, t)$ is in the tangent plane of the direction sphere, since \mathbf{e}_{12} is a unit-vector. The infinitesimal area is the norm of the cross product of the two independent directions, or zero. But the crossproduct is directed along the outward normal and so we find

Table 4.1: Properties of the 3 parts of White's equation

	Linking	Twist	Writhe
topological invariant	yes	no	no
locally defined	no	yes	no
needs a frame	yes	yes	no
(gauge invariant	no	no	yes)

for the degree:

$$\text{Lk} = \frac{1}{4\pi} \oint_{S^1} ds \oint_{S^2} dt \left(\frac{\partial \mathbf{e}_{12}(s, t)}{\partial s} \wedge \frac{\partial \mathbf{e}_{12}(s, t)}{\partial t} \right) \cdot \mathbf{e}_{12}(s, t) \quad (4.6)$$

It is not hard to convince yourself that this is exactly the Gauss integral. Since all maps are continuous, all continuous deformations that keep the surface regular, meaning non-intersecting deformations, do not change this number. It must be a topological invariant.

The same procedure can be repeated when the two links, the maps $\mathbf{r}_{1,2}$, coincide, resulting in an intrinsic linking number of a link, called the writhe. The argumentation is the same except that f can only be defined on the product space without the diagonal, the set of points in $S^1 \times S^1$ of the form (s, s) , the direction from a point of the link to another, being undefined when the points coincide. In fact the direction becomes the tangent when approaching the diagonal, but flips direction from one side of the diagonal to the other side. The torus without diagonal is homeomorphic to a cylinder or a disk with a hole cut out in the center. The resulting integral exists though but is not integer valued and varies continuously upon deformation. The big breakthrough that started with Călugăreanu's papers was the discovery of what is now usually called White's theorem relating the Gauss integral of a link with itself, or the writhe, with the linking number and twist of the framed link:

$$\text{Lk} = \text{Tw} + \text{Wr} \quad (4.7)$$

Here the linking number is the conventional linking number, as defined by the Gauss inte-

gral (4.5), for the two ribbon curves, and the twist the integrated differential rotation of the frame around the tangent. It is more remarkable than it looks since the linking number is an integer and a topological invariant, whereas the other quantities are continuous real valued functions. The twist as a local rotation of the ribbon curves around each other is also not preserved under smooth deformations. A local inhabitant, wanting to make a tour around the world could put a stick at the start of the tour pointing in some well defined direction normal to the curve, could carefully keep track of the direction he chose by not rotating around the

tube and still ending in a different direction, making on the way theories about mysterious forces. Table 4.1 gives an overview of the different properties.

So White's theorem tells us that the two quantities twist and writhe when added form a topological invariant. That it is the linking number can be seen by flattening the link on a plane in a continuous way without breaking it anywhere. For our use it is enough to assume the link is a trivial knot, so we can flatten it to a circle, otherwise there are standard moves to unknot a knot keeping track of the change in linking number. The writhe is clearly zero so the linking number must be equal to the twist.

It is also possible to give an intrinsic unified way to calculate linking number, writhe and twist [140]. One starts assigning a direction to the ribbon. Next one counts the number of times one line of the ribbon crosses the other as seen from a projection and averages over all directions. When the lines cross at the same spot of the ribbon it is contributing to the twist, else to the writhe. Both contribute to the linking number. Some care has to be taken about the multiplicity of the counting.

One way to proof White's theorem is to regularize the singular points by choosing a canonical ribbon. One common choice is the direction of curvature, defining the principal normal of the Frenet frame, or alternatively the remaining, bi-normal. The disadvantage is that this presumes a non vanishing curvature. A more elegant choice is the writhe frame, adjusting the frame and thereby the twist, at a point s along the link as follows [140]: The chords starting from s , the chord fan, define a, possibly complicated, path on the direction sphere from $\mathbf{t}(s)$ to $-\mathbf{t}(s)$. Choose the frame normal \mathbf{u} , connecting s with its ribbon point, such that the semicircle from $-\mathbf{t}(s)$ to $\mathbf{t}(s)$ via this normal, closes the path to a loop on S^2 with an enclosed area of zero (mod 4π). The claim is that this zero is the linking number of the resulting ribbon.

$$0 := \frac{1}{4\pi} \oint (\text{full loop at } s) = \frac{1}{4\pi} \int_0^{L_c} dt \left(\frac{\partial \mathbf{e}(s, s+t)}{\partial s} \wedge \frac{\partial \mathbf{e}(s, s+t)}{\partial t} \right) \cdot \mathbf{e}(s, s+t) \\ + \frac{1}{4\pi} \int_0^\pi d\phi \left(\frac{\partial \mathbf{v}(s, \phi)}{\partial s} \wedge \frac{\partial \mathbf{v}(s, \phi)}{\partial \phi} \right) \cdot \mathbf{v}(s, \phi), \quad (4.8)$$

with the unit vector $\mathbf{v} = -\mathbf{t}(s) \cos(\phi) + \mathbf{u}(s) \sin(\phi)$ following the geodesic set by $\mathbf{u}(s)$, chosen to have an enclosed area of zero (mod 4π). With $\mathbf{u}(s)$ as ribbon normal, the second term equals:

$$\frac{1}{4\pi} \int_0^\pi d\phi \left(\frac{\partial \mathbf{v}(s, \phi)}{\partial \phi} \wedge \mathbf{v}(s, \phi) \right) \cdot \frac{\partial \mathbf{v}(s, \phi)}{\partial s}, \\ = \frac{1}{4\pi} \int_0^\pi d\phi (\mathbf{t}(s) \wedge \mathbf{u}(s)) \cdot (-\dot{\mathbf{t}}(s) \cos(\phi) + \dot{\mathbf{u}}(s) \sin(\phi)) \\ = \frac{1}{2\pi} (\mathbf{t}(s) \wedge \mathbf{u}(s)) \cdot \dot{\mathbf{u}}(s) \quad (4.9)$$

which is the local twist. We still have to show that equation (4.8) is indeed the inner loop integral of the linking number. The second ribbon curve is defined as $\mathbf{r}_2(s) = \mathbf{r}(s) + \epsilon \mathbf{u}(s)$ with ϵ small enough to prevent intersections. The linking number is a topological invariant so we are free to take the limit $\epsilon \downarrow 0$ in the end without changing its value. When we integrate equation (4.6) over t , keeping s fixed, we can distinguish two different regimes.

1. When $\mathbf{r}(t)$ is far away from $\mathbf{r}(s)$, compared to the distance of the two ribbon curves, the integrand can be approximated by that of the writhe part of equation (4.8).
2. When the distance between the points is much smaller than the ribbon width the integrand lies approximately on the arc of the twist part, its position on the arc describing half a turn.

Although the intervals for the second regime shrink with decreasing ϵ , the contribution to the full integral approaches that of the twist part. When ϵ goes to zero the two loop integrals are the same. This proves White's relation since this limiting procedure does not change Lk. Note that nowhere we needed to have 0 on the left hand side of equation (4.8). In a way the writhe term can be seen as the writhe at s , but it depends on the rest of the link.

As a final remark: all 3 of the quantities measure areas on the unit sphere. With the total area swept out by the ribbon cross chords given (Lk) it can be divided in a local (Tw) and a nonlocal (Wr) part. Another way to think about it is as follows: given a space curve there is a gauge freedom of choosing a smooth section in the frame bundle. As seen from the space curve it is the writhe that is the gauge invariant quantity. These concepts show a strong resemblance to other geometric phases like Berry's phase and the Aharonov-Bohm effect.

The writhe being nonlocal complicates perturbation calculations enormously. Under certain conditions it is nonetheless possible to turn the writhe into a local quantity. We will call two links writhe-homotopic if: (i) they are homotopic as non-intersecting space curves and (ii) the tangent along the homotopy is nowhere anti-parallel to one of the end curves. Fuller showed [141, 142] how to relate the writhe of 2 writhe-homotopic links, with writhes $Wr_{1,2}$, in a local way. When discussing White's relation we noted that the linking number measures the area swept out by the chords. The writhe is a measure of the area swept out by the tangent, A_t , when traversing the curve. Fuller showed [141]:

$$Wr = \frac{1}{2\pi} A_t + 1 \bmod 2 \quad (4.10)$$

from that observation he gave arguments for a local expression of the writhe difference. We will sketch the derivation along the lines of Aldinger et al. [142] and refer for the details to that paper.

The homotopy we write as $\mathbf{r}_t(s)$ with end-links $\mathbf{r}_1(s) = \mathbf{r}(s, 0)$ and $\mathbf{r}_2(s) = \mathbf{r}(s, 1)$. The main idea is that this homotopy, when framed continuously, can not change its topologically invariant linking number, and so the *nonlocal* calculation of the writhe difference can be replaced by a *local* calculation of the twist difference. They are in that case equal with

opposite sign. We are free to choose the framing along the homotopy as long as the framing itself also changes continuously in t . We first construct a framing for the start and end link by choosing frame normals common to both links:

$$\mathbf{u}_0(s) = \mathbf{u}_1(s) := \frac{\mathbf{t}_0(s) \wedge \mathbf{t}_1(s)}{|\mathbf{t}_0(s) \wedge \mathbf{t}_1(s)|} \quad (4.11)$$

This fails at s -points where the tangents are parallel. To overcome this we can infinitesimally distort the start link at these points. We will see in the end that the final result only depends on the tangents of the start and end loop and we can remove the distortion. Along the homotopy we will rotate the frame normals with the tangent rotations [143]:

$$\mathbf{u}_t(s) = \mathbf{u}_0(s) + \sin(\phi)(\mathbf{n}_t(s) \wedge \mathbf{u}_0(s)) + 2 \sin^2\left(\frac{\phi}{2}\right)(\mathbf{n}_t(s) \wedge (\mathbf{n}_t(s) \wedge \mathbf{u}_0(s))) \quad (4.12)$$

with ϕ the angle between the tangents at s , and n the common normal:

$$\mathbf{n}_t(s) = \frac{\mathbf{t}_0(s) \wedge \mathbf{t}_t(s)}{|\mathbf{t}_0(s) \wedge \mathbf{t}_t(s)|} \quad (4.13)$$

We have now constructed a ribbon homotopy with a writhe homotopic centerline. The twist difference is easy to calculate, using the standard vector identity [135]:

$$\mathbf{v}_1 \wedge (\mathbf{v}_2 \wedge \mathbf{v}_3) = (\mathbf{v}_1 \cdot \mathbf{v}_3)\mathbf{v}_2 - (\mathbf{v}_1 \cdot \mathbf{v}_2)\mathbf{v}_3,$$

namely:

$$\begin{aligned} \text{Wr}_2 - \text{Wr}_1 &= \text{Tw}_1 - \text{Tw}_2 \\ &= \frac{1}{2\pi} \oint ds \left[(\mathbf{t}_1(s) - \mathbf{t}_2(s)) \wedge \left(\frac{\mathbf{t}_1(s) \wedge \mathbf{t}_2(s)}{|\mathbf{t}_1(s) \wedge \mathbf{t}_2(s)|} \right) \right] \cdot \frac{\partial}{\partial s} \left(\frac{\mathbf{t}_1(s) \wedge \mathbf{t}_2(s)}{|\mathbf{t}_1(s) \wedge \mathbf{t}_2(s)|} \right) \\ &= \frac{1}{2\pi} \oint ds \left[-(\mathbf{t}_1(s) + \mathbf{t}_2(s)) \frac{(1 + \mathbf{t}_1(s) \cdot \mathbf{t}_2(s))}{|\mathbf{t}_1(s) \wedge \mathbf{t}_2(s)|} \right] \cdot \frac{\frac{\partial}{\partial s}(\mathbf{t}_1(s) \wedge \mathbf{t}_2(s))}{|\mathbf{t}_1(s) \wedge \mathbf{t}_2(s)|} \end{aligned}$$

Using $|\mathbf{t}_1 \wedge \mathbf{t}_2|^2 = 1 - (\mathbf{t}_1 \cdot \mathbf{t}_2)^2$ this simplifies to:

$$\text{Wr}_2 - \text{Wr}_1 = \frac{1}{2\pi} \oint ds \frac{(\mathbf{t}_1 \wedge \mathbf{t}_2) \cdot (\dot{\mathbf{t}}_1 + \dot{\mathbf{t}}_2)}{1 + \mathbf{t}_1 \cdot \mathbf{t}_2}. \quad (4.14)$$

The 2nd condition on the homotopy makes sure that this change does not cover the full sphere. In case condition (ii) is not fulfilled, Fuller's equation gives the writhe mod 2. In principle following any non intersecting homotopy one can use Fuller's equation, using continuity to

deal with the anti-parallel points, to calculate the relative writhe. This we will use in the next chapter to calculate the writhe of the plectoneme.

In our setup we do not have a loop but a chain with the end tangents aligned with the force. We first have to close this chain to a loop before using the concepts of writhe and White's relation. Starostin [144] showed that this can be done by closing the loop with a geodesic on the tangent sphere. In our case, with the two end tangents parallel we don't have to care about this closing, since the area the tangents sweep out between both ends is automatically closed. We can define the writhe of the straight chain to be zero and calculate the writhe from equation (4.14) relative to it. This approach presupposes that the chain can not loop around an endpoint. In the magnetic bead experiments we are referring to, this is not possible thanks to the diameter of the bead, $1\text{ }\mu\text{m}$, relative to a deflection length of the order of 10 nm and even to the chain length of 700 nm for part of the experiments.

Plectoneme formation of double-stranded DNA under torsion

5.1 Motivation

We will now extend the WLC model to include the response to torsional stresses in the chain. The helical structure of dsDNA makes the understanding of supercoiling, under torsional stress, important for the mechanics of transcription and replication in both prokaryotes and eukaryotes. Torsion induced supercoiling is also thought to be an important ingredient for the compactification of DNA into the bacterial nucleoid. Also here was it the introduction of single molecule techniques, that made it possible to examine the torsional response of DNA in a precise and controlled way. Making use of the preferred direction for its magnetic moment of super paramagnetic beads [95], allows to measure the relation between torsion and extension while using a force clamp. Also with optical tweezers torsion can be applied while stretching DNA [145], using specially fabricated beads. For larger tensions micropipettes have been used [146]. Since the first magnetic tweezer experiments the precision in measurement has increased to a level that makes it possible to resolve many open questions concerning the elastic properties of DNA. Next to these measurements of the extension as a function of the linking number several methods have been used to measure at the same time the torque [145, 147].

A large amount of models have been devised to describe these experiments, from purely mechanical models [148], mechanical models with electrostatic interactions [149, 150] models that include some entropic effects [151] to phenomenological models [152], each targeted to explain some feature in a specific experiment. Our goal is to make a model built from first principles, valid over a large range of monovalent salt concentrations and loading forces. Our approach differs in several aspects from previous work. First of all we take explicitly the full chain as a continuous elastic rod into consideration. We will show that the writhe of the

chain can be calculated exactly. The electrostatic interaction we take with some precision into account following [153] and argue why this approach is correct.

It is clear that some approximations and simplifications are unavoidable to keep the model simple enough to handle; we will nonetheless capture the essential features that the measurements reveal. In this chapter we introduce the ingredients of the model as an extension of the WLC model from Chapter 3. We will explain the way the plectoneme is formed while being connected to the tails in Section 5.2. In Section 5.4 we will review the various interactions that play a role in the formation of a plectoneme in some detail.

5.2 The mechanistic Plectoneme

Again we describe dsDNA as a persistent chain, for length scales above the helical repeat of 3.5 nm. Since the chain is not torsion free in these experiments, its ends rotationally constrained, we follow the ribbon approach of the previous chapter.

It has to be stressed that we hide the local twist of the double helix in the definition of the ribbon. This twist does show up in a twist stretch coupling, that surprisingly turns out to be negative [154, 151]: twist increases with increasing tension. Its measured value is $-21 k_B T$ [155]. The stretch modulus of dsDNA is rather high, with values in the literature of around 1200 pN [96, 151]. Its direct influence on the extension is small for the forces we are interested in (up to 4 pN). The negative twist stretch coupling has due to this also only a minor influence on the experiments. In this chapter we will not take them into account to avoid clogging the expressions too much. Both we will include when we discuss the influence of thermal fluctuations in Chapter 7.

The energy density of the chain consists of four parts: the bending energy, the twist energy, the potential energies of the externally applied force respectively the torque, and the non-local volume interactions. The Kirchhoff analogy states that this system, without volume interactions, can be mapped to that of a spinning top, whose Hamilton density is the Lagrange density of the elastic ribbon. Since we assume that the chain has an isotropic circular cross-section, the system is mapped to the Lagrange case, which is classically integrable, i.e. a complete set of integrals of motion exists. A comprehensive overview and classification of its solutions can be found in [156].

In the realms of classical elasticity, neglecting thermal fluctuations, applying a torque on a ribbon under tension does at first not change the shape of the centerline up to a critical torque where a buckling bifurcation is reached schematically depicted in Figure 5.1, similar to the buckling transition under compression of an elastic rod as introduced in Chapter 3. At this critical torque loops will form that, constrained by non-local volume interactions, finally will release twist into a plectoneme until the energy gain in releasing twist equals the energy cost of the resulting plectoneme(s) (see Figure 5.2). It is generally assumed that the torque won't change after the nucleation and one speaks of the plectoneme torque as the final torque. The reasoning is that once a plectoneme has formed the increase in linking number all

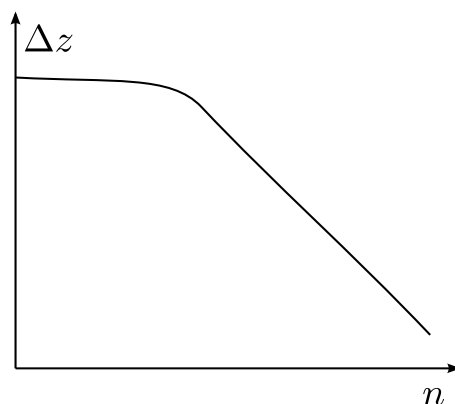


Figure 5.1: Sketch of a typical curve observed when twisting DNA under tension. n is the number of turns, Δz the extension of the molecule.

goes into a regular plectoneme. Since the twist does not change anymore, the torque, being proportional to the twist, should also be constant. This plectoneme torque can be calculated from the turn extension measurements by assuming the torque-linking number relation to be linear before the transition [145]. If indeed the torque does not change once a plectoneme is formed, the torque can be calculated using Maxwell relations between torque/linking number and force/extension [147]. In that last case the linear dependence below the transition is used only once under high tension. Oddly enough there is a discrepancy between the resulting plectoneme torques. This we will resolve in Chapter 7.

The mechanical cost of plectoneme formation caused by the bending of the strands into a helix favors a flat thin plectoneme, with a plectoneme angle $\alpha \simeq \pi/2$. However in this limit the writhe per plectoneme length, as we will soon discuss, is zero and there is no twist release possible. The most efficient twist release happens for $\alpha \simeq \pi/4$. The realized angle will be in between these two limits. The effect of electrostatic interactions is to slightly increase the angle as we will discuss in Section 5.4.3

In general the diameter of the plectoneme tends to be smaller than that of the loop, whose size is largely set by the tension. The optimal diameter of the plectoneme is the result of a competition between

1. efficiency in using contour-length for twist reduction, the cost growing linear with the tension.
2. the resistance against bending, favoring a flat plectoneme.
3. electrostatic repulsion favoring a larger radius and plectoneme angle.
4. thermal fluctuations that drive the strands apart, mostly affecting the radius.

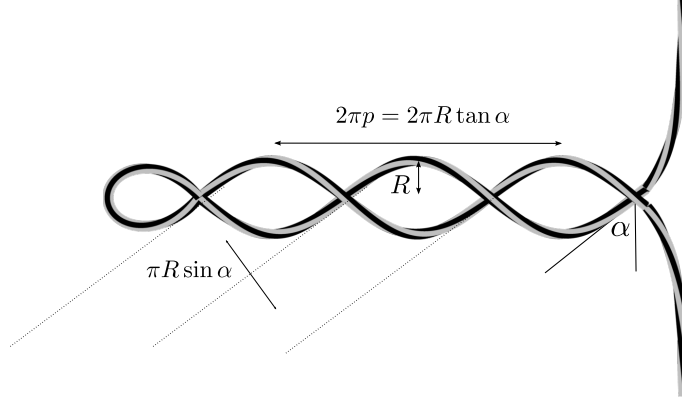


Figure 5.2: The shape of the WLC after buckling. The radius R of the plectoneme is measured from the centerlines of the opposing strands. The dsDNA radius sets a lower limit to this radius.

Increasing the number of turns after the buckling transition increases only the length of the plectoneme, since it is energetically favorable over twist increase. Thermal fluctuations cause the chain to tunnel to a plectoneme before the linking number has reached the bifurcation point. This is not the only thermal effect though. A thorough analysis of thermal fluctuations in the plectoneme turns out to be necessary. In Chapter 7 we will show how to take thermal fluctuations into account after plectoneme nucleation in a proper way under the relevant experimental conditions. This results in a prediction of a new phase in between the classic plectoneme phase and the chaotic chain, where plectoneme formation does not become favorable before the bifurcation point. The theory will be checked against extensive experiments from the Seidel group.

5.3 Linear elasticity

In the experiments using magnetic beads the force is fixed, the gradient of the magnetic field working as a force clamp. The linking number, the “number of turns” is controlled by a rotating magnetic field and the end to end distance of the chain is recorded as a function of these two control parameters. Adding twist and torsion, the reduced energy of the WLC can be written as follows:

$$\mathcal{E} = \int_{-L_c/2}^{L_c/2} ds \left[\frac{P_b}{2} \dot{\mathbf{t}}^2(s) + \frac{P_c}{2} \Delta \psi^2(s) - \mathbf{f} \cdot \mathbf{t}(s) \right] - 2\pi \text{Lk}([\mathbf{t}, \Delta \psi]) \tau_f + \mathcal{E}_{el}([\mathbf{t}]). \quad (5.1)$$

The torque along the force axis, τ_f , is a Lagrange multiplier in case the number of turns is used as a constraint. The linking number is a functional of the local coordinates of the model. The last term, the electrostatic contribution, is responsible for the volume interactions. We split the linking number into a twist and a tangential part using White’s equation (4.7) from

the last chapter. We write:

$$\begin{aligned} \text{Lk}([\mathbf{t}], \Delta\psi) &= \text{Tw}([\Delta\psi]) + \text{Wr}([\mathbf{t}]) \\ &= \frac{1}{2\pi} \int_{-L_c/2}^{L_c/2} ds \Delta\psi(s) + \text{Wr}([\mathbf{t}]). \end{aligned} \quad (5.2)$$

The use of Fuller's local expression is especially handy in the low torque regime, where one could hope that large fluctuations around the ground state, not allowing for writhe homotopy, are energetically suppressed enough to give a negligible contribution to the partition sum, but care has to be taken since the existence of a writhe homotopy can only be checked on a global scale. For a stability analysis, where we only look at infinitesimal fluctuations, it is fine though. We use polar coordinates for the tangent vector with the same choice as in Chapter 3:

$$\mathbf{t}(s) = (\cos \phi \cos \theta, \sin \phi \cos \theta, \sin \theta) \quad \theta \in [-\pi/2, \pi/2], \phi \in [-\pi, \pi] \quad (5.3)$$

The map is again regular around the straight chain state, $\phi = \theta = 0$. The x -axis is chosen in the direction of the force. We now check when the energy functional has negative eigenvalues in its fluctuation determinant. The reference curve is the straight chain aligned along the x -axis. Its writhe we set to zero and it is a solution of the Euler-Lagrange equations. Fuller's equation (4.14) leads to:

$$\begin{aligned} \text{Wr}(\{\phi, \theta\}) &= \frac{1}{2\pi} \int_{-L_c/2}^{L_c/2} ds \frac{(\mathbf{e}_x \wedge \mathbf{t}(s)) \cdot \dot{\mathbf{t}}(s)}{1 + t_x(s)} \\ &= \frac{1}{2\pi} \int_{-L_c/2}^{L_c/2} ds \frac{\sin(\phi(s))\dot{\theta}(s) - \cos(\phi(s))\sin(\theta(s))\cos(\theta(s))\dot{\phi}(s)}{1 + \cos(\phi(s))\cos(\theta(s))} \end{aligned} \quad (5.4)$$

The energy in these coordinates is:

$$\begin{aligned} \mathcal{E} &= \frac{P_b}{2} \int_{-L_c/2}^{L_c/2} ds \left(\cos^2(\theta(s))\dot{\phi}^2(s) + \dot{\theta}^2(s) \right) + \frac{P_c}{2} \int_{-L_c/2}^{L_c/2} ds \Delta\psi^2(s) \\ &\quad - 2\pi\tau_f \left[\text{Wr}(\{\phi, \theta\}) + \frac{1}{2\pi} \int_{-L_c/2}^{L_c/2} ds \Delta\psi(s) \right] \\ &\quad + f[L_c - \int_{-L_c/2}^{L_c/2} ds \cos(\phi(s))\cos(\theta(s))] + \mathcal{E}_{el}(\{\phi, \theta\}) \end{aligned} \quad (5.5)$$

We use OSF [157, 158] theory to account for the electrostatic interactions through a renormalized persistence length and drop the electrostatic term. Fluctuations $d\phi(s), d\theta(s)$ on

top of the straight chain contribute to a change in energy of:

$$\delta \mathcal{E} = \int_{-L_c/2}^{L_c/2} ds \mathbf{X}^T(s) \hat{T} \mathbf{X}(s) \quad (5.6)$$

where we introduced

$$\mathbf{X}(s) = \begin{pmatrix} \delta\phi(s) \\ \delta\theta(s) \end{pmatrix} \quad \hat{T} = \begin{pmatrix} -\frac{P_b}{2} \frac{d^2}{ds^2} + \frac{f}{2} & \frac{\tau_f}{2} \frac{d}{ds} \\ -\frac{\tau_f}{2} \frac{d}{ds} & -\frac{P_b}{2} \frac{d^2}{ds^2} + \frac{f}{2} \end{pmatrix}. \quad (5.7)$$

When $\tau_f \geq \sqrt{2fP_b}$ the determinant of \hat{T} is minimized to a value of $\det \hat{T}$ for Fourier modes with a wavenumber of $k = \sqrt{\frac{\tau_f^2}{2P_b^2} - \frac{f}{P_b}}$. The minimum reached is:

$$\det(\hat{T}) = \frac{\tau_f^2}{4} (fP_b - \frac{\tau_f^2}{4}) \quad (5.8)$$

When the torque (or the corresponding linking number) reaches a value of

$$\tau_{cr} = 2\sqrt{fP_b} \quad \Longleftrightarrow \quad n_{cr} = \frac{\sqrt{fP_b}L_c}{\pi P_c} \quad (5.9)$$

the straight rod solution becomes unstable, as indicated by the sign change of the determinant, marking a transition to a configuration where twist has been traded in for writhe.

For an infinite chain the stable ground state above this *bifurcation point* is a helical shape [159], becoming localized when the boundary effects come into play. In the extreme case of an infinite long chain with tangents at infinity aligned along the direction of force, the solutions correspond to the homoclinic solutions of the equivalent (under the Kirchhoff analogy) symmetric top [156]. We will discuss them and then show that finite size corrections are negligible in the parameter regime we are interested in.

The general solutions of the elastic rod, with twist under a torque low enough that volume interactions do not play a role are characterized by 3 constants of motion in the Kirchhoff analogy. A common choice are the torque along the force direction, τ_f , the torque along the centerline, τ_3 , or equivalently the rate of twist $\Delta\psi$, and the local Lagrange density. The homoclinic solutions are characterized by their asymptotic behavior:

$$\lim_{s \rightarrow \pm\infty} \mathbf{t}(s) = \mathbf{e}_z, \quad (5.10)$$

the main deviation from the straight chain is chosen around $s = 0$. Following [156] we choose the force along the z -axis and standard polar coordinates for the tangent. The Lagrange

density reads:

$$\mathcal{L} = \frac{P_b}{2}(\sin^2(\theta)\dot{\phi}^2(s) + \dot{\theta}^2(s)) + \frac{P_c \Delta\psi^2}{2} + f \cos \theta(s) \quad (5.11)$$

and the homoclinic solutions are given by:

$$\cos(\theta(s, t)) = 1 - 2t^2 \operatorname{sech}^2\left(t \frac{s}{\lambda}\right) \quad (5.12)$$

$$\phi(s, t) = \arctan\left(\frac{t}{\sqrt{1-t^2}} \tanh\left(t \frac{s}{\lambda}\right)\right) + \sqrt{1-t^2} \frac{s}{\lambda}, \quad (5.13)$$

where $\lambda = \sqrt{P_b}/f$ is again the deflection length. For each $t \in [0, 1]$ the above equations define a homoclinic solution. This class of solutions defines at the same time the required homotopy of non crossing curves between the straight line at $t = 0$ and localized solutions up to any value of $t \in [0, 1)$. The electrostatic potential keeps $t < 1$ and so we can use Fuller's equation with the z -axis as reference curve, resulting in a writhe of:

$$\begin{aligned} W_{\text{loop}}(t) &= \frac{1}{2\pi} \int_{-\infty}^{\infty} ds \frac{(\mathbf{e}_z \wedge \mathbf{t}(s)) \cdot \dot{\mathbf{t}}(s)}{1 + t_z(s)} \\ &= \frac{2}{\pi} \arcsin(t). \end{aligned} \quad (5.14)$$

These solutions indeed solve the Euler Lagrange equations, at an appropriately chosen torque, and their Lagrange density is constant along the contour. The energy of the homoclinic solutions has a potential contribution and equal elastic contribution that add to

$$\mathfrak{E}_{\text{loop}}(t) = 2 f L_{\text{loop}} \quad L_{\text{loop}} = \int_{-\infty}^{\infty} ds [1 - \cos(\theta(s, t))] = 4\lambda t. \quad (5.15)$$

with L_{loop} the change in extension compared to the straight chain, which we will use as the length of the loop part of the solution. This results in an energy of the homoclinic solution with given linking number Lk :

$$\mathcal{E}(t) = \mathfrak{E}_{\text{loop}}(t) + \frac{(2\pi)^2 P_c}{2 L_c} \left[Lk - \frac{2}{\pi} \arcsin(t) \right]^2. \quad (5.16)$$

From this expression follows that for tensions $f < f_0 := 4 P_c^2 / (P_b L_c^2)$ the energy minimum shifts from the straight rod continuously to the homoclinic loop when increasing the linking number from Lk_{cr} (5.9) till 1. For tensions above f_0 only a limited range of stable solutions in between the two extremes exists. Also in that case the straight rod ceases to be stable at

Lk_{cr} , while the barrier to the loop solution disappears a little later, when:

$$Lk = Lk_{cr} \sqrt{1 - \frac{4}{Lk_{cr}^2 \pi^2}} + \frac{2}{\pi} \arcsin \left(\frac{2}{Lk_{cr} \pi} \right) \quad (5.17)$$

In Figure 5.3 a typical situation is sketched for a chain of 600 nm and a tensile force of 2 pN $\gg f_0$. Note how already in an early stage a local minimum starts to form separated by a barrier from the straight rod that shifts to smaller t values with increasing Lk .

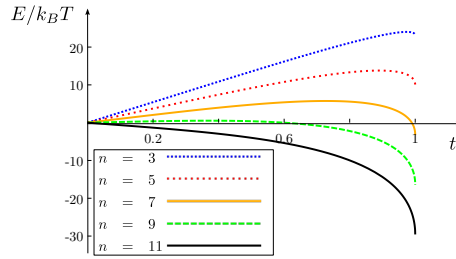


Figure 5.3: Relative energies of homoclinic solutions as a function of the homoclinic parameter t for several linking numbers, n . The energy is relative to the straight rod where all of the linking number is in the twist of the chain.

The excluded volume interactions, caused by short distance electrostatics, stabilize the final loop. At the moment this electrostatics dictated loop configuration has been reached, more twist will be released through plectonemic extension of the loop, discussed in the next section.

The two legs of the homoclinic solutions have a non trivial point of closest approach whenever $t > t_c \simeq 0.80424$. Its value is found from the nontrivial minimum of

$$d(s, t) = 2\lambda \sqrt{4t^2 \operatorname{sech}^2(st/\lambda) \sin^2(s\sqrt{1-t^2}/\lambda) + (s/\lambda - 2t \tanh(st/\lambda))^2}. \quad (5.18)$$

For a given force this distance has a maximum of $d_m \simeq 1.4\lambda$, for the critical homoclinic parameter t_c . This maximum has an important influence on the possibility of plectoneme formation, limiting the strength of electrostatics or the weakness of screening allowed, since as a condition for plectoneme nucleation one expects a point of closest approach, functioning as a pivot.

To separate the local OSF type effect of chain stiffening from the nonlocal loop destabilizing electrostatics the loop size should be larger than the Debye screening length [160]. It is possible to extend this approach over a larger range [161]. We have reasons not to do this:

1. The experimental conditions are such that the loopsize is considerably larger than the screening length. This is not accidental, since at the moment that they are almost equal a simple scaling argument would reveal that the energy cost per gained writhe in the

plectoneme is in that case of the same magnitude as that of the loop. Combining this with the entropic gain in forming more loops, plectoneme nucleation is unlikely.

2. The details of the groundstate energetics of the endloop are not relevant for plectoneme formation even close to the transition point, when thermal fluctuations are taken into account.
3. It would complicate the calculations considerably without a benefit relevant to the measurements.

We will finally discuss finite size effects on the ground state solution space. By comparing the exact one loop solution for a finite chain with the homoclinic loop solution it is straightforward to show that the energy increase, to lowest order, is given by:

$$\Delta \mathcal{E}_{\text{finite}}(y) = 64 f L_c \exp(-2 L_c / \lambda) \quad (5.19)$$

Since in the experiments considered $L_c \gg \lambda$, this exponential decaying factor is negligible, until most of the chain sits in a plectoneme.

5.4 The Plectoneme

5.4.1 Geometry

After the formation of the homoclinic loop generically, depending on the salt concentration, a plectoneme will form, since as we will see the growing of a plectoneme is energetically cheaper than the formation of another homoclinic loop, to change twist into writhe.

The simplest model for electrostatic interactions would start from the repulsion of 2 parallel rods. As can be seen from Figure 5.2 it wouldn't do justice to the geometry of the plectoneme as was thoroughly discussed by Ubbink and Odijk [153]. The reason is that seen from one point along the chain, the electrostatic repulsion by the opposing strand has a radial component, increasing the plectoneme radius, and a pitch component, increasing the plectoneme angle, that are not equivalent.

We will for simplicity take the plectoneme radius and angle to be constant along the plectoneme, but take the homoclinic limit solution to be set by the demand that the nontrivial shortest distance between the two legs of the homoclinic solution, is equal to twice the plectoneme radius. It is here that we will define the start of the plectoneme, ending in the remaining part of the homoclinic solution, that remains connected rotating around the plectoneme with the growing plectoneme. In this way our solution is continuous. One could argue that the assumption of constant plectoneme parameters does not represent the true minimum of the free energy and that in reality the space curve should be smooth. However details of the energetics are not important for the experiments, where most contributions come from the plectoneme alone.

We will use the following space curve parameterized by the contour length s to describe a plectoneme starting at $s = 0$:

$$\begin{aligned}
 s \in [0, L_p/2] : \quad & s \in [L_p/2 + L_{\text{loop}}, L_p + L_{\text{loop}}] : \\
 \mathbf{r}_p(s) = \begin{pmatrix} (s_0 + s) \sin \alpha \\ -R \cos \left((s_0 + s) \frac{\cos \alpha}{R} \right) \\ R \sin \left((s_0 + s) \frac{\cos \alpha}{R} \right) \end{pmatrix} & \mathbf{r}_p(s) = \begin{pmatrix} (s_0 + L_p + L_{\text{loop}} - s) \sin \alpha \\ R \cos \left((s_0 + L_p + L_{\text{loop}} - s) \frac{\cos \alpha}{R} \right) \\ -R \sin \left((s_0 + L_p + L_{\text{loop}} - s) \frac{\cos \alpha}{R} \right) \end{pmatrix},
 \end{aligned} \tag{5.20}$$

with R and α the plectoneme radius and angle, L_p the contour length of DNA in the plectoneme and L_{loop} the contour length of the end loop. The starting orientation depends on the homoclinic solution and is set by s_0 . The local unit tangent is $\mathbf{t}(s) = \dot{\mathbf{r}}(s)$. To simplify the calculations, we mention that the relation of the radius to the homoclinic parameter, as follows from equation (5.18), can be approximated in the relevant range $t \in [0.80424, 1)$ to ample accuracy by:

$$t = 1 - 0.3799 \left(\frac{R}{\lambda} + 0.0112 \right)^2 \tag{5.21}$$

One often assumes the plectoneme to have a constant writhe per contourlength of

$$\omega = \frac{\sin(2\alpha)}{4\pi R} \tag{5.22}$$

although it is usually considered to be right within some approximation [153, 162] neglecting endloop and tails. In appendix (B) we show this expression to be exact when we include the change of writhe of the endloop while increasing the plectoneme length.

5.4.2 Elasticity

The free energy density (the free energy per length of strand) of the plectoneme has three distinct contributions: an elastic contribution due to the curved path of the centerline of DNA, an electrostatic repulsion of the two strands and a potential part due to the work done against the stretching force, which is just $f L_p$. Since the curvature of a strand in the plectoneme is constant, the reduced elastic energy density is given by

$$\epsilon_{\text{bend}}(t, \alpha) = \frac{P_b \cos^4(\alpha)}{2 R(t)^2} \tag{5.23}$$

5.4.3 Electrostatics

Since DNA is a strong electrolyte, in a neutral pH environment, the persistence length gets an electrostatic correction. Using OSF theory [157, 158] and taking counterion condensation [163] into account by reducing the charge density along the chain to the charge density left after condensation [160], the resulting renormalized persistence length becomes:

$$P_b = P_{b(0)} + \frac{1}{4\kappa^2 Q_B} \quad (5.24)$$

with κ^{-1} the Debye screening length: and Q_B the Bjerrum length [164]:

$$\kappa = \sqrt{\frac{2q_e^2 n_s}{\epsilon_r \epsilon_0 k_B T}} \quad Q_B = \frac{q^2}{4\pi \epsilon_r \epsilon_0 k_B T} \quad (5.25)$$

with ϵ_0 the electric constant, ϵ_r the dielectric constant of water, q_e the elementary charge and n_s the number density of salt molecules. For water at room temperature, 298 K, the Bjerrum length is 0.715 nm. Expressing the concentration of salt, c_s in mM(milli molar) or mol/ m³ the inverse screening length at room temperature is $\kappa = 0.1\sqrt{c_s}$. The reduced energy density of the electrostatic interaction is described by the Ubbink-Odijk theory [153]:

$$\epsilon_{el}^0(t, \alpha) = \frac{q_{eff}^2 Q_B}{2} \sqrt{\frac{\pi}{\kappa R(t)}} e^{-2\kappa R(t)} Z(\cot(\alpha)) \quad (5.26)$$

$$Z(x) = 1 + m_1 x^2 + m_2 x^4 \quad m_1 = 0.828, m_2 = 0.864 \quad (5.27)$$

valid for $\cot(\alpha) < 1$, with q_{eff} the effective charge density of the centerline of a cylinder that is the source of a Debye-Hückel potential that coincides asymptotically in the small potential, far field with the nonlinear Poisson-Boltzmann potential of that cylinder with a given surface charge. For dsDNA we take a naked charge density of 2 charges per 0.34 nm, representing the 2 phosphate charges per basepair, and a radius of 1 nm.

The expansion is a fit that behaves reasonably also for $\cot \alpha$ close to one, where a standard asymptotic expansion would fail.

To calculate the effective charge density we follow the method laid out by Philip and Wooding [165]. It is fast and accurate for our conditions, plus it automatically gives the radius R^* , where the reduced potential equals 1 and thus the linearized theory breaks down. In Figure 5.4 and Figure 5.5 the dependence of the effective charge density and the non-linear radius R^* on the salt concentration are plotted for DNA. Note that the effective charge *increases* almost linearly with increasing salt concentration. This increase is a compensation for pushing back the charge to the centerline under stronger screening.

To understand the limitations it is good to recapitulate the limits of validity for the mean force calculations [166, 167] that form the basis of the treatment by Ubbink et al. First of all a mean field treatment with point like particles, that is Poisson-Boltzmann, needs to

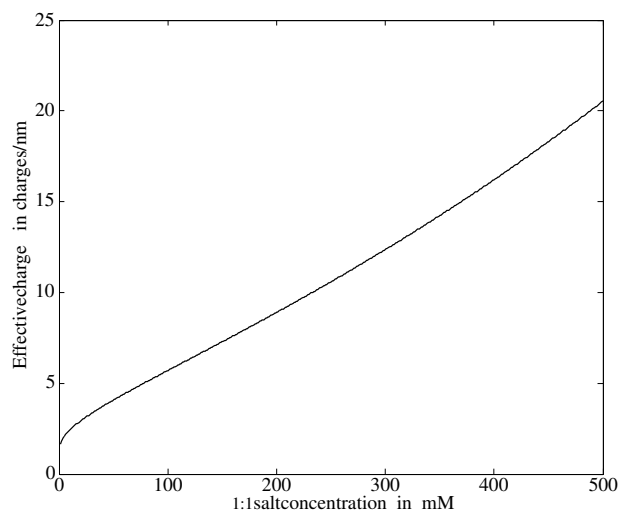


Figure 5.4: The effective charge line density as function of salt concentration

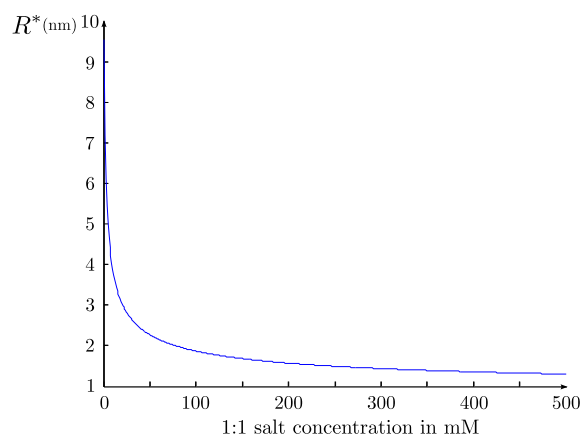


Figure 5.5: The radius where the electrostatic and thermal energy are equal as function of salt concentration

be applicable. That requirement is fulfilled since we are only looking at monovalent salt solutions¹. The distance should be so large that within the nonlinear region around one cylinder, the potential of the other cylinder is negligible and, which in our case is practically equivalent, the potential halfway in between the two cylinders is small enough that linear superposition holds. We will see that under experimental conditions this requirement is fulfilled.

5.4.4 Summing up

We have now an expression for the energy of a configuration with plectoneme under fixed linking number but still without thermal fluctuations:

$$\mathcal{E}(t, \alpha) = -f(L_c - L_p) + \mathfrak{E}_{\text{loop}}(t) + L_p(\epsilon_{\text{bend}}(t, \alpha) + \epsilon_{\text{el}}^0(t, \alpha)) + \frac{(2\pi)^2 P_c}{2L_c} (Lk - W_{\text{rloop}}(t) - L_p \omega(t, \alpha))^2 \quad (5.28)$$

For a plectoneme to form, a balance is needed between maximizing ω and minimizing the elastic, electrostatic, and potential free energy densities. The optimal plectoneme angle will settle between $\pi/4$, maximizing the writhe density, and $\pi/2$ minimizing bending energy. This is confirmed by explicit minimizations in Chapter 8. A condition for a local minimum to exist is that equation (5.28) has a minimum with respect to variations in L_p for finite positive L_p :

$$L_p(t, \alpha) = \frac{Lk - W_{\text{rloop}}(t)}{\omega(t, \alpha)} - \frac{L_c}{(2\pi)^2 \omega^2(t, \alpha) P_c} (\epsilon_{\text{bend}}(t, \alpha) + \epsilon_{\text{el}}^0(t, \alpha) + f) > 0. \quad (5.29)$$

The plectoneme is a global minimum when the resulting energy is lower than the straight chain solution. This second condition happens in general at larger Lk and so the transition is from a straight solution to a plectoneme with finite length. This *transition point*, when the global free energy minimum changes from the rod like solution to a plectoneme, is under usual experimental conditions considerably below the bifurcation point. The energy barrier between the two minima is of the order of $f\lambda \sim 10k_B T$, for lengths ($\sim 700 - 4000\text{nm}$) and forces ($\sim 1 - 4\text{pN}$) as used in the experiments. This results in a seemingly first order transition even at finite temperatures, rendering the behavior essentially different from the Euler buckling of semiflexible polymers, where thermal fluctuations destroy long range ordering as discussed in Chapter 3 without the addition of frictional forces [169].

¹See for a recent assessment [168])

Chapter 6

Free energy of a confined worm like chain under torsion

In this chapter we lay the foundation for the extension of the mechanistic plectoneme model with thermal fluctuations, that will be the main subject of the next chapter. The plectonemes that form put the chains into a confined environment that has an important impact on the way the torsional loads get divided. We will extend the WLC model from earlier chapters to one with a finite stretch modulus and twist stretch coupling, confined in a channel with dimensions far below the persistence length of the chain, even compared to a torsion corrected persistence length. The narrowness of the channel implicates that the chain does not fold on itself, but that it is up to fluctuations stretched, the so called Odijk regime [170]. In the torsion free case an analogous calculation was performed by Burkhardt [171], but his calculation can not immediately be applied to this more complex problem. To start of we will redo the calculations of Moroz and Nelson [172] of a chain under torsion and tension below buckling. We will take a different approach, as a guideline for how to treat the more complicated cases. An analogous calculation in less detail was also done by Marko [173]

6.1 Chain under tension

The WLC Hamiltonian is easily extended to include an elastic stretch term and a twist stretch coupling. The stretch modulus, multiplying a term quadratic in the stretch, is not precisely known, but values are in the 700 pN to 1400 pN range. It is pretty large which is one of the reasons stretch is often neglected. The twist stretch coupling modulus, B , multiplies a term linear in twist and stretch, thereby breaking stretch-compress and chiral symmetries. It was recently found to be negative: when stretch increases, twist also increases. More about these quantities for DNA in the next chapter. The chain is now not only represented by its tangent and differential twist angle, but also by a local stretch scalar. The parametrization is as before, but it is to be noted that the parametrization does not anymore coincide with the contour

length due to the stretch. The Hamiltonian reads, up to quadratic order:

$$\mathcal{H} = \int_0^{L_c} ds \left[\frac{P_b}{2} \left(\frac{d\mathbf{t}(s)}{ds} \right)^2 + \frac{P_c}{2} \dot{\psi}^2(s) + \frac{S}{2} u(s)^2 + B \dot{\psi}(s) u(s) - f \left(1 + u(s) - \frac{\mathbf{t}_\perp^2(s)}{2} \right) \right] \quad (6.1)$$

We look at fluctuations around the ground-state. The Euler Lagrange equations for the twist angle, $\dot{\psi}$, and stretch factor $u(s)$ give the obvious “classical” results:

$$\dot{\psi}_0 = \text{constant} \quad u_0 = \frac{f - B \dot{\psi}_0}{S} \quad (6.2)$$

When changing to a fixed linking number ensemble we will make the natural choice $\dot{\psi}_0 = 2\pi \langle \text{tw} \rangle$, the expectation value of the twist density. Completing the square for $u(s)$, and assuming the fluctuations around the ground-state stretch factor to be small, they can be integrated out:

$$\mathcal{H} = \int_0^{L_c} ds \left[\frac{P_b}{2} \left(\frac{d\mathbf{t}_\perp(s)}{ds} \right)^2 + \frac{P_c}{2} \dot{\psi}^2(s) - \frac{(f - B \dot{\psi}(s))^2}{2S} - f \left(1 - \frac{\mathbf{t}_\perp^2(s)}{2} \right) \right] \quad (6.3)$$

As we have local expressions for twist, $\text{tw}(s) = \frac{\dot{\psi}(s)}{2\pi}$, and writhe ω , given by Fuller’s equation, equation (4.14) up to quadratic order:

$$\omega(s) \simeq \frac{1}{4\pi} \left(t_x(s) \frac{dt_y(s)}{ds} - \frac{dt_x(s)}{ds} t_y(s) \right), \quad (6.4)$$

we can define a linking density as $\text{lk}(s) := \text{tw}(s) + \omega(s)$. The boundary conditions we want to study are with $Lk = \int ds \text{lk}$ fixed. Writing $\text{lk}(s) = \text{lk} + \delta(s)$, with $\text{lk} = Lk / L_c$, allows us to integrate over the fluctuations:

$$\begin{aligned} \mathcal{H} &= \int_0^{L_c} ds \left[\frac{P_b}{2} \left(\frac{d\mathbf{t}_\perp(s)}{ds} \right)^2 + 2\pi^2 P_c (\text{lk} - \omega(s))^2 - \frac{(f - 2\pi B (\text{lk} - \omega(s)))^2}{2S} \right. \\ &\quad \left. - f \left(1 - \frac{\mathbf{t}_\perp^2(s)}{2} \right) \right] \\ &= \int_0^{L_c} ds \left[\frac{P_b}{2} \left(\frac{d\mathbf{t}_\perp}{ds} \right)^2 + \frac{f}{2} \mathbf{t}_\perp^2 - \left(\pi P_c' \text{lk} + \frac{Bf}{2S} \right) (t_x \dot{t}_y - \dot{t}_x t_y) \right] \\ &\quad + \left(2\pi^2 P_c \text{lk}^2 - \frac{(f - 2\pi B \text{lk})^2}{2S} - f \right) L_c \end{aligned} \quad (6.5)$$

with $P_c' := P_c - B^2 / S$, the effective torsional persistence length renormalized by the twist stretch coupling, as introduced by Marko [173]. We rescale lengths with the deflection length, $\hat{s} = s/\lambda$:

$$\mathcal{H} = \int_0^{\hat{L}_c} d\hat{s} \left[\frac{\alpha}{2} \left(\frac{d\mathbf{t}_\perp(\hat{s})}{d\hat{s}} \right)^2 + \frac{\alpha}{2} \mathbf{t}_\perp^2(\hat{s}) - \frac{\gamma}{2} (t_x i_y - i_x t_y) \right] + \left(2\pi^2 P_c \text{lk}^2 - \frac{(f - B 2\pi \text{lk})^2}{2S} - f \right) L_c$$

with $\alpha = \sqrt{P_b f}$, $\hat{L}_c = L_c / \lambda$, and $\gamma = 2(\pi P_c' \text{lk} + \frac{Bf}{2S})$ dimensionless. We take periodic boundary conditions changing to Fourier series

$$\mathbf{t}(\hat{s}) = \sum_{n=-\infty}^{\infty} \mathbf{a}_n \exp\left(i \frac{2\pi n}{\hat{L}_c} \hat{s}\right) \quad (6.6)$$

resulting in

$$\mathcal{H} = \sum_{n=1}^{\infty} \left(\mathbf{a}_n^\dagger \hat{T}_n \mathbf{a}_n \right) + \left(2\pi^2 P_c \text{lk}^2 - \frac{(f - B 2\pi \text{lk})^2}{2S} - f \right) L_c \quad (6.7)$$

with

$$\hat{T}_n = \begin{pmatrix} \alpha \left(\frac{2\pi n}{\hat{L}_c} \right)^2 + \alpha & -i\gamma \frac{2\pi n}{\hat{L}_c} \\ i\gamma \frac{2\pi n}{\hat{L}_c} & \alpha \left(\frac{2\pi n}{\hat{L}_c} \right)^2 + \alpha \end{pmatrix} \quad (6.8)$$

The eigenvalues are

$$\mu_{n,\pm} = \alpha \left(\frac{2\pi n}{\hat{L}_c} \right)^2 + \alpha \pm \gamma \frac{2\pi n}{\hat{L}_c} \quad (6.9)$$

The partition sum is a product of Gaussian integrals and so

$$Z = \mathcal{N} \exp \left[- \left(2\pi^2 P_c \text{lk}^2 - \frac{(f - B 2\pi \text{lk})^2}{2S} - f \right) L_c \right] \prod_{n=1}^{\infty} \frac{\alpha^2 \left(\frac{2\pi n}{\hat{L}_c} \right)^4}{\mu_{n,+} \mu_{n,-}} \quad (6.10)$$

In the denominator of the product we have a quadratic expression in n^2 . Let η_i , ($i = 1, 2$) be its roots. Then we can write the product as:

$$\begin{aligned} \prod_{n=1}^{\infty} (\dots) &= \prod_{i=1}^2 \prod_{n=1}^{\infty} \frac{1}{(1 - \frac{\eta_i}{n^2})} \\ &= \prod_{i=1}^2 \frac{\pi \sqrt{\eta_i}}{\sin(\pi \sqrt{\eta_i})} \end{aligned} \quad (6.11)$$

The complex part of the square root of these roots gives the exponential decay with increasing chain length. The roots are:

$$\eta_{1,2} = \left(\frac{\hat{L}_c}{2\pi} \right)^2 \left(\frac{\gamma^2}{2\alpha^2} - 1 \pm i \frac{\gamma}{\alpha^2} \sqrt{\alpha^2 - \frac{\gamma^2}{4}} \right) \quad (6.12)$$

Alternatively we can work all the time in the continuum limit, which will turn out to be useful for the confined case coming up soon:

$$\begin{aligned} \mathcal{F} &= \left(2\pi^2 P_c l k^2 - \frac{(f - B 2\pi l k)^2}{2S} - f \right) L_c + \hat{L}_c \int_0^{\infty} \frac{dp}{2\pi} \log \left(\frac{(p^2 + 1)^2 - \frac{\gamma^2}{\alpha^2} p^2}{p^4} \right) \\ &= \left(2\pi^2 P_c l k^2 - \frac{(f - B 2\pi l k)^2}{2S} - f + \frac{\sqrt{\alpha^2 - \gamma^2/4}}{\alpha \lambda} \right) L_c \\ &= \left(2\pi^2 P_c l k^2 - \frac{(f - B 2\pi l k)^2}{2S} - f + \frac{1}{P_b} \sqrt{f P_b - \frac{1}{4} (2\pi P_c' l k + B f / (S) - \sigma / (2\pi))^2} \right) L_c \end{aligned} \quad (6.13)$$

To calculate the writhe density expectation value we have added a term $\sigma \omega$ to the Hamiltonian and we find

$$\begin{aligned} \langle \omega \rangle &= \frac{1}{L_c} \frac{\partial \beta \mathcal{F}}{\partial \sigma} \Big|_{\sigma=0} = \frac{1}{2\pi P_b} \frac{\frac{1}{4} (2\pi P_c' l k + \frac{B f}{S})}{\sqrt{f P_b - \frac{(2\pi P_c' l k + \frac{B f}{S})^2}{4}}} \Rightarrow \\ \langle tw \rangle &= l k \left(1 - \frac{1}{2\pi P_b} \frac{\frac{1}{4} (2\pi P_c' l k + \frac{B f}{S l k})}{\sqrt{f P_b - \frac{(2\pi P_c' l k + \frac{B f}{S})^2}{4}}} \right) \end{aligned} \quad (6.14)$$

The stretch factor u_0 follows from equation (6.2): $u_0 = (f - B 2\pi \langle tw \rangle) / S$. We obtain the relative extension of the chain by differentiating the free energy with respect to the force:

$$\begin{aligned} \rho &:= \frac{\langle \Delta z \rangle}{L_c} = -\frac{1}{L_c} \frac{\partial \mathcal{F}}{\partial f} \\ &= 1 - \frac{P_b - \frac{B}{2S} (2 \text{lk} \pi P_c' + \frac{Bf}{S})}{2 P_b \sqrt{f P_b - \frac{(2 \text{lk} \pi P_c' + \frac{Bf}{S})^2}{4}}} + \frac{f - 2 B \text{lk} \pi}{S} \end{aligned} \quad (6.15)$$

Finally it is interesting to know the expectation value of the torque that the end of the chain exerts on the 2 clamps that set the linking number. To calculate it, we add a term $-\tau 2\pi \text{lk}$ to the free energy and minimize with respect to lk . This gives the torque at a point along the chain:

$$\langle \tau \rangle = 2 \text{lk} P_c' \pi + \frac{B(f - 2 B \text{lk} \pi)}{S} - \frac{P_c' (\text{lk} P_c' \pi + \frac{Bf}{2S})}{2 P_b \sqrt{f P_b - (\text{lk} P_c' \pi + \frac{Bf}{2S})^2}} \quad (6.16)$$

6.2 Confined chain: isotropic case

We consider a linking number constrained chain of contour-length L_0 , confined along the z -axis in a harmonic potential. Following Burkardt [171] we will assume the potential to be strong enough so that there are no overhangs. The Hamiltonian reads:

$$\mathcal{H} = \int_0^{L_c} ds \left[\frac{P_b}{2} \left(\frac{d^2 \mathbf{r}(s)}{ds^2} \right)^2 + \frac{P_c}{2} \dot{\psi}^2(s) + \frac{S}{2} u(s)^2 + B \dot{\psi}(s) u(s) + \frac{b}{2} (r_x^2(s) + r_y^2(s)) \right], \quad (6.17)$$

where s is the stretched chain contour, $s(t) = \int_0^t dt' (1 + u(t'))$ and L_c the contour length of the stretched chain. We furthermore changed to coordinates perpendicular to the channel axis, neglecting all terms above quadratic ones in either \mathbf{r} or its derivative.

Note that, unlike u , $\dot{\psi}$ is not in general a small variable, since we consider a chain under torsion. White's relation must hold, taking the ends parallel to the confinement axis. The absence of overhangs means that all fluctuating paths are writhe homotopic¹ to the confinement axis, so we can use Fuller's equation (4.14) and we can write $\text{Wr} = \int_0^{L_c} ds \omega(s)$.

¹This is actually not true since the paths in a path integral are not smooth to the extreme, but in a limit sense it can be used

Using the confinement axis as reference curve we have up to quadratic order:

$$\omega(s) \simeq \frac{1}{4\pi} \left(\frac{dr_x(s)}{ds} \frac{d^2 r_y(s)}{ds^2} - \frac{d^2 r_x(s)}{ds^2} \frac{dr_y(s)}{ds} \right) \quad (6.18)$$

We make the following coordinate change:

$$\phi(s) := \psi(s) - 2\pi \text{lk} + 2\pi \omega(s) \text{ with linking number density: } \text{lk} := \frac{Lk}{L_c} \quad (6.19)$$

with obviously $\int_0^{L_c} ds \phi(s) = 0$. After completing the square for $u(s)$ we find up to quadratic order:

$$\mathcal{H} = \int_0^{L_c} ds \left[\frac{P_b}{2} \left(\frac{d^2 \mathbf{r}(s)}{ds^2} \right)^2 + \frac{b}{2} \mathbf{r}^2(s) - \pi P_c' \text{lk} (\dot{r}_x \ddot{r}_y - \ddot{r}_x \dot{r}_y) \right] + 2\pi^2 P_c' \text{lk}^2 L_c \quad (6.20)$$

To simplify the calculations we rescale the internal (contour) length and the external (channel width) length following Burkhardt:

$$\hat{s} = b^{1/4} P_b^{-1/4} s \quad \hat{\mathbf{r}} = P_b^{1/8} b^{3/8} \mathbf{r} \quad \hat{P} = \frac{P_c'}{P_b} \quad \hat{\text{lk}} = b^{-1/4} P_b^{1/4} \text{lk} \quad \alpha := b^{1/4} P_b^{3/4} \quad (6.21)$$

resulting in:

$$\mathcal{H} = \int_0^{\hat{L}_c} d\hat{s} \left[\frac{1}{2} \left(\frac{d^2 \hat{\mathbf{r}}(\hat{s})}{d\hat{s}^2} \right)^2 + \frac{1}{2} \hat{\mathbf{r}}^2(\hat{s}) - \pi \hat{P} \hat{\text{lk}} (\dot{\hat{r}}_x \ddot{\hat{r}}_y - \ddot{\hat{r}}_x \dot{\hat{r}}_y) \right] + 2\alpha\pi^2 \hat{P} \hat{\text{lk}}^2 \hat{L}_c \quad (6.22)$$

We go now to momentum space, taking periodic boundary conditions:

$$\mathcal{H} = \sum_{n=1}^{\infty} \left(\mathbf{a}_n^\dagger \hat{\mathbf{T}}_n \mathbf{a}_n \right) + \hat{L}_c 2\alpha\pi^2 \hat{P} \hat{\text{lk}}^2 \quad (6.23)$$

with

$$\hat{\mathbf{T}}_n = \begin{pmatrix} \left(\frac{2\pi n}{\hat{L}_c} \right)^4 + 1 & i 2\pi \hat{P} \hat{\text{lk}} \left(\frac{2\pi n}{\hat{L}_c} \right)^3 \\ -i 2\pi \hat{P} \hat{\text{lk}} \left(\frac{2\pi n}{\hat{L}_c} \right)^3 & \left(\frac{2\pi n}{\hat{L}_c} \right)^4 + 1 \end{pmatrix} \quad (6.24)$$

The eigenvalues are

$$\lambda_{n,\pm} = \left(\frac{2\pi n}{\hat{L}_c} \right)^4 + 1 \pm 2\pi \hat{P} \hat{l} k \left(\frac{2\pi n}{\hat{L}_c} \right)^3 =: \left(\frac{2\pi n}{\hat{L}_c} \right)^4 + 1 \pm \zeta \left(\frac{2\pi n}{\hat{L}_c} \right)^3 \quad (6.25)$$

There is an instability for

$$\zeta_{cr} = \frac{4}{3^{3/4}} \Rightarrow l k_{cr} = \frac{2b^{1/4} P_b^{3/4}}{3^{3/4} \pi P_c'} \quad (6.26)$$

The partition sum is a product of Gaussian integrals

$$Z = \mathcal{N} \exp(-2\alpha\pi^2 \hat{P} \hat{l} k^2 \hat{L}_c) \prod_{n=1}^{\infty} \frac{\left(\frac{2\pi n}{\hat{L}_c} \right)^8}{\lambda_{n,+} \lambda_{n,-}} \quad (6.27)$$

In the denominator of the product we have a quartic expression in n^2 . Let $\eta_i \bar{\eta}_i$, $(i = 1, 2)$ be the pairs of conjugate roots then we can write the product as:

$$\begin{aligned} \prod_{n=1}^{\infty} (\dots) &= \prod_{i=1,2} \prod_{n=1}^{\infty} \frac{1}{\left(1 - \frac{\eta_i}{n^2}\right)} \frac{1}{\left(1 - \frac{\bar{\eta}_i}{n^2}\right)} \\ &= \prod_{i=1,2} \frac{\pi \sqrt{\eta_i}}{\sin(\pi \sqrt{\eta_i})} \frac{\pi \sqrt{\bar{\eta}_i}}{\sin(\pi \sqrt{\bar{\eta}_i})} \end{aligned} \quad (6.28)$$

The complex part of the square root of these roots give the exponential decay with increasing chain length. The roots are all of the form:

$$\eta_i = \left(\frac{\hat{L}}{2\pi} \right)^2 \xi_i(\zeta) \quad \text{and complex conjugate} \quad (6.29)$$

The functions ξ_i , choosing the branch cut appropriately, are found to be:

$$\xi_j(\zeta) = \frac{\zeta^2}{4} + \frac{(-1)^j}{4} \sqrt{g(\zeta)} + \frac{i}{2} \sqrt{4 - \frac{3}{4}\zeta^4 + \frac{g(\zeta)}{4}} + (-1)^j \frac{8\zeta^2 - \zeta^6}{4\sqrt{g(\zeta)}} \quad (6.30)$$

with

$$g(\zeta) := \zeta^4 - \frac{16}{3} + \frac{128}{9h(\zeta)} + 2h(\zeta) \quad h(\zeta) := \left[4\zeta^4 - 2\zeta_{cr}^4 + 4\zeta^2 \sqrt{\zeta^4 - \zeta_{cr}^4} \right]^{1/3} \quad (6.31)$$

Now write $\sqrt{\xi_{1,2}} = (x_{1,2} \pm iy_{1,2})$. In the long chain limit the contribution of the roots to the partition sum is:

$$\frac{\frac{\hat{L}_c^2}{4} |\xi|}{\sin^2(\hat{L}_c x/2) \cosh^2(\hat{L}_c y/2) + \cos^2(\hat{L}_c x/2) \sinh^2(\hat{L}_c y/2)} \simeq \hat{L}_c^2 |\xi| e^{-\hat{L}_c |y|} \quad (6.32)$$

Let $\xi_{1,2}$ be representatives of the two conjugate pairs and $y_{1,2}$ its imaginary parts. The partition sum is given by:

$$Z \simeq \mathcal{N} \exp(-2\alpha\pi^2 \hat{P} \hat{l} k^2 \hat{L}_c) \hat{L}_c^4 |\xi_1 \xi_2| e^{-\hat{L}_c (|y_1| + |y_2|)} \quad (6.33)$$

The free energy of the confined chain per contour-length in the long chain limit is given by the lowest eigenvalue of the Hamiltonian :

$$f = - \lim_{L_c \rightarrow \infty} \frac{1}{L_c} \log(Z) = 2\pi^2 P_c' l k^2 + \left(\frac{b}{P_b} \right)^{1/4} (|y_1| + |y_2|) \quad (6.34)$$

The first term is the twist energy stored in the chain, the second represents the free energy

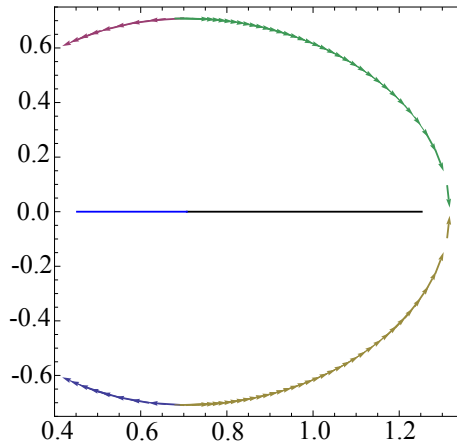


Figure 6.1: Flow of the roots $\sqrt{\xi_i}$ in the complex plane under increasing torsion. The horizontal line indicates the speed with which the roots flow as explained in the text.

of the confinement. In case the linking number density is zero, the roots are, up to a sign equal: $\xi_{1,2} = \pm i \Rightarrow |y_{1,2}| = 1/\sqrt{2}$ and we retrieve Burkhardt's result. The flow of the roots under increasing linking number density is depicted in Figure 6.1. Starting from $lk = 0$ the root pairs move apart. Both decrease their imaginary parts, effectively decreasing the free energy of confinement. The reason is that the thermal writhe pushes the chains away from the centerline. This does not happen in a symmetric way, as is shown by the line along the x -axis, where each arrow corresponds to a fixed increase of lk . At lk_{cr} the right pair of roots

becomes real indicating a singularity in the partition sum. Of course our theory breaks down before this happens. To facilitate a fast calculation of the effect of twist on the confinement free energy the following expression can be shown to give an approximation with a maximum error less than 0.7%.:

$$|y_1| + |y_2| \simeq \sqrt{2} \left[\left(\frac{3^{3/4} - 1}{2\sqrt{3^{3/4}}} + \frac{\zeta}{10} \right) \sqrt{\frac{4}{3^{3/4}} - \zeta} + \frac{1}{3^{3/4}} \right] \quad (6.35)$$

Another way to calculate the free energy is the following, starting from (6.27), omitting a constant and the twist part

$$\begin{aligned} \mathfrak{f} &= \frac{1}{L_c} \sum_{n=1}^{\infty} \log \left(\frac{(p_n^4 + 1)^2 - \zeta^2 p_n^6}{p_n^8} \right) \\ &\simeq -\frac{b^{1/4}}{P_b^{1/4}} \int_{\epsilon}^{\infty} \frac{dp}{2\pi} \log \left(\frac{p^8}{(p^4 + 1)^2 - \zeta^2 p^6} \right) \quad \text{with } \epsilon := \frac{2\pi P_b^{1/4}}{b^{1/4} L_c} \\ &= -\frac{b^{1/4}}{P_b^{1/4}} \left[\int_{\epsilon}^{\infty} \frac{dp}{2\pi} \log \left(\frac{p^8}{(p^4 + 1)^2} \right) - \int_{\epsilon}^{\infty} \frac{dp}{2\pi} \log \left(1 - \frac{\zeta^2 p^6}{(p^4 + 1)^2} \right) \right] \end{aligned} \quad (6.36)$$

The first integral results in:

$$\begin{aligned} \int_{\epsilon}^{\infty} \frac{dp}{2\pi} \log \left(\frac{p^8}{(p^4 + 1)^2} \right) &= \frac{\sqrt{2}}{\pi} \left(\arctan(1 - \sqrt{2}p) - \arctan(1 + \sqrt{2}p) \right) \\ &\quad + \frac{1}{\sqrt{2}\pi} \log \left(\frac{1 - \sqrt{2}p + p^2}{1 + \sqrt{2}p + p^2} \right) + \frac{p}{\pi} \log \left(\frac{p^4}{1 + p^4} \right) \Bigg|_{\epsilon}^{\infty} \\ &= -\sqrt{2} - \frac{4}{\pi} \epsilon \log(\epsilon) \end{aligned} \quad (6.37)$$

and the second, making use of the fact that $\zeta p^3 < p^4 + 1$, for $\zeta < \zeta_{cr}$, and noting that the series converges uniformly in any closed interval contained in $[0, \zeta_{cr})$, in:

$$\begin{aligned} \int_{\epsilon}^{\infty} \frac{dp}{2\pi} \log \left(1 - \frac{\zeta^2 p^6}{(p^4 + 1)^2} \right) &= -\sum_{n=1}^{\infty} \frac{1}{n} \int_{\epsilon}^{\infty} \frac{dp}{2\pi} \left(\frac{\zeta^2 p^6}{(p^4 + 1)^2} \right)^n \\ &= -\sum_{n=0}^{\infty} \frac{\Gamma(n/2 - 1/4) \Gamma(3n/2 + 1/4) \zeta^{2n}}{4\pi (2n)!} - \sqrt{2} \end{aligned}$$

This can be rewritten with the help of standard gamma function identities as:

$$= -\sqrt{2} \left[1 - {}_3F_2 \left(-\frac{1}{4}, \frac{1}{12}, \frac{5}{12}; \frac{1}{4}, \frac{1}{2}; \frac{\xi^4}{\xi_{cr}^4} \right) + \frac{3\xi^2}{32} {}_3F_2 \left(\frac{1}{4}, \frac{7}{12}, \frac{11}{12}; \frac{3}{4}, \frac{3}{2}; \frac{\xi^4}{\xi_{cr}^4} \right) \right] + \mathcal{O}(\epsilon^7) \quad (6.38)$$

making the bifurcation point explicit. The free energy of confinement is finally given by:

$$\mathfrak{f} = \frac{b^{1/4}}{P_b^{1/4}} \sqrt{2} \left[{}_3F_2 \left(-\frac{1}{4}, \frac{1}{12}, \frac{5}{12}; \frac{1}{4}, \frac{1}{2}; \frac{\xi^4}{\xi_{cr}^4} \right) - \frac{3\xi^2}{32} {}_3F_2 \left(\frac{1}{4}, \frac{7}{12}, \frac{11}{12}; \frac{3}{4}, \frac{3}{2}; \frac{\xi^4}{\xi_{cr}^4} \right) \right] \quad (6.39)$$

or defining the “small” parameter $x := \xi/\xi_{cr}$ and the dimensionless parameter $\gamma := \frac{2\pi P_c' \sqrt{2}}{\xi_{cr} P_b}$

$$\begin{aligned} g := \frac{\mathfrak{f}}{\gamma \text{lk}} &= \frac{1}{x} {}_3F_2 \left(-\frac{1}{4}, \frac{1}{12}, \frac{5}{12}; \frac{1}{4}, \frac{1}{2}; x^4 \right) - \frac{x}{2\sqrt{3}} {}_3F_2 \left(\frac{1}{4}, \frac{7}{12}, \frac{11}{12}; \frac{3}{4}, \frac{3}{2}; x^4 \right) \\ &= \frac{1}{x} - \frac{x}{2\sqrt{3}} - \frac{5x^3}{72} + \mathcal{O}(x^7) \end{aligned}$$

An estimate of the rest term can be obtained using the asymptotic expansion of the gamma function:

$$\begin{aligned} &\simeq \frac{1}{x} - \frac{x}{2\sqrt{3}} - \frac{5x^3}{72} - \frac{x^5}{4\sqrt{\pi}(1-x^2)} \\ &= \sum_{n=0}^{\infty} a_n x^{2n-1}, \text{ with } a_n := \frac{\Gamma(n/2 - 1/4)\Gamma(3n/2 + 1/4)\xi_{cr}^{2n}}{4\pi\sqrt{2}(2n)!} \end{aligned} \quad (6.40)$$

It is somewhat unexpected that the two expressions for the free energy equation (6.34) and equation (6.39) are equivalent, but the second can be seen as the Laurent series of the first. It is useful to express the free energy in terms of the width of the fluctuations in the channel. For long chains this can be easily obtained from the free energy density (Burkhardt):

$$z := \frac{P_b \gamma^3 \text{lk}^3}{2} \langle \mathbf{r}^2 \rangle = \frac{P_b \gamma^3 \text{lk}^3}{2} 2 \frac{\partial \mathfrak{f}}{\partial b} = -x^5 \frac{\partial g}{\partial x} = - \sum_{n=0}^{\infty} (2n-1) a_n x^{2n+3},$$

or in generalized Hypergeometric functions:

$$\begin{aligned} z &= x^3 {}_3F_2 \left(-\frac{1}{4}, \frac{1}{12}, \frac{5}{12}; \frac{1}{4}, \frac{1}{2}; x^4 \right) + \frac{1}{2\sqrt{3}} x^5 {}_3F_2 \left(\frac{1}{4}, \frac{7}{12}, \frac{11}{12}; \frac{3}{4}, \frac{3}{2}; x^4 \right) \\ &\quad + \frac{5}{18} x^7 {}_3F_2 \left(\frac{3}{4}, \frac{13}{12}, \frac{17}{12}; \frac{5}{4}, \frac{3}{2}; x^4 \right) + \frac{77}{324\sqrt{3}} x^9 {}_3F_2 \left(\frac{5}{4}, \frac{19}{12}, \frac{23}{12}; \frac{7}{4}, \frac{5}{2}; x^4 \right) \end{aligned}$$

We now wish to invert the series (6.41). We use a standard trick to rewrite the series in a form that makes it suitable for Lagrange inversion, namely as a series where the derivative at the point of inversion is finite. We first write

$$z(x) = a_0 x^3 \left(1 - \sum_{n=1}^{\infty} (2n-1) \frac{a_n}{a_0} x^{2n} \right), \quad (6.41)$$

then consider the following series:

$$y(x) := \sqrt[3]{z(x)} = \sqrt[3]{a_0} x \left[1 + \sum_{k=1}^{\infty} \frac{1}{k!} \frac{\Gamma(-1/3 + k)}{\Gamma(-1/3)} \left(\sum_{n=1}^{\infty} (2n-1) \frac{a_n}{a_0} x^{2n} \right)^k \right], \quad (6.42)$$

and finally apply Lagrange inversion on $y(x)$:

$$x(z) = \sum_{n=1}^{\infty} \frac{1}{n!} \frac{d^{n-1}}{dx^{n-1}} \left(\frac{x}{y(x)} \right)^n \Big|_{x=0} z^{n/3} \quad (6.43)$$

The first terms of the resulting series are:

$$\begin{aligned} x(z) &= z^{1/3} - \frac{z}{6\sqrt{3}} - \frac{7z^{5/3}}{216} + \mathcal{O}(z^{7/3}) \\ g(z) &= \frac{1}{z^{1/3}} - \frac{z^{1/3}}{3\sqrt{3}} + \frac{5z^{5/3}}{243\sqrt{3}} + \mathcal{O}(z^{7/3}) \end{aligned}$$

or in terms of the unscaled variables:

$$\mathfrak{f} = \frac{2^{1/3}}{P_b^{1/3} \langle \mathbf{r}^2 \rangle^{1/3}} - \frac{(2\pi \text{lk } P_c')^2}{8 \cdot 2^{1/3} P_b^2} (P_b \langle \mathbf{r}^2 \rangle)^{1/3} + \mathcal{O}\left(\frac{(2\pi \text{lk } P_c')^5}{P_b^6} (P_b \langle \mathbf{r}^2 \rangle)^{5/3}\right) \quad (6.44)$$

The demand $\zeta \ll \zeta_{cr}$ translates into $(P_b \langle \mathbf{r}^2 \rangle)^{1/3} \ll P_b / (2\pi P_c' \text{lk})$. In the plectoneme the free energy of the confining potential is taken into account. When the potential causing the confinement potential is separately known, but complicated, the harmonic potential is just there to get an estimate for the cost of confining the chain and so its contribution needs to be subtracted [153] to get the confinement free energy:

$$\begin{aligned} \mathfrak{f}_{pot} &= \frac{1}{2} b \langle \mathbf{r}^2 \rangle = \frac{1}{4} \frac{2^{1/3}}{(P_b \langle \mathbf{r}^2 \rangle)^{1/3}} + \frac{(2\pi \text{lk } P_c')^2}{16 \cdot 2^{1/3} P_b^2} (P_b \langle \mathbf{r}^2 \rangle)^{1/3} + \frac{3(2\pi \text{lk } P_c')^4}{2^8 P_b^4} P_b \langle \mathbf{r}^2 \rangle \\ &\quad + \mathcal{O}\left(\frac{(2\pi \text{lk } P_c')^5}{P_b^6} (P_b \langle \mathbf{r}^2 \rangle)^{5/3}\right) \end{aligned}$$

and so we find

$$\begin{aligned} f_{conf} = & \frac{3}{2^{5/3}} \frac{1}{(P_b \langle \mathbf{r}^2 \rangle)^{1/3}} - \frac{3(2\pi \text{lk } P_c')^2}{16 \cdot 2^{1/3} P_b^2} (P_b \langle \mathbf{r}^2 \rangle)^{1/3} - \frac{3(2\pi \text{lk } P_c')^4}{2^8 P_b^4} P_b \langle \mathbf{r}^2 \rangle \\ & + \mathcal{O}\left(\frac{(2\pi \text{lk } P_c')^5}{P_b^6} (P_b \langle \mathbf{r}^2 \rangle)^{5/3}\right) \end{aligned} \quad (6.45)$$

We next consider the average thermal writhe, which is conjugate to the linking number in the fluctuation free energy:

$$\begin{aligned} \omega = & -\frac{1}{2\pi} \frac{\partial f}{\partial (2\pi P_c' \text{lk})} \Big|_b \\ = & \frac{3}{2^5 \sqrt{2}} \frac{P_c' \text{lk}}{P_b^2} (P_b \langle \mathbf{r}^2 \rangle)^{1/3} + \frac{317}{2^{12} \sqrt{2}} \frac{4\pi^2 (P_c' \text{lk})^3}{P_b^4} P_b \langle \mathbf{r}^2 \rangle + \mathcal{O}\left(\frac{(2\pi \text{lk } P_c')^5}{P_b^6} (P_b \langle \mathbf{r}^2 \rangle)^{5/3}\right) \end{aligned} \quad (6.46)$$

Of course Whites relation gives us at the same time the average twist density.

To calculate the extension we add a term $(\lambda/2)(\frac{d\mathbf{r}}{ds})^2$ to the fluctuation Hamiltonian (6.20). The extension is then given by, using the results of section 6.1:

$$\rho := \frac{\Delta z}{L_c} = \left(1 + \frac{B}{S} 2\pi \text{lk} - \frac{\partial f}{\partial \lambda} \Big|_{\lambda=0}\right) \quad (6.47)$$

The resulting free energy expression changes to:

$$\begin{aligned} f = & -\frac{b^{1/4}}{P_b^{1/4}} \int_0^\infty \frac{dp}{2\pi} \log \left(\frac{p^8}{(p^4 + \hat{\lambda} p^2 + 1)^2 - \bar{\xi}^2(\lambda) p^6} \right) \\ = & -\frac{b^{1/4}}{P_b^{1/4}} \left[\int_0^\infty \frac{dp}{2\pi} \log \left(\frac{p^8}{(p^4 + \hat{\lambda} p^2 + 1)^2} \right) + \sum_{n=1}^\infty \frac{1}{n} \int_0^\infty \frac{dp}{2\pi} \left(\frac{\bar{\xi}^2(\lambda) p^6}{(p^4 + \hat{\lambda} p^2 + 1)^2} \right)^n \right], \end{aligned} \quad (6.48)$$

with $\hat{\lambda} = \lambda P_b^{-1/2} b^{-1/2}$ and $\bar{\xi}(\lambda) = \frac{2\pi P_c' \text{lk} + B \lambda / (S)}{P_b^{3/4} b^{1/4}}$. We need $\partial_\lambda f$ at $\lambda = 0$. The first integral results in:

$$\begin{aligned} \frac{\partial}{\partial \lambda} \int_0^\infty \frac{dp}{2\pi} \log \left(\frac{p^8}{(p^4 + \hat{\lambda} p^2 + 1)^2} \right) \Big|_{\lambda=0} &= P_b^{-1/2} b^{-1/2} \frac{\partial}{\partial \hat{\lambda}} \left(-2 \sqrt{\frac{1}{2} + \frac{\hat{\lambda}}{4}} \right) \Big|_{\hat{\lambda}=0} \\ &= -2^{-3/2} P_b^{-1/2} b^{-1/2} \end{aligned} \quad (6.49)$$

while the second integral results in:

$$\begin{aligned}
& \left. \frac{\partial}{\partial \lambda} \int_0^\infty \frac{dp}{2\pi n} \left(\frac{\bar{\zeta}^2 p^6}{(p^4 + \hat{\lambda} p^2 + 1)^2} \right)^n \right|_{\lambda=0} \\
&= -\frac{1}{\sqrt{b} P_b} \int_0^\infty \frac{dp}{\pi} \left(\frac{\zeta^2 p^6}{(p^4 + 1)^2} \right)^n \frac{p^2}{p^4 + 1} + \frac{B \zeta^{2n-1}}{S P_b^{3/4} b^{1/4}} \int_0^\infty \frac{dp}{\pi} \left(\frac{p^6}{(p^4 + 1)^2} \right)^n \\
&= -\frac{\Gamma(n/2 + 1/4) \Gamma(3n/2 + 3/4)}{4\pi (2n)! (b P_b)^{1/2}} \zeta^{2n} + \frac{B \zeta^{2n-1} \Gamma(n/2 - 1/4) \Gamma(3n/2 + 1/4)}{4\pi (2n-1)! b^{1/4} S P_b^{3/4}}
\end{aligned} \tag{6.50}$$

And so we find as contraction factor:

$$\begin{aligned}
\rho &= 1 - \frac{1}{2\sqrt{2}b^{1/4} P_b^{3/4}} + \frac{3B\zeta}{8\sqrt{2}P_b S} - \frac{5\zeta^2}{64\sqrt{2}b^{1/4} P_b^{3/4}} \\
&= 1 - \frac{2B\ell k}{S} - \frac{(1 - \frac{3BP_c' \pi \ell k}{2SP_b})}{2^{4/3} P_b} (P_b \langle \mathbf{r}^2 \rangle)^{1/3} - \frac{(1 + \frac{3BP_c' \pi \ell k}{8P_b S})(P_c' \pi \ell k)^2}{4P_b^3} P_b \langle \mathbf{r}^2 \rangle
\end{aligned} \tag{6.51}$$

6.3 Non isotropic confinement

We now consider a confinement in a channel, where the confining potential in the two directions have a different strength. The Hamiltonian (6.20) changes to:

$$\mathcal{H} = \int_0^{L_c} ds \left[\frac{P_b}{2} \left(\frac{d^2 \mathbf{r}(s)}{ds^2} \right)^2 + \frac{b_x}{2} r_x^2(s) + \frac{b_y}{2} r_y^2(s) - \pi P_c' \ell k (\dot{r}_x \ddot{r}_y - \ddot{r}_x \dot{r}_y) \right] + 2\pi^2 P_c' \ell k^2 L_c \tag{6.52}$$

The rescaling is as before except that we replace b with

$$\lambda(b_x, b_y) := \frac{2(33(b_x^2 b_y + b_x b_y^2) + (b_x^2 + 14b_x b_y + b_y^2)^{3/2} - b_x^3 - b_y^3)}{27b_x b_y}. \tag{6.53}$$

which has the dimension of $[L^{-3}]$. With that choice the bifurcation point is at:

$$\zeta_{cr} := \frac{2\pi P_c' \ell k_{cr}}{P_b^{3/4} \lambda^{1/4}} = 1. \tag{6.54}$$

And so we have again a suitable parameter for an expansion. The free energy corresponding to (6.36) is now given by:

$$\begin{aligned} \mathfrak{f} &= -\frac{\lambda^{1/4}}{P_b^{1/4}} \int_0^\infty \frac{dp}{2\pi} \log \left(\frac{p^8}{(p^4 + b_x/\lambda)(p^4 + b_y/\lambda) - \zeta^2 p^6} \right) \\ &= \frac{\lambda^{1/4}}{P_b^{1/4}} \left(\frac{b_x^{1/4} + b_y^{1/4}}{\sqrt{2}\lambda^{1/4}} \right. \\ &\quad \left. - \frac{\lambda^{1/4}(b_x^{3/4} - b_y^{3/4})}{4\sqrt{2}(b_x - b_y)} \zeta^2 - \frac{\lambda^{3/4}(b_x^{9/4} - 9b_x^{5/4}b_y + 9b_xb_y^{5/4} - b_y^{9/4})}{32\sqrt{2}(b_x - b_y)^3} \zeta^4 + \mathcal{O}(\zeta^6) \right) \end{aligned} \quad (6.55)$$

The λ 's neatly cancel. This is obvious from the way the scaling was defined but this makes the expansion more transparent. Since λ cancels we change to a new parameter $\alpha := 2\pi P_c' \text{lk}$. The critical point can be written as

$$\left(2\pi P_c' \text{lk}_{cr} \right)^2 = \frac{4\sqrt{2}(b_x P_b^3 + b_y P_b^3) + 2\sqrt{(2(b_x + b_y)^2 + 24b_x b_x) P_b^6}}{3\sqrt{(b_x P_b^3 + b_y P_b^3) + \sqrt{((b_x P_b^3 + b_y)^2 + 12b_x b_x) P_b^6}}} \quad (6.56)$$

To get an expression for the free energy as function of the second moment of the fluctuations we will use a multivariate extension of Lagrange inversion [174, 175]. For the choice of point of reversion and parameterization we will first try to treat both directions on equal footing.

We start by defining suitable scales and parameters. Define, with $i = x$ or y :

$$z_i := \frac{\alpha}{P_b^{3/4} b_i^{1/4}} \quad \mathfrak{g}(z_x, z_y) := \frac{P_b}{\alpha} \mathfrak{f}[b_x(z_x), b_y(z_y)], \quad (6.57)$$

with $i = x$ or y . The average fluctuation variance can now be calculated (as before) as:

$$v_i(z_x, z_y) := 2 \frac{\alpha^3}{P_b^2} \langle r_i^2 \rangle(z_x, z_y) = -z_i^5 \partial_{z_i} \mathfrak{g}(z_x, z_y) \quad (6.58)$$

We need a formal power series $f_{x,y}$ that implicitly defines $z_{x,y}$ as a power series in $v_{x,y}$ through $z_i = v_i^{1/3} f_i(z_x, z_y)$. Note that we have taken the (reduced) variance to the power $1/3$, since this functional equation has only a solution, that is then also unique, when $f_i(0, 0) \neq 0$. We define f_i as:

$$f_i(z_x, z_y) := \frac{z_i}{v_i^{1/3}(z_x, z_y)} \quad (6.59)$$

The coefficient for the term $(\sqrt[3]{v_x})^n (\sqrt[3]{v_y})^m$, n, m not necessarily positive, of \mathfrak{g} , as a power series in $u_i := \sqrt[3]{v_i}$, is given by the Good-Lagrange formula [174, 175]

$$\begin{aligned} [u_{x,y}]^{n,m} \mathfrak{g}(z_x(u_x), z_y(u_y)) \\ &= [z_{x,y}]^{n,m} \mathfrak{g}(z_x, z_y) f_x^n(z_x, z_y) f_y^m(z_x, z_y) \text{Det} \left(\delta_{i,j} - \frac{z_i}{f_j(z_x, z_y)} \frac{\partial f_j(z_x, z_y)}{\partial z_i} \right) \\ &= [z_{x,y}]^{n,m} \mathfrak{g}(z_x, z_y) f_x^n(z_x, z_y) f_y^m(z_x, z_y) \frac{1}{9} \text{Det} \left(\frac{z_i}{v_j(z_x, z_y)} \frac{\partial v_j(z_x, z_y)}{\partial z_i} \right) \end{aligned} \quad (6.60)$$

where $[x_{1,2}]^{n,m} F(x_{1,2})$ denotes the coefficient of the monomial $x_1^n x_2^m$ in the (formal) power series F . Of course the same would hold would we replace \mathfrak{g} with some other power series. From the above we find:

$$\begin{aligned} \mathfrak{g} = & \frac{1}{2^{2/3}} (v_x^{-1/3} + v_y^{-1/3}) - \frac{1}{6 \cdot 2^{1/3}} (v_x^{1/3} + v_y^{1/3}) + \frac{1}{6 \cdot 2^{1/3}} (v_x^{4/3} v_y^{-1} + v_x^{-1} v_y^{4/3}) \\ & - \frac{1}{6 \cdot 2^{1/3}} (v_x^{5/3} v_y^{-4/3} + v_x^{-4/3} v_y^{5/3}) + \frac{1}{324 \cdot 2^{2/3}} (v_x^{5/3} + v_y^{5/3}) \end{aligned} \quad (6.61)$$

and we clearly have a problem: there are an infinite number of terms in $(v_x^{(2n+1)/3} + v_y^{(2n+1)/3})$ with coefficients that do not decrease. To resolve this we will redefine our expansion parameters. We will distinguish two cases: either the harmonic potentials are almost equal, $b_x \approx b_y$ and $\langle r_x^2 \rangle \approx \langle r_y^2 \rangle$, or one of them is much smaller, say $b_x \ll b_y$. In the end we will see that they both lead to the same answer.

6.3.1 Almost isotropic case

In the first case we will use $z := z_x$ and $\delta_w := z_y/z_x - 1$ as parameterization of the potentials and $v := v_x$, $\Delta_w := \langle r_y^2 \rangle / \langle r_x^2 \rangle - 1$ as variance parameters. The defining power series are now:

$$f_v(z, \delta_w) := \frac{z}{v^{1/3}(z, \delta_w)} \quad \text{and} \quad f_{\Delta_w}(z, \delta_w) := \frac{\delta_w}{\Delta_w(z, \delta_w)} \quad (6.62)$$

resulting in the Good-Lagrange equation:

$$\begin{aligned} [\sqrt[3]{v}, \Delta_w]^{n,m} \mathfrak{g}(z(\sqrt[3]{v}, \Delta_w), \delta_w(\sqrt[3]{v}, \Delta_w)) = \\ [z, \delta_w]^{n,m} \mathfrak{g}(z, \delta_w) \frac{f_v^n(z, \delta_w) f_{\Delta_w}^m(z, \delta_w) z \delta_w}{3v(z, \delta_w) \Delta_w(z, \delta_w)} \text{Det} \left(\begin{array}{cc} \partial_z v(z, \delta_w) & \partial_z \Delta_w(z, \delta_w) \\ \partial_{\delta_w} v(z, \delta_w) & \partial_{\delta_w} \Delta_w(z, \delta_w) \end{array} \right) \end{aligned} \quad (6.63)$$

From this we find:

$$\begin{aligned} g &= \left(2^{1/3} - \frac{\Delta_w}{3 \cdot 2^{2/3}} + \mathcal{O}(\Delta_w^2) \right) v^{-1/3} - \left(\frac{1}{8 \cdot 2^{1/3}} + \frac{\Delta_w}{48 \cdot 2^{1/3}} + \mathcal{O}(\Delta_w^2) \right) v^{1/3} + \mathcal{O}(v^{5/3}) \Rightarrow \\ f &= \frac{1 - \Delta_w/6}{(P_b \langle r_x^2 \rangle)^{1/3}} - \frac{\alpha^2(1 + \Delta_w/6)}{8 P_b^2} (P_b \langle r_x^2 \rangle)^{1/3} + \mathcal{O}(\alpha^4) \end{aligned} \quad (6.64)$$

Also here we can calculate the entropic contribution to the confinement free energy, subtracting the contribution of the artificial harmonic potential (in case the confinement potential has been taken care of separately). Replacing g in the Good-Lagrange equation (6.63) with the expectation value of the reduced potential energy density $\langle U \rangle = \frac{1}{2}(b_x \langle r_x^2 \rangle + b_y \langle r_y^2 \rangle)$ we find:

$$\begin{aligned} [\sqrt[3]{v}, \Delta_w]^{n,m} \langle U \rangle (z(\sqrt[3]{v}, \Delta_w), \delta_w(\sqrt[3]{v}, \Delta_w)) &= \\ \frac{\alpha^2}{2 P_b} [z, \delta_w]^{n,m} \frac{1}{2} (z^{-4} v(z, \delta_w) + [z(1 + \delta_w)]^{-4} v(z, \delta_w)(1 + \Delta_w(z, \delta_w)) & \\ \frac{f_v^n(z, \delta_w) f_{\Delta_w}^m(z, \delta_w) z \delta_w}{3 v(z, \delta_w) \Delta_w(z, \delta_w)} \text{Det} \begin{pmatrix} \partial_z v(z, \delta_w) & \partial_z \Delta_w(z, \delta_w) \\ \partial_{\delta_w} v(z, \delta_w) & \partial_{\delta_w} \Delta_w(z, \delta_w) \end{pmatrix} \Rightarrow & \\ \langle U \rangle = \frac{1 - \Delta_w/6}{(4 P_b \langle r_x^2 \rangle)^{1/3}} + \frac{\alpha^2(1 + \Delta_w/6)}{16 P_b^2} (P_b \langle r_x^2 \rangle)^{1/3} + \mathcal{O}(\alpha^6) & \end{aligned} \quad (6.65)$$

and so

$$f_{conf} = f - \langle U \rangle = \frac{(3 - \Delta_w/2)}{4(P_b \langle r_x^2 \rangle)^{1/3}} - \frac{\alpha^2(1 + \Delta_w/6)}{16 P_b^2} (P_b \langle r_x^2 \rangle)^{1/3} + \mathcal{O}(\alpha^4) \quad (6.66)$$

Note that these results lead to the right isotropic expressions since:

$$\frac{1}{\langle \mathbf{r}^2 \rangle^{1/3}} = \frac{1}{(\langle r_x^2 \rangle + \langle r_y^2 \rangle)^{1/3}} \approx \frac{1 - \Delta_w/6}{2^{1/3} \langle r_x^2 \rangle^{1/3}} \quad (6.67)$$

For the extension we add again a fictitious force term as in the isotropic case, leading to

$$\begin{aligned}\rho_w &= 1 - \frac{1}{P_b} \sum_{n=0}^{\infty} \int_0^{\infty} \frac{dp}{2\pi} \frac{p^2(2p^4 + b_x + b_y)p^{6n}}{((p^4 + b_x)(p^4 + b_y))^{2n+1}} \\ &= 1 - \frac{1}{4\sqrt{2} P_b^{3/4}} \left(\frac{b_x^{1/4} + b_y^{1/4}}{(b_x b_y)^{1/4}} + \frac{5\alpha^2}{4(b_x^{1/4} + b_y^{1/4})(\sqrt{b_x} + \sqrt{b_y}) P_b^{3/2}} \right. \\ &\quad \left. + \frac{11(b_x + b_y + 6\sqrt{b_x b_y} + 3b_x^{3/4}b_y^{1/4} + 3b_x^{1/4}b_y^{3/4})\alpha^4}{32\sqrt{2}(b_x^{3/4} + b_y^{3/4})(\sqrt{b_x} + \sqrt{b_y})^3 P_b^3} + \mathcal{O}(\alpha^6) \right) \end{aligned} \quad (6.68)$$

relying again on the inversion formula. This finally results in:

$$\rho_w = 1 - \frac{(1 + \Delta_w/6)}{2 P_b} (P_b \langle r_x^2 \rangle)^{1/3} - \frac{(1 + \Delta_w/2)\alpha^2}{8 P_b^3} P_b \langle r_x^2 \rangle \quad (6.69)$$

Finally we calculate the writhe density as function of the linking number density:

$$\omega = \frac{(3 + \Delta_w/2) P_c' \text{lk}}{8 P_b^2} (P_b \langle r_x^2 \rangle)^{1/3} + \frac{(3 + 3\Delta_w/2)\pi^2 (P_c' \text{lk})^3}{8 P_b^4} P_b \langle r_x^2 \rangle \quad (6.70)$$

Next we will check the limit of high anisotropy.

6.3.2 Strong anisotropy

We assume $b_x \gg b_y \Rightarrow \langle r_x^2 \rangle \ll \langle r_y^2 \rangle$. We change δ_w and Δ_w to $\delta_s := z_x/z_y$ and $\Delta_s := (\langle r_x^2 \rangle / \langle r_y^2 \rangle)$, keeping the other two variables from the previous case. The defining power series are:

$$f_v(z, \delta_s) := \frac{z}{v^{1/3}(z, \delta_s)} \quad \text{and} \quad f_{\Delta_s}(z, \delta_s) := \frac{\delta_s}{\Delta_s^{1/3}(z, \delta_s)} \quad (6.71)$$

Note that this time we need $\Delta_s^{1/3}$ since to lowest order $\Delta_s \sim \delta_s^3$. As inversion formula we find:

$$\begin{aligned} & [\sqrt[3]{v}, \sqrt[3]{\Delta_s}]^{n,m} \mathfrak{g}(z(\sqrt[3]{v}, \sqrt[3]{\Delta_s}), \delta_s(\sqrt[3]{v}, \sqrt[3]{\Delta_s})) = \\ & [z, \delta_s]^{n,m} \mathfrak{g}(z, \delta_s) \frac{f_v^n(z, \delta_s) f_{\Delta_s}^m(z, \delta_s) z \delta_s}{9v(z, \delta_s) \Delta_s(z, \delta_s)} \text{Det} \begin{pmatrix} \partial_z v(z, \delta_s) & \partial_z \Delta_s(z, \delta_s) \\ \partial_{\delta_s} v(z, \delta_s) & \partial_{\delta_s} \Delta_s(z, \delta_s) \end{pmatrix} \end{aligned} \quad (6.72)$$

resulting in:

$$\begin{aligned} g &= \frac{1}{2^{2/3}} \left(1 + \Delta_s^{1/3} \right) v^{-1/3} - \frac{1}{6 \cdot 2^{1/3}} \left(1 - \Delta_s + \Delta_s^{4/3} + \mathcal{O}(\Delta_s^{7/3}) \right) v^{1/3} \\ &\quad + \frac{1}{3 \cdot 2^{2/3}} \left(\frac{1}{108} - \frac{1}{36} \Delta_s + \frac{1}{3} \Delta_s^{4/3} - \frac{1}{2} \Delta_s^{5/3} + \mathcal{O}(\Delta_s^{6/3}) \right) v^{5/3} + \mathcal{O}(v^{7/3}) \Rightarrow \end{aligned}$$

We can in fact sum up all terms in Δ_s in the second term to get as compact expression:

$$\begin{aligned} f &= \frac{1 + \Delta_s^{1/3}}{2(P_b \langle r_x^2 \rangle)^{1/3}} - \frac{(1 - \Delta_s)(2\pi P_c' l k)^2}{6 P_b^2 (1 - \Delta_s^{4/3})} (P_b \langle r_x^2 \rangle)^{1/3} \\ &= \frac{1 + \Delta_s^{1/3}}{2(P_b \langle r_x^2 \rangle)^{1/3}} - \frac{(1 + \Delta_s^{1/3} + \Delta_s^{2/3})(2\pi P_c' l k)^2}{6 P_b^2 (1 + \Delta_s^{1/3})(1 + \Delta_s^{2/3})} (P_b \langle r_x^2 \rangle)^{1/3} \end{aligned} \quad (6.73)$$

Remembering the definition of Δ_s it is immediately clear that the end result can be written in a symmetric way covering all cases in one formula. It is useful to introduce now the concept of deflection length of confinement as

$$\lambda_{x,y} := (P_b \langle r_{x,y}^2 \rangle)^{1/3} \quad \bar{\lambda} = 2 \frac{\lambda_x^3 \lambda_y + \lambda_x^2 \lambda_y^2 + \lambda_x \lambda_y^3}{(\lambda_x + \lambda_y)(\lambda_x^2 + \lambda_y^2)} \quad (6.74)$$

as a length scale over which the potential starts to dominate thermal motion. The factor 2 is a matter of convention. The torsion mixes the two confinement directions. The new deflection length that emerges can be seen as an effective one, dominated by the smallest dimension in case of highly anisotropic confinement, equal to the conventional one for isotropic confinement. With these definitions the final result of this chapter can be written as:

$$f = \frac{1}{2} \left(\frac{P_b}{\lambda_x} + \frac{P_b}{\lambda_y} \right) - \frac{1}{12} \frac{\bar{\lambda} (\pi P_c' l k)^2}{P_b^2} \quad (6.75a)$$

Not to become too repetitive we just mention the results for all other relevant quantities:

$$\langle U \rangle = \frac{1}{8} \left(\frac{P_b}{\lambda_x} + \frac{P_b}{\lambda_y} \right) + \frac{1}{24} \frac{\bar{\lambda} (\pi P_c' l k)^2}{P_b^2} \quad (6.75b)$$

$$f_{conf} = \frac{3}{8} \left(\frac{P_b}{\lambda_x} + \frac{P_b}{\lambda_y} \right) - \frac{1}{8} \frac{\bar{\lambda} (\pi P_c' l k)^2}{P_b^2} \quad (6.75c)$$

$$\rho_s = 1 - \frac{2 B l k}{S} - \frac{1}{4} \left(\frac{\lambda_x}{P_b} + \frac{\lambda_y}{P_b} \right) + \frac{\bar{\lambda} B \pi P_c' l k}{2 S P_b^2} - \frac{(7\lambda_x^3 \lambda_y^5 - 2\lambda_x^4 \lambda_y^4 + 7\lambda_x^5 \lambda_y^3)(\pi P_c' l k)^2}{12(\lambda_x + \lambda_y)(7\lambda_x^2 + \lambda_y^2)^2 P_b^3} \quad (6.75d)$$

$$\omega = \frac{\bar{\lambda} P_c' l k}{4 P_b^2} \quad (6.75e)$$

Thermal Fluctuations and the Multi-Plectoneme Phase

To account for thermal fluctuations two strategies seem to dominate the theoretical considerations in the literature. They both do not consider the fluctuations per se in the plectoneme, but either conclude that plectoneme formation hardly affects the thermal fluctuations [150] or boldly consider the shortening only happening in the tails [176, 177]. Both approaches have their shortcomings.

In the first case, it not clear why the size of the thermal fluctuations inside the plectoneme should be the same as in the tails. The confinement of the chain in the plectoneme is the result of a subtle equilibrium between the applied tension, the electrostatic repulsion and the need to reduce the twist through writhe. Furthermore this procedure needs an extra surface charge reduction of the chain to reproduce experimental slopes [150].

The second approach, when properly applied, does not need this ad hoc charge reduction to get a reasonable agreement with some of the experiments but has the conceptual problem that there is no a priori reason why the plectoneme would be totally immune to fluctuations. The reasoning that thermal fluctuations are small within the plectoneme and thus can be ignored is erroneous since the plectoneme free energy has to be compared with the plectonemeless configuration where the finite fluctuations have a known dependence on tension and applied torque. The only conclusion one can draw, following this line of thought, is that the extreme reduction in the number of configurations prohibits plectoneme formation.

The influence of thermal fluctuations on free energy, extension and twist for linking numbers below the plectoneme transition are pretty well understood [172, 173]. This result can not be used within a plectoneme. That is why the free energy of the tails is often taken as the free energy of a worm-like chain under tension, not taking the effect of a constraint nonzero linking number into account, or alternatively putting all linking number dependence in an effective torsional stiffness [151] after a low torque expansion. The problem remains in that

there is no reason to assume that this effective torsional stiffness can be used within the plectoneme to account for the torsional part of the free energy.

We are using a detailed calculation of a confined worm-like chain under torsion. Our strategy is to integrate out short wavelength degrees of freedom, restricted to fluctuations around the straight chain and plectoneme solutions, treating the tails and the plectoneme separately. We will then calculate the free energy of the resulting effective Hamiltonian as a sum over the local minima.

7.1 Short wave length fluctuations

Below the transition we use the results from Moroz and Nelson [172] extended with a finite stretch modulus and twist stretch coupling as performed in Section 6.1. Comparing the expression for the free energy (6.13) with the calculations from [172], we see that (the inverse of) their expansion parameter K is replaced by:

$$K = \sqrt{f P_b - (\pi P_c' l k + \frac{B f}{2 S})^2} \quad (7.1)$$

The free energy density of the chain expressed in this factor can now be written as (6.13):

$$\begin{aligned} f_{\text{tail}} &= 2\pi^2 P_c l k^2 - \frac{(f - 2\pi B l k)^2}{2 S} - f + \frac{K}{P_b} \left(1 - \frac{1}{4 K} - \frac{1}{64 K^2} \right) \\ &\simeq f_{\text{tw}}^t - f \left(1 + \frac{f - 4\pi B l k}{2 S} \right) + \frac{1}{\lambda} \left(1 - \frac{\lambda}{4 P_b} - \frac{\lambda^2}{64 P_b^2} \right), \end{aligned} \quad (7.2)$$

with the twist free energy

$$f_{\text{tw}}^t \simeq 2\pi^2 P_c' \langle \text{tw}^2 \rangle = 2\pi^2 P_c' \left(1 - \frac{\lambda P_c'}{4 P_b^2} \right) l k^2, \quad (7.3)$$

where we have added higher order terms from [172] to the free energy density. The values for the stretch modulus, $S = 300 \text{ nm}^{-1}$, and the stretch-twist coupling, $B = -21$ we take from the recent paper by Sheinin and Wang [155]. The twist energy is one of the main results of Moroz et al. [172] who introduced the notion of the *thermally* renormalized torsional persistence length:

$$P_c^{\text{eff}}(\lambda) = \left(1 - \frac{\lambda P_c'}{4 P_b^2} \right) P_c' \quad (7.4)$$

The linking number that was put into the chain gets spread between twist and a thermal writhe that is not symmetric around the straight twisted rod, but has a directionality thereby

decreasing the twist. The expectation value of this writhe per unit length, $\omega_{\text{tail}}^{\text{th}}$, and the resulting twist density, tw , are given by equation (6.14) or to lowest order as:

$$\langle \omega_{\text{tail}}^{\text{th}} \rangle = \frac{P_c' \lambda}{4 P_b^2} \left(\text{lk} + \frac{B f}{2\pi S} \right) \Rightarrow \quad \langle \text{tw} \rangle = \text{lk} \left(1 - \frac{P_c' \lambda}{4 P_b^2} \right) - \frac{P_c' \lambda B f}{8\pi P_b^2 S} \quad (7.5)$$

The thermal shortening with finite size correction follows from equation (6.15):

$$\begin{aligned} \rho_{\text{tail}} = 1 + \frac{f - 2\pi B \text{lk}}{S} - \frac{1}{2K} \left(1 + \frac{1}{64K^2} + \dots \right) \left(1 - \frac{B}{2P_b S} (2\pi \text{lk} P_c' + \frac{B f}{S}) \right) \\ + \left(\frac{1 - \coth(\frac{L_c K}{P_b})}{2K} + \frac{P_b}{2L_c K^2} \right) \left(1 - \frac{B^2 f}{2P_b S^2} \right) \end{aligned} \quad (7.6)$$

The finite size correction differs from the correction given by [172] to make it valid for short chains, though the reasoning is the same. For a freely rotating WLC under tension the shortening factor is, up to quadratic order, given by [125]:

$$\rho_{\tau=0} = 1 - \frac{\coth(\frac{L_c K_{\tau=0}}{P_b})}{2K_{\tau=0}} + \frac{P_b}{2L_c K_{\tau=0}^2} \quad (7.7)$$

As can be read of from K , the critical buckling bifurcation point gets shifted upwards to:

$$\text{Lk}_{cr} = \frac{L_c}{2\pi P_c'} \left(2\sqrt{f P_b} - \frac{B f}{S} \right) \quad (7.8)$$

The validity of these expressions is limited to values of force and linking number that make the expansion factor K large enough. Moroz and Nelson argued that for K^2 larger than 3, the error in the extension should be below 10%, based on a comparison with the next term in the asymptotic expansion. There are 2 other sources for errors: the appearance of knotted configurations, that should have been excluded from the partition sum and configurations with a writhe that differs a multiple of 2 from the calculated writhe caused by the use of Fuller's equation. For large K when large deviations from the straight rod are highly suppressed the influence of these effects are small and we will consider a value of $K^2 = 3$ to be the lower bound below which the theoretical treatment of [172, 173] breaks down.

Once a plectoneme is formed one can think roughly of the solution as consisting of 3 distinct regions: the tails, where life is as in the straight pre buckling solution, the end-loop, and the plectoneme.

As was shown by Kulic et al [125], in a WLC under tension, it is the length of a loop, not the contour length of the chain forming the loop, that is to lowest order unaffected by thermal fluctuations. This has been shown for the case of a homoclinic parameter $t = 1$ loop with the two legs bound by a gliding ring at the contact point. There is no reason to doubt that this

will hold also for the end loops of the plectonemes, since they are sufficiently close to the closed loop, with the essential difference that the legs are not bound together but lie in an effective potential well resulting from a twist induced attraction and an electrostatic repulsion. Thermal fluctuations necessarily open the loop from its ground state value, thus decreasing its length. This loop destabilization effect becomes unimportant for a finite size plectoneme configuration, since loop opening and plectoneme radius are linked. To avoid unnecessary complications we will just ignore the entropic loop contributions and instead determine the relevant loop size from the plectoneme. The advantage of not having to introduce a detailed end loop entropic contribution to the free energy more than compensates for the small error it might produce in the free energy close to a possible plectonemeless loop configuration. In general it hardly affects the jump in length seen in the turn extension plots at the transition, since jumps indicate a finite size plectoneme at the transition.

The plectoneme part of the solution needs a more careful examination. As starting point we take the calculations by Ubbink and Odijk [153]. They considered one strand of the regular plectoneme fluctuating in the mean field potential of the opposing strand. They assume the fluctuations to have a Gaussian distribution around their average in two directions perpendicular to the strand. One direction is chosen pointing towards the opposing strand, the radial direction, the other normal to this direction, the pitch direction. Fluctuations in the radial direction are dominated by the exponent of the electrostatic interactions, while fluctuations in the pitch direction have much less influence on the energetics. Let us stress the advantage of this approach over expanding the effective confining potential around the ground state. In the radial direction the potential is highly skewed, exponentially increasing towards smaller radius. A harmonic approximation would only be valid in a tiny region around the ground state. Instead the point of view taken here is that the fluctuations are small compared to the typical length-scale of the chain, i.e. the persistence length. Denoting the standard deviation of the Gaussian distribution in the radial and pitch direction by respectively σ_r and σ_p , the electrostatic part of the free energy changes approximately to [153]:

$$f_{\text{el}}(t, \alpha, \sigma_r) = \epsilon_{\text{el}}^0 e^{4\kappa^2 \sigma_r^2} = \frac{q_{\text{eff}}^2 Q_B}{2} \sqrt{\frac{\pi}{\kappa R(t)}} e^{4\kappa^2 \sigma_r^2 - 2\kappa R(t)} Z(\cot(\alpha)). \quad (7.9)$$

It is clear that the steep exponential rise of this free energy contribution limits the value of σ_r to be of order $(2\kappa)^{-1}$. This clearly distinguishes the magnitude of radial fluctuations from those in the “pitch-direction”. It was argued in [178] that the standard deviation in the pitch direction should be of the order of the pitch itself. This one expects also purely on geometric grounds. The exact value is not that easy to calculate, but since it is considerably larger than the radial standard deviation, our results are fairly insensitive to its exact value, as it is the tightest direction that dominates the free energy of confinement (see below). In the following we will make the choice $\sigma_p = \pi R \sin(\alpha)$, which is the width of the virtual channel where a strand can move in perpendicular to the radial direction until it meets the opposing strand. The undulating chain contracts slightly with a factor ρ_{pl} , that we will discuss shortly. This

contraction decreases the bending energy density and the writhe density of the plectoneme per contour length in a nontrivial way. In appendix C.1 it is shown that they change to:

$$\epsilon_{\text{bend}} \rightarrow \bar{f}_{\text{bend}} = \rho_{\text{pl}}^4 \epsilon_{\text{bend}} = \rho_{\text{pl}}^4 \frac{P_b \cos^4(\alpha)}{2 R^2} \quad \omega \rightarrow \rho_{\text{pl}} \omega = \rho_{\text{pl}} \frac{\sin(2\alpha)}{4\pi R} \quad (7.10)$$

For the entropic cost of confinement we cannot neglect the twist in the chain. The expectation value of the twist free energy density is, based on the equations of motion, constant along the chain. The space available to form thermal writhe in the plectoneme is in general not the same as for a straight chain under tension. And so we need to take the thermal writhe in the plectoneme explicitly into considerations. We now assign part of the total linking number to the tails and loop, from which follows a tension dependent expectation value of thermal writhe and twist density according to (7.5). The rest of the linking number has to be accounted for by the plectoneme. We use this difference as definition of its linking number. For a large part it is accounted for by the twist and the writhe of the zero temperature plectoneme, but some comes from the thermal writhe of the strands within the plectoneme. A problem is that writhe, as a local observable, is only defined with respect to a reference curve, which in our treatment thus far was the z-axis, not the writhing plectoneme. In appendix (C.1) it is shown that under reasonable assumptions the thermal writhe can be treated as an additive correction to the plectoneme writhe, where the thermal writhe is calculated as the thermal writhe of an undulating chain, with a finite linking number, confined in a straight channel. For the calculation of the relevant quantities for a torsionally constrained confined WLC we can fall back to Section 6.3.2. The two directions x, y in equation (6.74) are the radial and pitch directions of the plectoneme strands. We assume we can capture the physics of confinement of the plectoneme strands with that of a harmonic confined chain with the same standard deviations σ_r and σ_p . In other words: the transversal distribution is Gaussian enough. In that case are the confinement free energy, the contraction factor and thermal writhe density given by equation (6.75). After inclusion of the twist factor multiplying the fluctuation determinant we find to lowest order for the free energy of the plectoneme strands

$$\bar{f}_{\text{strand}} = \bar{f}_{\text{tw}}^{\text{str}} + \frac{3}{8} \left(\frac{1}{\lambda_r} + \frac{1}{\lambda_p} \right) \quad (7.11)$$

$$\text{with } \bar{f}_{\text{tw}}^{\text{str}} := 2\pi^2 P_c' \langle \text{tw}_{\text{str}}^2 \rangle = 2\pi^2 P_c^{\text{eff}}(\bar{\lambda}) \text{lk}_{\text{str}}^2, \quad (7.12)$$

where $P_c^{\text{eff}}()$ is the function of λ as given by equation (7.4) The relative extension of the chain is to the same order given by

$$\rho_{\text{pl}} = 1 - \frac{2B \text{lk}_{\text{str}}}{S} - \frac{1}{4} \left[\frac{\lambda_r}{P_b} + \frac{\lambda_p}{P_b} \right] + \frac{2\lambda_s B \pi P_c' \text{lk}_{\text{str}}}{S P_b^2} \quad (7.13)$$

It is important to stress that the confinement free energy is purely entropic: the contribution of the confining potential was subtracted from the full free energy. The confining channel in

the plectoneme is not straight and the r and p directions rotate around the channel axis. This does influence the writhe. The length scale of these is of the order of the pitch or, as argued above, of the standard deviation, in that channel direction. In all cases we consider, the radial standard deviation is considerably smaller than that in the pitch direction. As can be seen from the equations, the torsional deflection length ranges in that case from $\bar{\lambda} = 3\lambda_r/2$ for $\sigma_r = \sigma_p$, till $\bar{\lambda} \simeq 2\lambda_r$ for $\sigma_r \ll \sigma_p$. Since this is the length scale where confinement dominates thermal fluctuations, as long as it is much smaller than the pitch, the global writhing path is not affected by thermal fluctuations. The contraction ρ_{pl} does depend somewhat on fluctuations in the pitch direction and so its size does affect plectoneme formation to some extent. The free energy density of the plectoneme is the sum of this confinement-, the bending (7.10)- and electrostatic (7.9) free energy:

$$f_{\text{plect}} = f_{\text{bend}} + f_{\text{strand}} + f_{\text{el}} \quad (7.14)$$

The energy stored in the twist is expected to have a fast relaxation time, since twist hardly couples to the environment. Experiments confirm this [179]. Therefore the twist free energy density is equal in the tails and the plectoneme strand. Since the magnitude of the fluctuations is not necessarily the same, the expectation values of the twist will in general differ. Equating f_{tw}^{t} and $f_{\text{tw}}^{\text{str}}$ allows us to eliminate the linking density of the strands in the plectoneme as parameter and write $\text{lk}_{\text{str}} = \delta \text{lk}$, with

$$\delta = \sqrt{\frac{P_c^{\text{eff}}(\lambda)}{P_c^{\text{eff}}(\lambda_s)}} \quad (7.15)$$

close to one by assumption. This is indeed the case in all experimental conditions studied: For forces ranging from 0.5 pN to 4 pN, λ varies from 7 nm to 20 nm, leading to an effective torsional persistence length of $P_c^{\text{eff}}(\lambda) \simeq (0.8 - 0.93) P_c'$. On the other hand the radial standard deviation in the plectoneme is largely set by the Debye screening length. With monovalent salt concentrations in the range of 20 mM to 320 mM and assuming $\sigma_r \simeq \kappa^{-1}/2$ we can estimate the corresponding effective persistence length to be $P_c^{\text{eff}}(\lambda_s) \simeq (0.91 - 0.96) P_c'$, and so a crude estimate for δ is $1.01 \geq \delta \geq 0.91$. Although the difference in ‘thermal waste’ while transforming linking number into twist is rather small, it would be wrong to draw the conclusion that entropic effects can be neglected, since the entropic part of the free energy goes as $\simeq k_B T / \lambda$. The difference between the two states can be up to one $k_B T$ per nm.

It is worthwhile to split off the twist contribution to the free energies:

$$\left. \begin{matrix} f_{\text{tail}} \\ f_{\text{plect}} \end{matrix} \right\} = f_{\text{tw}} + \left\{ \begin{matrix} g_{\text{tail}} \\ g_{\text{plect}} \end{matrix} \right. \quad (7.16)$$

with:

$$g_{\text{tail}} = -f \left(1 + \frac{f - 4\pi B \text{lk}}{2S} \right) + \frac{1}{\lambda} \left(1 - \frac{\lambda}{4P_b} - \frac{\lambda^2}{64P_b^2} \right) \quad (7.17)$$

$$g_{\text{plect}} = \frac{3}{8} \left(\frac{1}{\lambda_r} + \frac{1}{\lambda_p} \right) + f_{\text{bend}} + f_{\text{el}} \quad (7.18)$$

the remaining free energy contributions. We will use $\Delta g = g_{\text{plect}} - g_{\text{tail}}$ to denote their difference. Once a plectoneme has formed the expectation value of its contour length follows from the combined linking numbers of plectoneme and end-loop, which should add to the linking number that was externally applied:

$$\text{Lk} = (L_c - L_p) \text{lk} + L_p [\rho_{\text{pl}} \omega + (1 - \epsilon) \text{lk}] + W_{\text{rloop}} \Rightarrow l_p := \frac{L_p}{L_c} = \frac{\nu - \text{lk} - W_{\text{rloop}} / L_c}{\rho_{\text{pl}} \omega - \epsilon \text{lk}}, \quad (7.19)$$

with $\nu := \text{Lk} / L_c$ the applied linking number density. The reduced free energy density of this one plectoneme configuration and its extension are:

$$\begin{aligned} f_1 &= (1 - l_p) f_{\text{tail}} + l_p f_{\text{plect}} \\ &= f_{\text{tw}} + g_{\text{tail}} + l_p \Delta g + \frac{\mathfrak{E}_{\text{loop}}(t)}{k_B T L_c} \end{aligned} \quad (7.20)$$

$$\frac{\Delta z}{L_c} = \rho_{\text{tail}} (1 - l_p) - \frac{L_{\text{loop}}}{L_c} \quad (7.21)$$

both depending on the 4 parameters $R(\text{or } t), \sigma_r, \alpha$ and lk . The calculation boils down to a 4 parameter minimization procedure. In the long chain limit with finite plectoneme length the loop contribution can be neglected in determining the 4 parameters. We can assume that ϵ is small compared to ω , under conditions where a plectoneme forms. We can also neglect the dependence of ρ_{pl} on the parameters, its variational contribution is on the order of $\lambda_{r,p} / P_b$, which is small by assumption. The long chain finite plectoneme free energy is:

$$f_1 = f_{\text{tw}}(\text{lk}) + g_{\text{tail}} + \frac{\nu - \text{lk}}{\rho_{\text{pl}} \omega(R, \alpha)} \Delta g(R, \alpha \sigma_r) \quad (7.22)$$

The linking number density and chain extension are readily obtained in this limit:

$$\text{lk} = \frac{\Delta g}{4\pi^2 P_c' \rho_{\text{pl}} \omega(R, \alpha)} \quad \frac{\Delta z}{L_c} = -\frac{\rho_{\text{tail}}}{\rho_{\text{pl}} \omega(R, \alpha)} \quad (7.23)$$

Minimizing the free energy is within this approximation equivalent to minimizing the linking number density. This is not really a surprise since plectoneme formation is driven by linking number. A numeric minimization gives results that compare in general well with experiments

only under limited conditions, namely the transition point, height of the jump at the transition as well as the slope after the transition are within experimental error for high enough forces and salt concentrations, see Figure 8.1. The lack of agreement clearly inversely correlates with K^2 . Dropping the assumption of equal linking number densities in tail and plectoneme hardly improves the results. Especially for low salt concentrations the agreement is good only for a small range of relatively high forces, even when the value of K^2 stays well above 3. This discrepancy, that is slightly stronger when fluctuations are neglected, has led to a variety of speculations: an effective charge reduction [150], partly introduced to explain torques measurements, and a charge correlation effect between the two intertwined super-helices that form the plectoneme [177]. The deviation of the experimental slopes from the calculated one goes hand in hand with the decrease of the height of the potential barrier between straight and plectoneme configuration. But our theory is not complete yet: the inclusion of other local minima next to these two configurations turns out to be of greater importance than has been acknowledged until now, as we will show in the next section.

7.2 Instantons

Contributions of local minima have to be taken separately into account in any perturbative calculation. A standard way to grasp their influence in statistical as well as quantum physics is through the concept of an instanton. Using the picture of a particle moving in an inverted potential, in our case the Kirchhoff analogy, the transition can be seen as a fast jump from one (local) minimum to another, fast since the particle in the inverted potential converts potential energy into kinetic energy during the tunneling through the barrier.

The usual way to take these local minima into account is to treat them as a gas of defects that compete with their entropic gain against the energetic advantage of the ground state. This is the situation that would exist in a torque regulated setup. In our case where the linking number is the control parameter the treatment changes essentially. A defect changes the linking number and so the energy of the configuration in which it is embedded. Furthermore the defects are themselves plectonemes and so to understand thermal fluctuation close to the transition we actually study multi-plectoneme configurations.

The entropic gain of a multi-plectoneme configuration is twofold: there is the usual combinatoric positional freedom of defect placement (the “gas of defects”), but there is also an increase in configurations due to the freedom in distributing the total plectoneme length over the individual plectonemes. Treating the plectonemes as having a hardcore repulsion, one finds for the density of states of a configuration with *total* plectoneme contour length L_p spread out over m plectonemes:

$$z_m = \frac{1}{\Lambda^{2m-1}} \frac{L_p^{m-1}(m)}{(m-1)!} \frac{(L_c - m L_{\text{loop}} - L_p(m))^m}{m!}, \quad (7.24)$$

with Λ a cutoff scale that we will take to be the helical repeat. This expression can be easily derived using Laplace transforms (see Appendix C.2). The result is essentially the product of the two contributions: the first fraction counts the possible ways to distribute the plectoneme length over the m plectonemes, while the second fraction counts the number of ways the gas of defects, in the guise of end-loops, can be partitioned over the free chain length. The choice of cutoff, is a choice of the unit we count in. The m dependent plectoneme length follows as before from the total linking number.:

$$L_p(m) = L_c \frac{\nu - \text{lk} - m \text{Wr}_{\text{loop}} / L_c}{\rho_{\text{pl}} \omega - \epsilon \text{lk}} \quad (7.25)$$

We cannot drop the loop contribution here since we should leave the possibility open that the number of plectonemes increases at the same (or higher) rate as the contour length. For the same reason we should also take the end-loop energy term into account. In principle also plectonemes with a negative writhe should be included. Their contribution is very small except when tension and linking number are low. We are mainly interested in linking numbers around and above the bifurcation point. In the following we will neglect them.

The maximum number of plectonemes can never be higher than L_c / L_{loop} and it is to be expected that finite size effects easily dominate the turn extension curves for shorter chains. We want to describe the generic behavior of the turn extension plot without end effects. The reason is not only to avoid plectoneme-plectoneme interactions, but also to avoid interactions of the magnetic/optical bead with the substrate and details of the exact geometry of attachment of the chain ends. It is sensible to work again in the large L_c limit, above the bifurcation point but with small enough linking number that the plectoneme density is low. These demands translate to $L_p > 0$ and $L_c \gg m L_{\text{loop}} + L_p$. Taking $\epsilon = 0$ and $\rho_{\text{pl}} = 1$ we write the free energy of the chain as:

$$\mathcal{F} = L_c f_0 + m \Delta = L_c \left(f_0 + \frac{\mu}{L_{\text{loop}}} \Delta \right) \quad \text{with } \Delta = \mathfrak{E}_{\text{loop}} - \frac{\text{Wr}_{\text{loop}} \Delta g}{\omega} \quad (7.26)$$

with f_0 collecting the terms of the free energy density, that do not depend on the *loop density* $\mu := m L_{\text{loop}} / L_c$. Since Δ is larger than zero iff the energetic cost per writhe of the loop is larger than that of the plectoneme, a negative delta results in a plectonemeless chain where the excess linking number is distributed over loops with writhe density $\omega_l := \frac{\text{Wr}_{\text{loop}}}{L_{\text{loop}}}$. Only entropic effects can change this. One caveat: close to the zero length plectoneme the lack of a proper electrostatic model for the endloop influences the free energy too much. This is not that serious when using plectoneme parameters in the long chain, finite plectoneme limit, but distorts the transition to some degree. To simplify the following discussion we will treat the cutoff and the loop length as being the same. The error amounts to logarithmic corrections that will have no influence on the conclusions we will draw. Comparing in the next chapter the model with experiments the change of cutoff has an effect smaller than the experimental error in all experiments we compared the model with. The loop density, μ , dependence of the

partition sum is now:

$$Z \sim \int_0^{\mu_m} d\mu \exp \left\{ \frac{L_c \mu}{L_{\text{loop}}} \left[\log \left(\frac{l_p(\mu)}{\mu} \frac{(1 - \mu - l_p(\mu))}{\mu} \right) + 2 - \Delta \right] \right\} \\ \simeq \int_0^{\mu_m} d\mu \exp \left\{ \frac{L_c \mu}{L_{\text{loop}}} \left[\log \left(\frac{l_p(\mu)}{\mu^2} \right) + 2 - \Delta \right] \right\}, \quad (7.27)$$

with μ_m the maximum density set by $\mu_m = \sup\{\mu \in [0, 1] | 0 \leq l_p(\mu) \leq 1 - \mu\}$. The extension of the chain can be seen as having two contributions: one from the plectoneme(s) and one from the loops:

$$\frac{z}{L_c} = 1 - l_p - \mu \quad (7.28)$$

It is straight forward to verify that the argument of the resulting exponent is a concave function of μ for $\mu \in (0, \mu_m)$ and so its dominant contribution comes from it's maximum:

$$\log \left(\frac{l_p(\langle \mu \rangle)}{\langle \mu \rangle^2} \right) - \frac{\langle \mu \rangle \frac{\omega_{\text{loop}}}{\omega}}{l_p(\langle \mu \rangle)} - \Delta = 0 \quad (7.29)$$

Since the two last terms are negative we should have $l_p(\langle \mu \rangle) > \langle \mu \rangle^2$. Single plectoneme behavior is to be expected when $l_p \simeq \frac{\nu - lk}{\omega}$. When this is the case:

$$\langle \mu \rangle \simeq \sqrt{\frac{\nu - lk}{\omega}} e^{-\Delta/2} \ll \frac{\nu - lk}{\omega_{\text{loop}}} \Rightarrow \frac{\nu - lk}{\omega} \gg \left(\frac{\omega_{\text{loop}}}{\omega} \right)^2 e^{-\Delta} =: \zeta \quad (7.30)$$

Of course multiple plectonemes do always appear for long enough chains. Their appearance normally does not change the slope of the turns extension plot in a measurable way. Once the nucleation of plectonemes dominates the slope we speak of a multi plectoneme phase. The right hand side of (7.30), the *multi plectoneme* (MP) factor, ζ , is an indicator for the multi plectoneme phase. We can distinguish 2 contributions that suppress multi-plectonemes: a large loop energy per gained writhe as compared to the plectoneme and a low writhe density in the loop, compared to the plectoneme. This last contribution is of purely entropic origin. The behavior of the multi-plectoneme factor is depicted in 7.1. The largest factor is at low salt and high tension. We can understand the curve by realizing that the plectoneme radius depends differently on force or salt concentration depending on their strength. The loop writhe density, which is on the order of $1/(4\lambda)$, is almost independent of the salt concentration, since the homoclinic parameter varies over a small range. At low salt ω is of the order κ . This is partly due to the electrostatics stabilizing the plectoneme opening angle to a value that is almost constant over a large range of conditions, while the plectoneme radius is to a large extend determined by the electrostatic interactions, resulting in a radius of the order of the Debye length. Since the writhe density of the plectoneme scales as $1/R$ we find $\omega \sim \kappa$. The

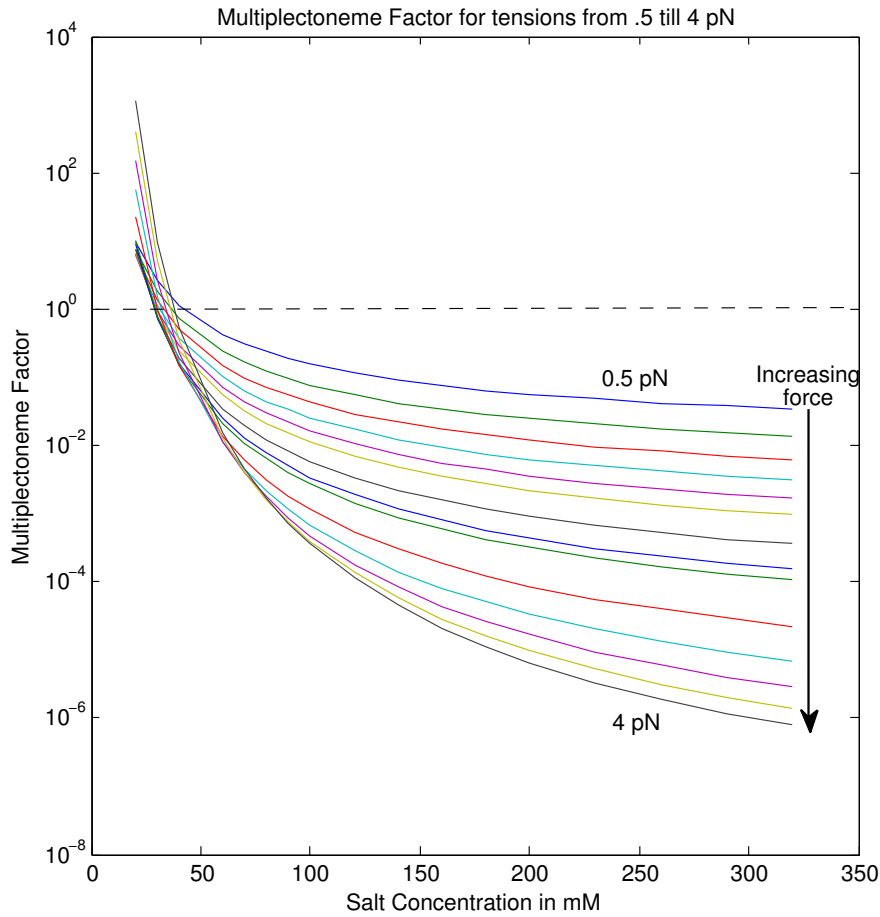


Figure 7.1: Multi-plectoneme factor

ratio $\omega_{\text{loop}} / \omega$ increases with decreasing salt concentration. Since the plectoneme free energy density at the same time increases while the loop energy stays roughly constant, Δ decreases and thus the MP factor increases. An increasing tension at a constant low salt concentration increases the pre-factor that scales as f / P_b . At the same time the loop energy increases as $\sqrt{f P_b}$ but the plectoneme contribution to Δ ($\Delta g / \omega$) increases almost linearly with f since R 's dependence on f is small.

This behavior changes at higher salt concentrations where it is the deflection length λ that sets the plectoneme radius resulting in an almost constant pre-factor and a Δ that increases as $\sim \sqrt{f P_b}$. This results in a decreasing MP factor with increasing tension.

A multi-plectoneme state corresponds to a linear dependence of $\mu \simeq \frac{\nu - 1}{\omega_l} k$. Since $\omega_{\text{loop}} < \omega$ we expect an increase of the slope due to multi-plectonemes. The slope naturally splits into a

one plectoneme contribution and an MP contribution as follows:

$$-\frac{\partial_v z}{L_c} = \frac{1}{\omega} + \partial_v \mu \left(1 - \frac{\omega_{\text{loop}}}{\omega} \right). \quad (7.31)$$

By lowering the salt concentration it is possible to arrive at a situation that the writhe density of the loop is larger than that of the plectoneme, while the plectoneme is still energetically favorable. An overall picture of the MP phase is clarified by the contour plot, Figure 7.2, of

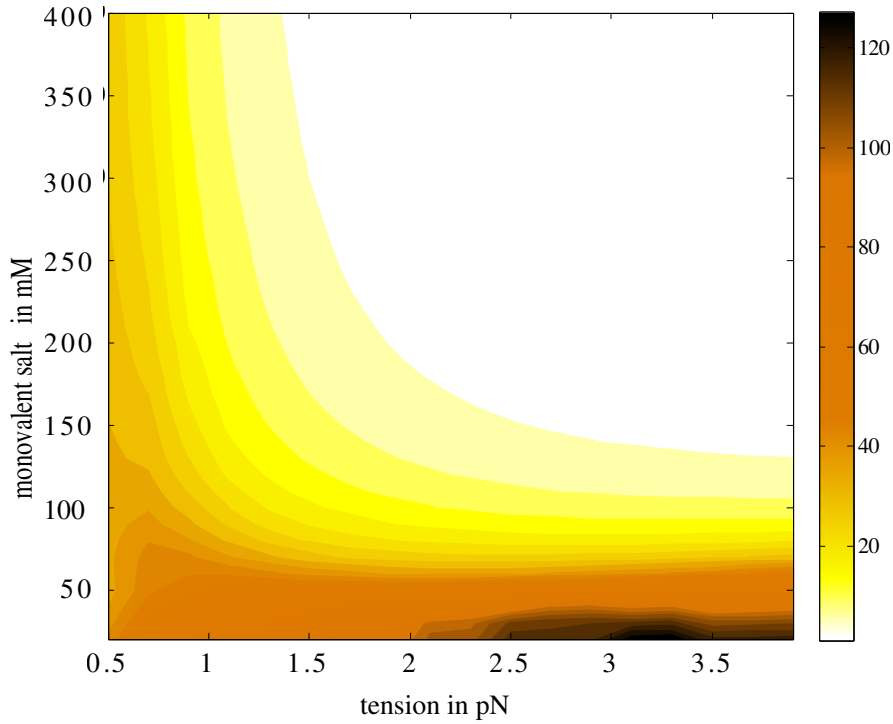


Figure 7.2: Contourplot of the number of plectonemes as function of salt concentration and tension for a 7.2 μm long chain

the number of plectonemes for a chain of 7.2 μm as it varies over a range of combinations of tension and salt concentration.

Comparison with experiments and conclusions

To test the validity of the model over an extensive range of parameters, use has been made of a series of measurements performed by the Seidel group in Dresden. For combinations of forces from 0.25 pN to 4 pN and salt concentrations from 20 mM to 320 mM the turns extension curves have been measured for chains of approximately 600 nm contourlength. The experimental data have been smoothed out with a moving average algorithm. To correct for the geometry of connection to the beads and substrate, the effective contour length of the chain has been obtained by fitting the 0 turns extension to the ideal not torsional restricted worm like chain. Up to lowest order this should be equivalent to the torsionally constrained 0 turns configuration. The effective chains thus obtained have a length that varies between 570 nm and 630 nm. A batch of measurements under varying forces, but constant salt concentration has been performed on one chain allowing us to verify that the effective chain length stays more or less constant once the geometry of the chain attachment is fixed. Only for forces below 1 pN the effective chain length decreases. This is partly due to the bend chain attachment, combined with too wildly fluctuating chains for our perturbative model.

The minimization procedure was initiated as follows: starting from the bifurcation point, lk_{cr} , the applied linking number per length was set to $\nu = lk_{cr} + 0.2$. The parameters of the model were set to $lk = 0.8 lk_{cr}$, $\alpha = 1$, $\sigma_r = 1/(2\kappa)$, and $R = 1/\kappa$. The free energy for a single chain was minimized after which the obtained values were used to set ν to $(\omega + lk_{str} + 2 lk_{cr})/2$, while keeping the other parameters unchanged. After this the minimization was repeated. In that way the applied linking number is approximately halfway in between the critical value and the maximal value. The reasoning is that with a linking number close to the bifurcation point the influence of an incomplete description of the end loop becomes too strong, while a linking number too far from the transition might underestimate the influence of multi plectoneme configurations. The precise value is not very important. Too close to the bifurcation point the chain collapses before the transition in low salt condition.

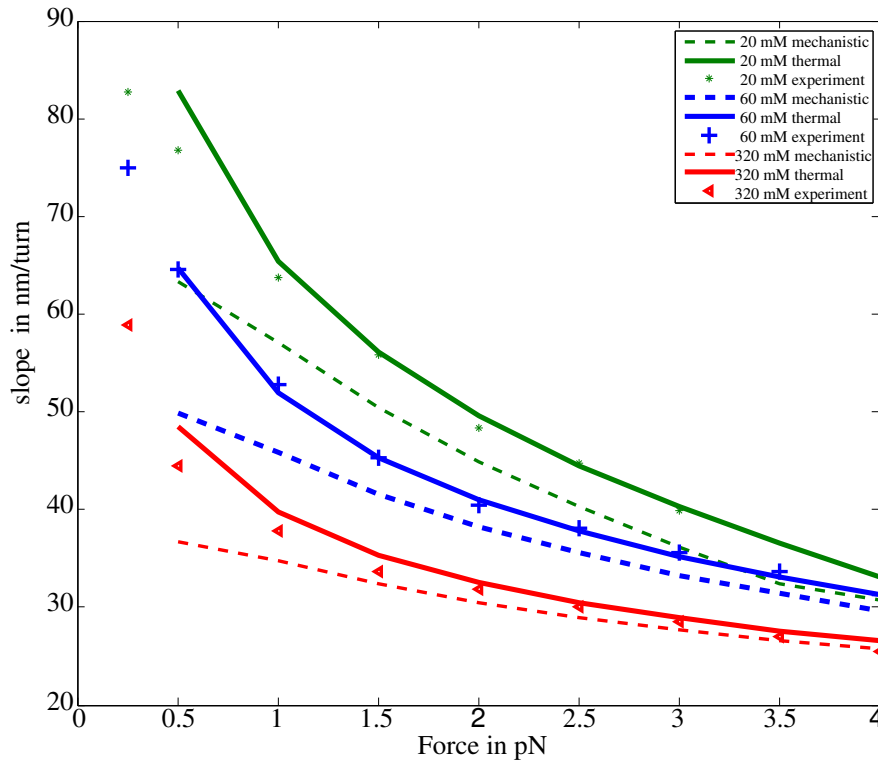


Figure 8.1: Slopes with and without thermal contributions. The dotted curves were calculated from the model up to Chapter 5, Equations eqs. (5.28) and (5.29). The solid thermal curves include multiplectonemes and were calculated using the method outlined in the text.

The reason is not so much the influence of the loop but a K^2 value that gets too low. Of course any prediction based on the model for K^2 values below 3 is unreliable. The generation of the force extension behavior is based on plectoneme energies from this minimization. The whole procedure is very fast.

As a first check of our model we compare predicted plectonemic slopes to those determined in experiments. Note that the choice of where to measure the slope is not always obvious in both theory and experiment. Whenever there was a clear constant slope visible it was taken as “the slope”, otherwise the first slope after the transition was taken. Especially for the short 600 nm chains it was not always clear what to take as slope. This is especially true for low salt, 20 mM to 60 mM, conditions. Nonetheless the slopes for the full range indicated a nice agreement between experiment and model. The results for 20, 60, and 320 mM are in Figure 8.1. The influence of the multi plectoneme phase is clearly visible for low salt concentrations. There is also a clear improvement in the low force range, although there the value of K^2 of around 2 at the transition makes the agreement mere coincidental. The turn-extension plot at 20 mM and 3 pN in Figure 8.2 shows the details. The transition happens in both cases at a lower linking number than in the experiment, presumably because it is

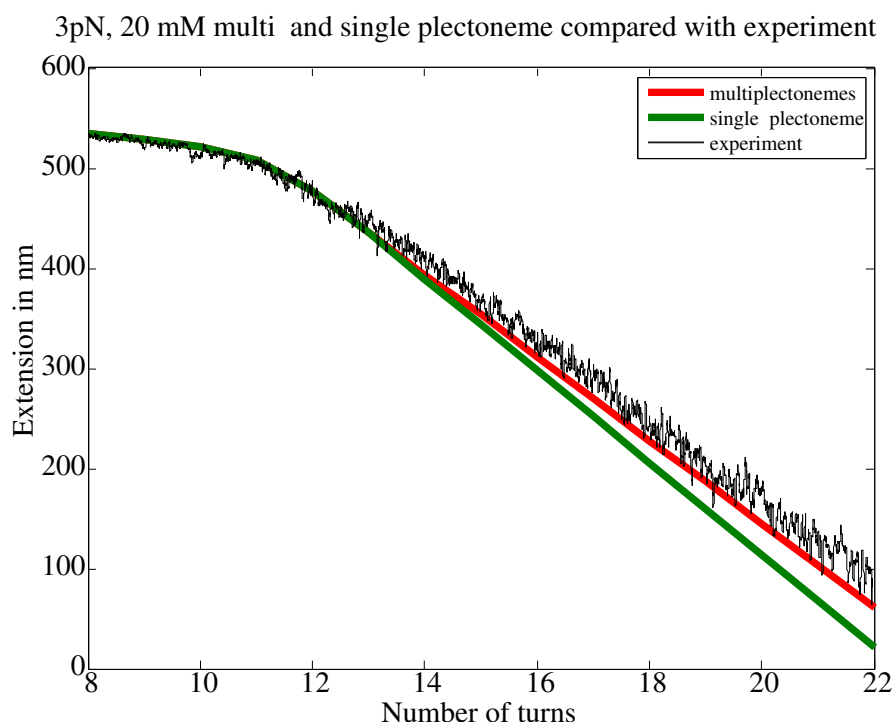


Figure 8.2: Influence of the multi-plectoneme phase on the turn extension slope. The black curve is a single plectoneme curve, the red curve when multiplectonemes are taken into consideration

too close to the bifurcation point. To produce the plots the torsional persistence length was lowered to 90 nm from 110 nm to 120 nm to get the transition point close to the experimental. In Figure 8.3 The number of plectonemes is set out against the number of turns for these conditions.

The curves for 20 mM and 320 mM are shown in Figure 8.4 and Figure 8.5. For most cases our model predicts the experimental curves extremely well. The 20 mM measurements show an exceptional behavior at 3.5 pN. It is possible that the chain undergoes a phase transition as has been suggested [150]. Another possibility is that because plectoneme formation is relatively expensive, starting plectonemes are extremely unstable. That can explain the sawtooth behavior with signs of attempts at plectoneme nucleation.

A set of experiments performed on a 3850 nm chain, in a 320 mM solution with the same setup shows a longer clear slope in Figure 8.6. The transition point suggests a 120 nm torsional persistence length.

Another test of the model is the analysis of the plectoneme torques. The torque can be easily obtained by dividing the increase of the free energy by the rotation angle that caused it. It is commonly believed that the linear slope of the curves coincides with a state of constant torque [180, 152]. This makes it attractive to use the DNA plectoneme as a source of constant torque in the study of molecules that interact with DNA like topoisomerase and helicase.

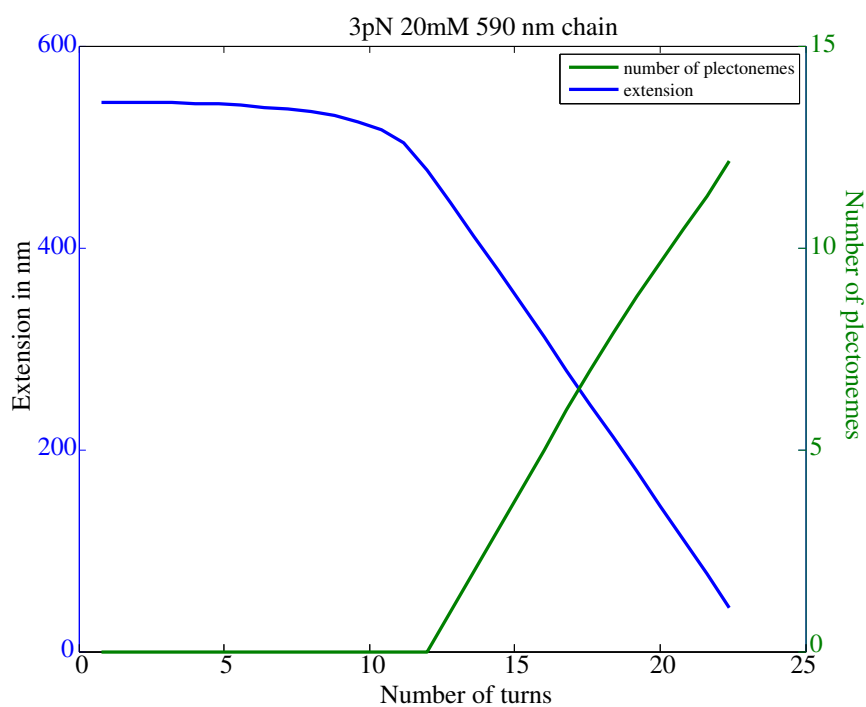


Figure 8.3: Number of plectonemes at 3 pN and 20 mM salt in green combined with the corresponding turns extension plot in blue

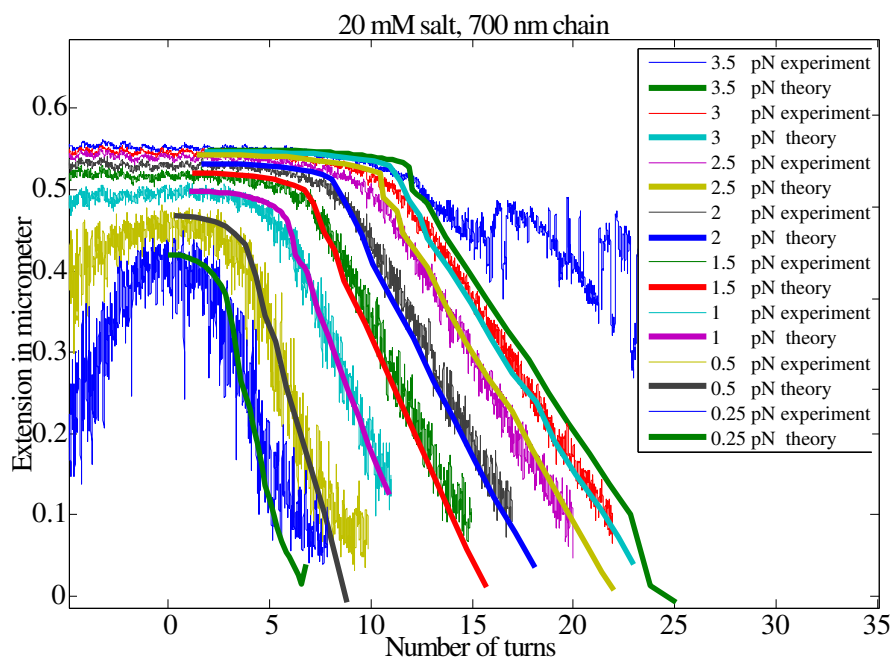


Figure 8.4: Turns versus extension plots for 20 mM salt concentrations. P_c was set to 90 nm to get a good agreement, but as explained in the text it might be a calculational artifact

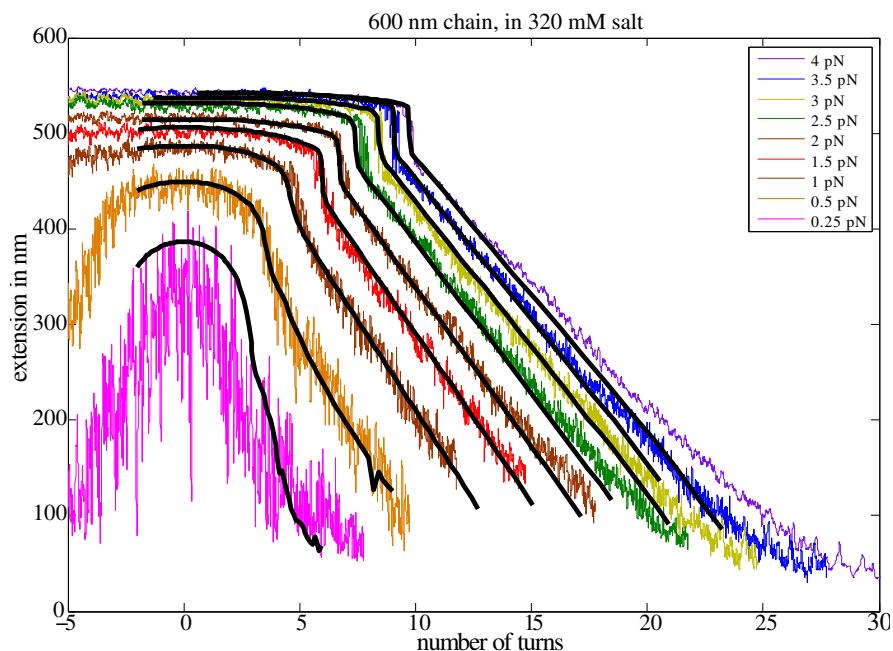


Figure 8.5: Turns versus extension plots for a 600 nm chain under varying tension in 320 mM salt. $P_c = 120$ nm

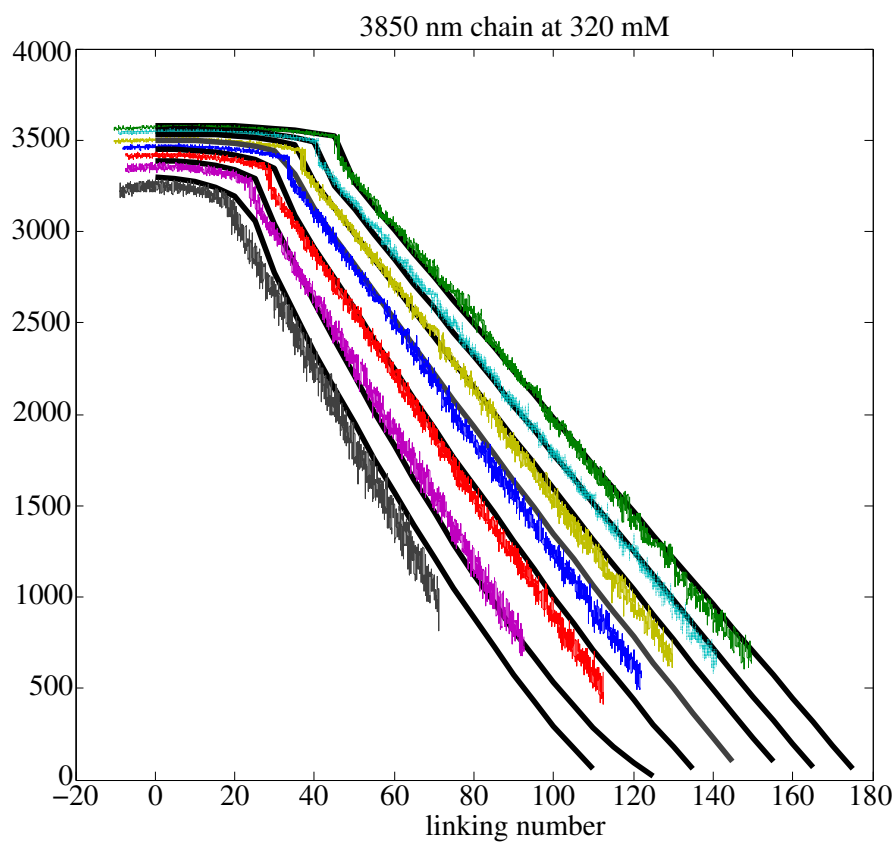


Figure 8.6: Turns versus extension plots for a chain of 3540 nm with tension from 1 pN to 4 pN in 320 mM salt. A torsional persistence length of 120 nm was used.

Table 8.1: Indirect torque measurements using Maxwell relations [147] compared to the theoretical values from our model

Salt (mM)	Force (pN)	Exp. Torque (pN nm)	Theor. Torque (pN nm)
10	2.86	28.1	35
	2.53	26.2	32
50	3.66	29.6	34.7
	3.23	27.4	32.4
100	3.33	24.4	30.1
	2.61	20.7	26.3
500	4.33	22.3	29.6
	3.80	20.2	27.5

One way to measure this plectoneme torque is by using a specially nanofabricated quartz cylinder in conjunction with an optical tweezer [181]. The setup seems to be very promising enabling the measurement of torque at the same time as force and extension. A small set of measurements was used with relatively short chains of 700 nm [145]. Another method makes use of the constant torque in the plectoneme region combined with Maxwell relations between torque/linking number and force/extension as free energy parameters to calculate the plectoneme torque over a large range of forces based on an approximately linear linking number torque relation before the transition at a force in the upper range. Making use of the assumption of a constant torque after plectoneme formation, the torque for a large range of data can be calculated just from the turn extension plot. This is the setup from Mosconi et al. [147]. The resulting torques in the measurements [145, 147] seem to differ. One suggestion is that the salt concentrations perhaps differ too much. It is interesting to compare the torques

our model predicts with those of reference [147]. To our surprise the torques we calculate differ from their measurements substantially enough to doubt the validity of our model, see Table 8.1. This was perhaps somehow to be expected, since the torque data were the main driving force for Maffeo et al [150] to incorporate a charge reduction factor into their model. What is somewhat mysterious is that the force extension curves themselves are in good agreement with our model. If the torque only depends on the shape of that curve, it must be that there is somewhere a wrong assumption made.

Comparing our torque predictions with the direct torque measurements from the older optical tweezer measurements [145] reveal however a remarkable good agreement as is shown in Figure 8.7, where the torques are shown as a function of the supercoiling density defined as the ratio of the linking number density to the linking number density of the two strands of the

double helix when the chain is straight and relaxed. This last density is of course $1/\text{helical repeat} = 1/3.6 \text{ nm}^{-1}$.

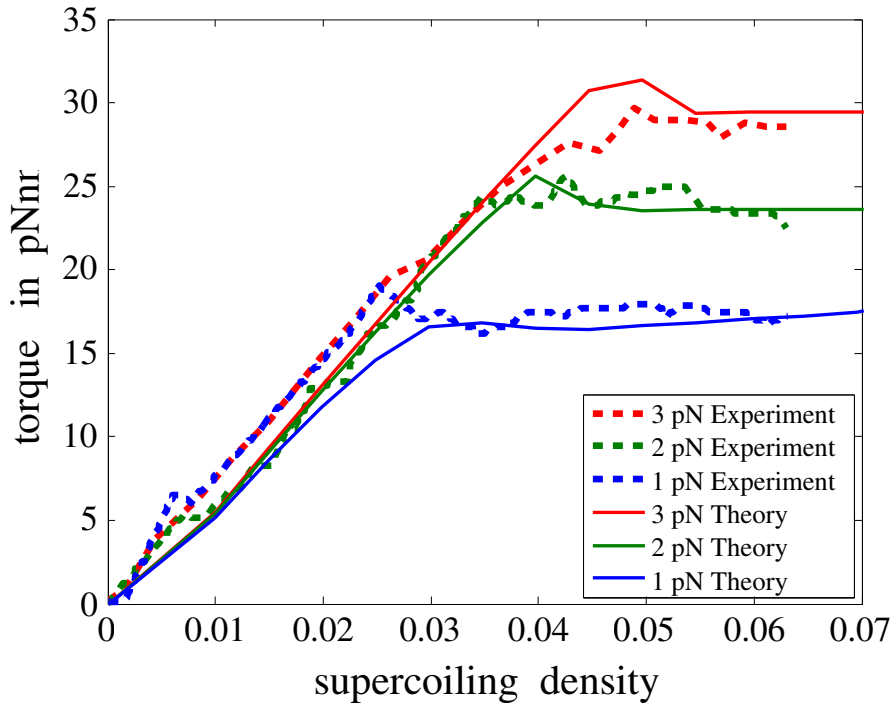


Figure 8.7: Comparison between experimental results from an optical tweezer experiment using a quartz cylinder to directly measure the torque [145] and our theoretical model. The DNA has a contourlength of 725 nm, monovalent salt concentration 150 mM

The culprit is readily revealed as the multiplectoneme phase. In extracting the torque from the force extension measurements an essential assumption is that the torque in the linear slope is indeed constant. That almost presupposes that the slope is a one plectoneme slope. Lacking a method to verify this assumption it had to be accepted on face value. In reality the torque is not constant at all for lower forces. Thanks to the fast increasing number of plectonemes along the chain the torque is almost linearly *increasing* spoiling the calculations. When we take this increase into account, the resulting torque values agree again wonderfully well with the predictions from our model.

As an example we borrow the calculations from Mosconi et al. [182]. The relevant curves are in Figure 8.8. The Maxwell relation calculations are performed over the path as shown in the figure on the left. The resulting torque for 3.67 pN is 27 pN nm. But if we examine the torque as calculated from the model the result is higher, around 34.9 pN nm. Though the torque is constant for the high-tension slope, the path from B to C in Figure 8.8 is one of decreasing torque thereby resulting in a too low estimate for the plectoneme torque.

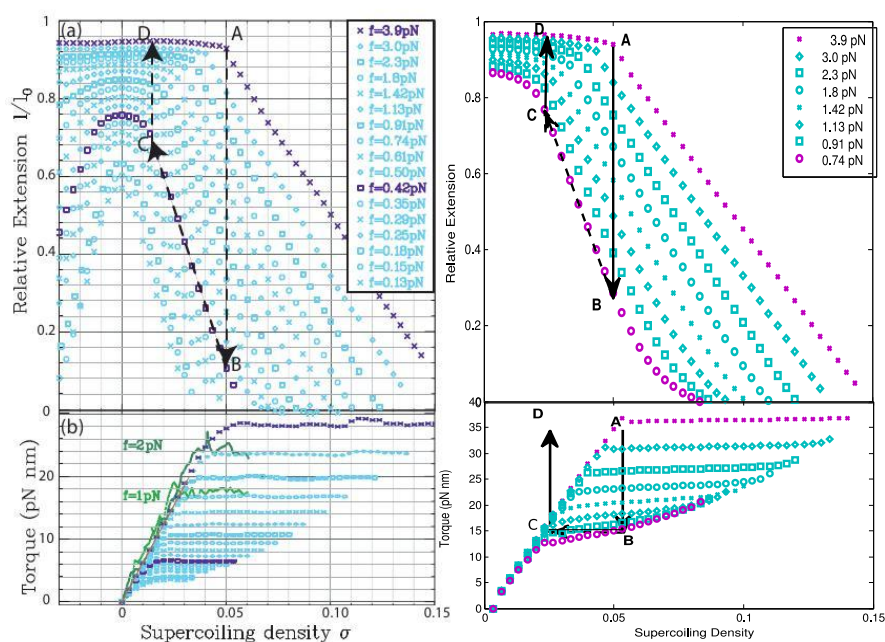


Figure 8.8: Magnetic tweezer measurements from Mosconi et al [182] as basis for indirect torque measurements. On the left are data from the actual measurements, the torques were determined assuming them to be constant. On the right the data as calculated from the theory for tensions where fluctuations are small enough using the criterium $K^2 \leq 3$. The contourlength is 5.6 μm , monovalent salt concentration of 100 mM

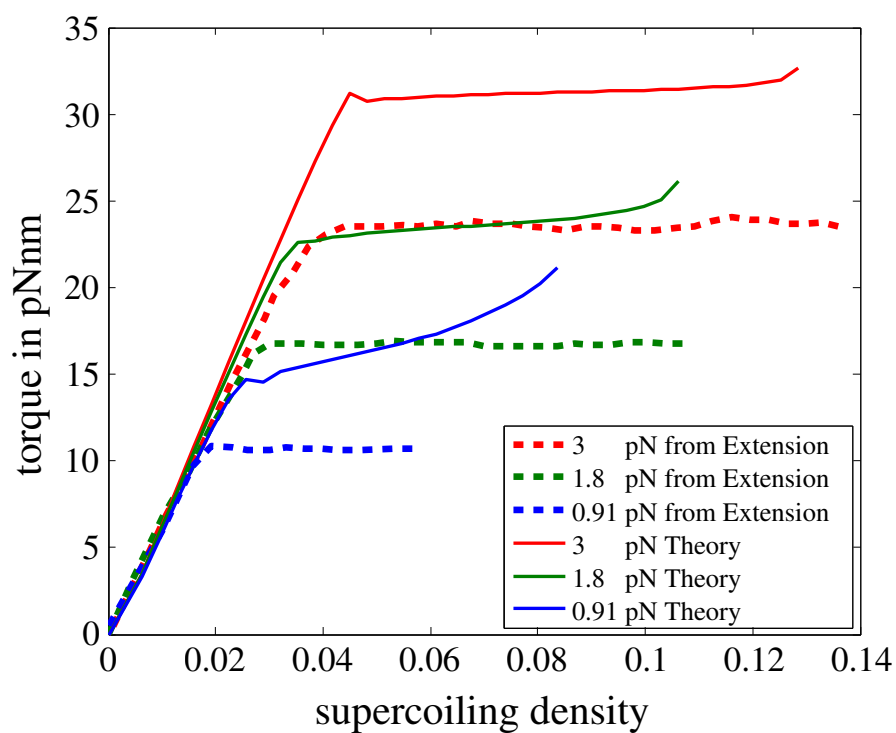


Figure 8.9: Torque as function of supercoiling density for three different tensions calculated from the model compared to the indirect determination of the torque using Maxwell relations under constant plectoneme torque assumption [182]. The conditions are the same as in Figure 8.8

8.1 Conclusions

Plectoneme formation in DNA can be thought of as a tool to study short distance interactions between DNA molecules in a reasonably controlled way. It seems to be important to acquire a good understanding of all the facets of the possible interactions. It was my intention to partly open the way to a detailed description of the mechanical, electrostatic and thermal forces that act on DNA in the cell. There are still many open questions of which I would like to mention a few:

- How is thermal writhe influenced by a writhing groundstate? The separation of the thermal writhe from its writhing background in the plectoneme as done in Appendix C.1 is a rough approximation, what are the effects of co- or anti-writhing paths?
- Is it possible get insight into possible charge correlations that might be important for homological recombination ?
- Do van der Waals forces play any role in DNA-DNA interactions in the cell ?
- Is the instability at low salt and high tensile forces a sign of a transition to PDNA, or is it a plectoneme nucleation problem ?
- What is the dependence of moduli other than the persistence length on the salt concentration?
- Does a crowded environment allow for larger torques ?

Elliptic functions and the generalized Lamé equation

A.1 Elliptic functions

The elliptic integrals and the Jacobi elliptic functions are functions of two variables and in the case of elliptic integrals of the third kind of three. There are different equivalent choices of pairs and the choice generally depends on the situation at hand. See also [120, 122].

Throughout Chapter 3 we use the Jacobi form (with one exception). In that form the variables are called the *argument*, x , and the *parameter*, $m \in [0, 1]$. In the literature the latter is sometimes replaced by the *modulus*, $k = \sqrt{m}$. The two variables are separated by a vertical line like in $E(x|m)$. An alternative form is the trigonometric form where the variables are the Jacobi *amplitude*, $\phi = \text{am}(x|m)$ and the *modulus* α defined through $\sin^2(\alpha) := m$. In that case the variables are separated by a backslash. So in the notation that we use we have the elliptic integrals of the first, second and third form written as:

$$F(\phi|m) = F(\phi \backslash \alpha) \quad E(x|m) = E(\phi \backslash \alpha) \quad \Pi(n; x|m) = \Pi(n; \phi \backslash \alpha) \quad (\text{A.1})$$

The integral of the first kind is an exception since it is in fact the inverse of the amplitude function and so $F(x|m)$ is identical to x . The complete integral of the first kind is defined as the value of F evaluated at an amplitude of $\pi/2$: $K(m) := F(\pi/2|m)$. The same holds for the other complete integrals, but now we can make use of the fact that $\text{am}^{-1}(\pi/2|m) = K(m)$ and so:

$$E(m) := E(K(m)|m) \quad \Pi(n|m) := \Pi(n; K(m)|m) \quad (\text{A.2})$$

The double periodic Jacobian elliptic functions are defined as:

$$\operatorname{sn}(x|m) := \sin(\operatorname{am}(x|m)) \quad \operatorname{cn}(x|m) := \cos(\operatorname{am}(x|m)) \quad \operatorname{dn}(x|m) := \frac{d}{dx} \operatorname{am}(x|m) \quad (\text{A.3})$$

A.2 Solving the generalized Lamé equation

The derivation is based on a similar derivation in [125]. We are looking for a solution of the generalized Lamé equation:

$$\ddot{y} + p(x)y = 0 \quad (\text{A.4})$$

where $p(x) = 1 + 4m - \epsilon - 6m \operatorname{sn}^2(x)$. We are especially interested in the small ϵ limit. The product $M(x) = y_1(x)y_2(x)$ of two solutions satisfies the third order differential equation:

$$\ddot{M} + 4p\dot{M} + 2\dot{p}M = 0 \quad (\text{A.5})$$

We will now construct a solution of this last equation as a series in $\operatorname{sn}(x)$. Write $M = \sum_{n \geq 0} a_n \operatorname{sn}^n(x)$. Substitution leads to the following relation between the coefficients:

$$a_n m(n^3 + 3n^2 - 22n - 24) + a_{n+2}(4(1 + 4m - \epsilon)(n + 2) - (n + 2)^3(1 + m)) + a_{n+4}(n + 4)(n + 3)(n + 2) = 0 \quad (\text{A.6})$$

To get a finite number of terms, the highest power has to be 4 and we find as solution:

$$M(x) = 9m^2 \operatorname{sn}^4(x) - 3m(3 + \epsilon) \operatorname{sn}^2(x) + 3\epsilon(1 - m) + \epsilon^2 \quad (\text{A.7})$$

Suppose $y_1(x)$ is one of the 2 solutions of (A.4) that make up M . We can use the D'Alembert construction to get another independent solution so that y_2 can be written as (the Wronskian is constant):

$$y_2(x) = By_1(x) + Cy_1(x) \int_0^x dx' \frac{1}{y_1^2(x')} \quad (\text{A.8})$$

Using the definition of $M(x)$, and assuming $M(x)$ to be positive, we can express $y(x)$ in terms of $M(x)$ as:

$$y = \sqrt{M(x)} \exp \left\{ - \int_0^x dx' \frac{C(m)}{2M(x')} \right\} \quad (\text{A.9})$$

Inserting this function into the Lamé equation results in:

$$2M(x)\ddot{M}(x) - \dot{M}^2(x) + C^2 + 4(1 + 4m - \epsilon - 6m \operatorname{sn}^2(x|m))M^2(x) = 0 \quad (\text{A.10})$$

and the $C(m)$ is found by inserting the solution for $M(x)$ (A.7):

$$C(m) = \pm 2\sqrt{\epsilon(3m(3+\epsilon) - \epsilon(1+4m-\epsilon)(3(1-m)+\epsilon))(3(1-m)+\epsilon)} \quad (\text{A.11})$$

$$\cong \pm 6\sqrt{\epsilon}\sqrt{3m(1-m)} \quad (\text{A.12})$$

The integrand in the exponential of (A.9) has poles at

$$p_{\pm} := \frac{3+\epsilon \pm \sqrt{9-6\epsilon(1-2m)-3\epsilon^2}}{6m} \cong \frac{3+\epsilon \pm (3-\epsilon(1-2m))}{6m}$$

Since $\text{sn}^2(x) \in [0, 1]$, by choosing $\epsilon < 0$ we can force the integrand to be regular for the parameter $m \in [0, 1]$. $C(m)$ on the other hand is now imaginary, so that we have to look at linear combinations of the two solutions for a real valued solution of the homogeneous equation. Noting that $M(x)$ is now strictly negative we find as the solution with the proper boundary conditions:

$$y(x) = \frac{2\sqrt{-M(0)}}{G(m)|C(m)|} \sqrt{-M(x)} \sin\left(\frac{-|C(m)|}{2} \int_0^x \frac{dx'}{M(x')}\right) \quad (\text{A.13})$$

We will now evaluate the integral appearing in the sinus:

$$\begin{aligned} \int_0^x \frac{dx'}{M(x')} &= \frac{-1}{9m^2(p_+ - p_-)p_+} \int_0^x \frac{dx'}{1 - 1/p_+ \text{sn}^2(x'|m)} \\ &\quad + \frac{1}{9m^2(p_+ - p_-)p_-} \int_0^x \frac{dx'}{1 - 1/p_- \text{sn}^2(x'|m)} \\ &= \frac{-1}{9m^2(p_+ - p_-)p_+} \Pi(1/p_+; x|m) + \frac{1}{9m^2(p_+ - p_-)p_-} \Pi(1/p_-; x|m) \end{aligned} \quad (\text{A.14})$$

The elliptic integral of the third kind, $\Pi(n; x|m)$, has a behavior that depends on the value of the characteristic n [120]. In our case we have characteristics $1/p_+ \cong m(1-\epsilon m/3) \in (m, 1)$ and $1/p_- \cong 3m/(\epsilon(1-m)) < 0$ both corresponding to so called circular cases.

The functional determinant is then given by:

$$\begin{aligned} D_{\theta}^{\epsilon} &= y(2K(m)) \\ &= \frac{-M(0)}{K(m)|C(m)|} \sin\left(\frac{|C(m)|}{9m^2(p_+ - p_-)} \left[\frac{1}{p_+} \Pi(1/p_+|m) - \frac{1}{p_-} \Pi(1/p_-|m) \right]\right) \end{aligned} \quad (\text{A.15})$$

where we introduced the complete elliptic integral of the third kind, defined as usual from the incomplete one:

$$\Pi(n|m) := \Pi(n; K(m)|m) = \frac{1}{2} \Pi(n; 2K(m)|m) \quad (\text{A.16})$$

The integral with the $1/p_+$ characteristic can be easily evaluated by expanding around characteristic m , leading to:

$$\Pi(1/p_+|m) = \int_0^{K(m)} \frac{dx}{\text{dn}^2(x|m)} + \mathcal{O}(\epsilon) \cong \frac{1}{1-m} E(m) \quad (\text{A.17})$$

Note that we only need to go up to first order in ϵ and the factor multiplying the sinus in equation (A.15) goes as $M(0) \sim \epsilon$.

The integral with the negative characteristic can be written as an elliptic integral with positive characteristic using the following definition [120]:

$$N_- := \frac{1 - p_- m}{1 - p_-} \cong 1 + \epsilon \frac{(1 - m)^2}{3m} \quad (\text{A.18})$$

resulting in:

$$\begin{aligned} \Pi(1/p_-|m) &= \frac{-p_-(1-m)}{(1-p_-)(1-mp_-)} \Pi(N_-|m) - \frac{p_-m}{1-p_-m} K(m) \\ &\cong -p_-(1-m) \Pi(N_-|m) - p_-m K(m) \end{aligned} \quad (\text{A.19})$$

The characteristic N_- is less trivial, since we can't expand around characteristic 1, where the elliptic integral diverges. We can express the integral in terms of yet another elliptic function, Heuman's Lambda function $\Lambda_0(z|m)$, as:[120]

$$\Pi(N_-|m) = K(m) + \frac{1}{2} \pi \delta [1 - \Lambda_0(z|m)] \quad (\text{A.20})$$

where

$$\begin{aligned} \delta &= \sqrt{\frac{N}{(1-N)(N-m)}} = \frac{1}{\sqrt{-\epsilon}} \left(\sqrt{\frac{3m}{(1-m)^3}} + \mathcal{O}(\epsilon) \right) \\ z &= \text{sn}^{-1} \left(\sqrt{\frac{1-N}{1-m}} \right) = \sqrt{-\epsilon} \left(\sqrt{\frac{(1-m)}{3m}} + \mathcal{O}(\epsilon) \right) \end{aligned} \quad (\text{A.21})$$

The Lambda function can be expressed, again following reference [120], in other elliptic functions as:

$$\Lambda_0(z|m) = \frac{2}{\pi} (K(m) E(z|1-m) - (K(m) - E(m)) F(am(z)|1-m)) \quad (\text{A.22})$$

Using the small argument expansion of the elliptic integrals: $E(z|1-m) \cong z$ we find :

$$\Pi(N_-|m) = K(m) - \frac{1}{1-m} E(m) + \frac{\pi}{2(1-m)\sqrt{-\epsilon}} \sqrt{\frac{3m}{1-m}} + \mathcal{O}(\sqrt{-\epsilon}) \quad (\text{A.23})$$

Finally we find for the functional determinant:

$$\begin{aligned} D_\theta^\epsilon &\cong -\frac{3\epsilon(1-m)}{K(m)|C(m)|} \sin \left(\frac{|C(m)|}{9m(1-m)} [K(m)(1-m) - (1-2m)E(m)] + \pi \right) \\ &\cong \frac{\epsilon}{K(m)3m} [K(m)(1-m) - (1-2m)E(m)] \end{aligned} \quad (\text{A.24})$$

which is equation (3.50).

Appendix B

Writhe of a plectoneme

In principle the writhe of the plectoneme can be calculated using Fuller's equation and continuity. Care should be taken since the plectoneme moves through a curve with anti-aligned tangent once every full turn of the plectoneme, when one considers the (un)winding as the homotopy to the straight line. Since we intend to use an exact expression for the writhe at least for the groundstate it is instructive first to calculate the writhe density for the plectoneme using Fuller's equation with respect to the plectoneme-axis for both strands, forgetting loop and tail

$$\begin{aligned}\omega_1(s) &= \frac{1}{2\pi} \frac{\cos(\alpha)(\sin(\alpha) - 1)}{R(t)} & s \in [0, l_p/2] \\ \omega_2(s) &= \frac{1}{2\pi} \frac{\cos(\alpha)(\sin(\alpha) + 1)}{R(t)} & s \in [l_p/2 + l_l, l_p + l_l].\end{aligned}\quad (\text{B.1})$$

We could in a hand waving fashion define an “average” writhe density as

$$\omega(\alpha, t) \stackrel{?}{=} \frac{1}{2}(\omega_1(s) + \omega_2(l_p + l_l - s)) = \frac{\cos(\alpha) \sin(\alpha)}{2\pi R(t)} \quad (\text{B.2})$$

The problem is that this definition, giving the usual relation, is based on Fuller's equation with respect to another axis than we started with, and we have not taken the writhe of the end loop into account

A correct way that shows the importance of the rotation of the closing loop is to use also here the z -axis as reference. Opposing points on the plectoneme strands have in this case the same writhe:

$$\omega_b(s) = \omega_b(l_p + l_l - s) = \frac{1}{2\pi} \frac{\sin \alpha \cos \alpha}{R(t)} \left[1 - \frac{1}{1 + \cos \alpha \cos \left((s_0 + s) \frac{\cos \alpha}{R(t)} \right)} \right] \quad (\text{B.3})$$

A surprising s dependence enters the writhe density of the plectoneme, the subscript b is as a reminder that this is a bare writhe density that does not include interactions with the rest of the chain. Adding plectoneme length also changes the writhe of the closing loop though. The closing loop is described at the onset of formation of the plectoneme by some space curve $\mathbf{r}_0(u) = (r_x(u), r_y(u), r_z(u))$, $u \in [0, l_l]$, with boundary conditions: $\mathbf{r}_0(0) = \mathbf{r}_p(0)$ and $\mathbf{r}_0(l_l) = \mathbf{r}_p(l_l)$. We furthermore assume the connection between the plectoneme and the end loop to be smooth, making the tangent well defined at the boundaries. The increase of the plectoneme by an amount of contour length $2s$ causes the end loop to rotate around the x -axis by an angle $\phi(s) = s \cos \alpha / R(t)$

$$\mathbf{r}_s(u) = \hat{O}_x(\phi(s))\mathbf{r}_0(u) = \begin{pmatrix} r_x(u) \\ \cos \phi(s)r_y(u) + \sin \phi(s)r_z(u) \\ -\sin \phi(s)r_y(u) + \cos \phi(s)r_z(u) \end{pmatrix} \quad (\text{B.4})$$

This rotation induces an s dependent change in the writhe of the loop to:

$$\text{Wr}_{\text{loop}}^1(s) = \frac{1}{2\pi} \int_0^{l_l} du \left(\frac{\cos \phi(s)(t_x(u)\dot{t}_y(u) - \dot{t}_x(u)t_y(u))}{1 - \sin \phi(s)t_y(u) + \cos \phi(s)t_z(u)} - \frac{\sin \phi(s)(t_z(u)\dot{t}_x(u) - \dot{t}_z(u)t_x(u))}{1 - \sin \phi(s)t_y(u) + \cos \phi(s)t_z(u)} \right). \quad (\text{B.5})$$

The superscript is just a reminder that it is not the writhe of the full homoclinic solution, but just of that part that detaches to function as end loop for the plectoneme. Note that this writhe is not necessarily well defined. In fact since the length of the loop is finite, its x -component is bounded and thus has at least one point where the tangent lies in a plane perpendicular to the x -axis. This tangent will be once every full turn of the plectoneme antipodal to the z -axis and thus invalidates Fuller's equation.

We can nonetheless calculate the differential change of this writhe per plectoneme contour:

$$\frac{d \text{Wr}_{\text{loop}}^1}{ds} = \frac{\cos \alpha}{2\pi R(t)} \int_0^{l_l} du \frac{-\dot{t}_x(u) - \sin \left(s \frac{\cos \alpha}{R(t)} \right) (t_x(u)\dot{t}_y(u) - \dot{t}_x(u)t_y(u))}{\left(1 - \sin \left(s \frac{\cos \alpha}{R(t)} \right) t_y(u) + \cos \left(s \frac{\cos \alpha}{R(t)} \right) t_z(u) \right)^2} \quad (\text{B.6})$$

$$- \frac{\cos \left(s \frac{\cos \alpha}{R(t)} \right) (t_z(u)\dot{t}_x(u) - \dot{t}_z(u)t_x(u))}{\left(1 - \sin \left(s \frac{\cos \alpha}{R(t)} \right) t_y(u) + \cos \left(s \frac{\cos \alpha}{R(t)} \right) t_z(u) \right)^2} \\ = \frac{\cos \alpha}{\pi R(t)} \frac{t_x(0)}{1 - \sin \left(s \frac{\cos \alpha}{R(t)} \right) t_y(0) + \cos \left(s \frac{\cos \alpha}{R(t)} \right) t_z(0)}, \quad (\text{B.7})$$

where use has been made of the unimodularity of the tangent vector and its symmetry: $t_x(0) = -t_x(l_l)$, $t_{y,z}(0) = t_{y,z}(l_l)$. Making use of the boundary conditions we finally find

$$\frac{d \text{Wr}_{\text{loop}}^1}{ds} = \frac{\cos \alpha \sin \alpha}{\pi R(t)} \frac{1}{1 + \cos \alpha \cos \left((s_0 + s) \frac{\cos \alpha}{R(t)} \right)} \quad (\text{B.8})$$

By adding this differential writhe density to the “bare” writhe density of the plectoneme (equation (B.3))(half of it to each strand) we recover the standard writhe density of a plectoneme (5.22), but now with the added bonus that the remaining writhe of the closing loop is independent of the length of the plectoneme. Since it is only in the end loop that antipodal points appear along the homotopy, defined by the explicit formation of the plectoneme, we can state that in this sense the writhe is additive:

$$\text{Wr}(t, \alpha) = \text{Wr}_{\text{loop}}(t) + L_p \omega(t, \alpha), \quad (\text{B.9})$$

with Wr_{loop} and ω given by equation (5.14) and (5.22).

Note that we used implicitly continuity to recover the full writhe of the chain by adding the differential writhe change of the end loop. In hindsight it is clear that the endloop should be included in the final result. Imagine for example a larger endloop such that the helices do not intertwine. All local writhe calculations considering the helix only would not depend on the intertwining at all! But the writhe of the latter can be calculated immediately without any continuity argument and it is easy to show from (B.3) that applying Fuller’s equation to a chain with a plectoneme of n turns ($l_p = 4n\pi R(t)/\cos \alpha$) gives a writhe of $\text{Wr} - 2n$.

Thermal fluctuations and plectonemes

C.1 Fluctuations of the strands in a plectoneme

Our treatment of thermal fluctuations in the plectoneme follows largely the work by Ubbink and Odijk [153], with some catch forced upon us by the physical conditions. In our case we can not just use Burkhardts result of the confinement of a rotational relaxed chain, but have to take the twist along the chain into account. This has two implications: 1. The confinement free energy gets twist dependent corrections, the calculation of which are of more general importance and are detailed in Chapter 6. 2. The confinement gives a relation between linking number and twist that depends on the confinement channel width. This is used to calculate the contour length of the plectoneme in the text.

In this appendix we will discuss how the fluctuations can be separated from the average plectoneme path. Thermal undulations effectively shorten the chain within its superhelical path. This has implications on the bending energy and the writhe density of the plectoneme. To calculate the effect we attach to each point along the non undulating path, the 0-path, or 0-chain, a triad, consisting of the tangent at that point and two normals. The fluctuations we can express in deviations in the two normal directions from the 0-path. The deviations in the tangential direction follow from the in-extensibility, or if needed a finite stretch modulus can be included [173]. For the plectoneme as triad we take its Fresnet basis, where the normal is the direction of curvature, which is the radial direction, making the “pitch-direction” the binormal. In contour length, the point along the 0-path gets shifted by a shortening factor ρ , for which we will use its expectation value. The deflection length in a confined channel is considerably shorter than the persistence length of the chain. In general one can expect, in conditions that allow for a perturbative expansion, that the length scales of the fluctuations are small compared to the global lengthscales. The main assumption in the following is: the wavelength of thermal undulation is considerably shorter than those of the writhing 0 path. More precisely the curvature and Fresnet torsion, which is 2π times the writhe density of the plectoneme, are small compared to the wavenumbers of thermal undulations. Neglecting

contributions from the 0-path torsion and curvature we arrive at the following equations:

$$\begin{aligned} \mathbf{r}(s) &:= \mathbf{r}_0(\rho s) + u_i(s) \mathbf{t}_{\perp,0}^i(\rho s) &\Rightarrow \quad \mathbf{t}(s) &\simeq \rho \mathbf{t}_0(\rho s) + \dot{u}_i(s) \mathbf{t}_{\perp,0}^i(\rho s) &\Rightarrow \\ \dot{\mathbf{t}}(s) &\simeq \rho^2 \dot{\mathbf{t}}_0(\rho s) + \ddot{u}_i(s) \mathbf{t}_{\perp,0}^i(\rho s) \end{aligned} \quad (\text{C.1})$$

And so we conclude that we can treat the channel as being straight for thermal fluctuations, provided we multiply the curvature of the 0-chain by ρ^2 . The bending energy of the 0 chain, being proportional to the curvature squared, acquires then a factor of ρ^4 .

For the writhe calculation we make again use of Fullers equation 4.14, now with a homotopy from the 0-path. Keeping the interval small enough and using continuity, there is no problem proving the homotopy being valid for using the equation. We only need to project the fluctuating path to the 0-path. This projection defines a homotopy. We write $\omega(s) = \omega_0(\rho s) + \Delta \omega(s)$. The 0-path writhe is as before but multiplied by ρ , since the tangent at ρs does not change, but its rate of change does.

Finally applying Fullers equation results in:

$$\Delta \omega(s) = \frac{1}{2\pi} \frac{(\mathbf{t}_0(\rho s) \wedge \mathbf{t}(s))(\dot{\mathbf{t}}(s) + \rho \dot{\mathbf{t}}(\rho s))}{1 + \rho} \simeq \frac{1}{4\pi} (\dot{u}_r(s) \ddot{u}_p(s) - \ddot{u}_r(s) \dot{u}_p(s)) \quad (\text{C.2})$$

up to quadratic order and using the same assumptions as before.

C.2 Multi-plectoneme Entropy

In this appendix the number of configurations, $z_m(L_p)$, is calculated with fixed total plectoneme length L_p in the presence of m plectonemes. We first treat the case with hardcore interactions between the plectonemes. We make lengths dimensionless by rescaling them with a length scale. The natural length scale in the tails is not a priori clear. One could argue for the deflection length λ , which is a natural cutoff in the tails, or alternatively for the 3.5 nm helical repeat which must be a scale where nucleation of loops are influenced by. We will choose the latter as the length scale for positioning and length distribution of the plectonemes in our calculations. Measurement data are due to thermal noise not precise enough to differentiate between possible length scales. Unlike [151] we don't see a reason in our setup to consider a different linking number density in each plectoneme. The fluctuations in linking number density are in principle included in the twist and writhe fluctuations.

For a configuration with one plectoneme of length L_p and loop-length L_{loop} the number of possible configurations is $L_c - L_{\text{loop}} - L_p$, the length along the chain we can place the start of the loop. In case of 2 plectonemes sharing the length L_p , the first plectoneme we encounter, say with plectoneme length Λ_1 , can have a position x_1 between 0 and $L_c - 2L_{\text{loop}} - L_p$, while the second plectoneme can have a position x_2 in the interval $[x_1 + \Lambda_1 + L_{\text{loop}}, L_c - \Lambda_2 - L_{\text{loop}}] = [x_1 + \Lambda_1 + L_{\text{loop}}, L_c - L_p + \Lambda_1 - L_{\text{loop}}]$. The length of the interval does not depend on how L_p is divided. It is easy to show using induction that the partition sum for m loops can be written

as:

$$z_m^{\text{hc}}(\text{L}_p) = \prod_{i=1}^{m-1} \left(\int_0^{\text{L}_p - \sum_{j=0}^{i-1} \Lambda_j} d\Lambda_i \right) \prod_{k=1}^m \left(\int_{x_{k-1} + \text{L}_{\text{loop}} + \Lambda_{k-1}}^{\text{L}_c - (m-k+1)\text{L}_{\text{loop}} - \text{L}_p + \sum_{q=0}^{k-1} \Lambda_q} dx_k \right), \quad (\text{C.3})$$

with $\Lambda_0 = x_0 := 0$. To shorten the notation we define an effective chain length $\text{L}_c' := \text{L}_c - m \text{L}_{\text{loop}}$. The second product, which we denote by y_m , integrates over all positions. It can be written as

$$\begin{aligned} y_m(\text{L}_c' - \text{L}_p) &= \prod_{k=1}^m \left(\int_0^{\text{L}_c' - \text{L}_p - \sum_{q=0}^{k-1} x_q} dx_k \right) \\ &= \int_0^{\text{L}_c' - \text{L}_p} dx_1 y_{m-1}(\text{L}_c' - \text{L}_p - x_1) \\ &= \mathcal{L}^{-1} \left(\frac{1}{t^{m+1}} \right) (\text{L}_c' - \text{L}_p) \end{aligned} \quad (\text{C.4})$$

$$= \frac{(\text{L}_c' - \text{L}_p)^m}{m!} \quad (\text{C.5})$$

where in the third step \mathcal{L}^{-1} denotes an inverse Laplace transform and the faltung theorem has been used. The first term can be calculated analogously, resulting in the not so surprising result:

$$z_m^{\text{hc}}(\text{L}_p) = \frac{\text{L}_p^{m-1}}{(m-1)!} \frac{(\text{L}_c' - \text{L}_p)^m}{m!} \quad (\text{C.6})$$

This hard core interaction is probably not entirely realistic. With a minor penalty plectonemes can have overlapping tails. The effects of plectoneme interactions come into play only when most of the free DNA has been used. As a test the calculations can be performed with the other extreme of noninteracting plectonemes. Defining $\text{L}_c'' := \text{L}_c - \text{L}_{\text{loop}}$, and again implicitly rescaling all lengths by the helical repeat, we find as combinatorial factor:

$$\begin{aligned} z_m^{\text{ni}}(\text{L}_p) &= \frac{1}{m!} \prod_{i=1}^m \left(\int_0^{\text{L}_p - x_{i-1}} dx_i (\text{L}_c'' - x_i) \right) (\text{L}_c'' - \text{L}_p + \sum_{i=1}^{m-1} x_i) \\ &= \frac{1}{m!} \mathcal{L}^{-1} \left(\frac{\text{L}_c''}{t} - \frac{1}{t^2} \right)^m (\text{L}_p) \end{aligned} \quad (\text{C.7})$$

$$= \frac{1}{m!} \sum_{k=0}^m \binom{m}{k} \frac{(-1)^k \text{L}_c''^{m-k} \text{L}_p^{m+k-1}}{(m+k-1)!}, \quad (\text{C.8})$$

which, not necessarily providing more clarity, can be written using a confluent hypergeometric function as:

$$z_m^{\text{ni}}(L_p) = \frac{1}{m!} \frac{(L_c'')^m L_p^{m-1} {}_1F_1(-m, m, L_p / L_c'')}{(m-1)!} \quad (\text{C.9})$$

The experiments we have analyzed are in a range that the difference between these two extremes is too small to be able to favor one approach above the other.

Appendix D

Matlab code

This is the matlab code used for calculating the turn extension plots, as well as all related quantities. Instructions are in the headers. The code probably runs fine on Octave, only the minimization procedure `fmincon()` should be replaced by an Octave equivalent. File `plectoneme.m` call with `data=plectoneme(force,step,salt,L,Pc)`. The turns extension plots were produced with `plot(data.nsign,data.extension)`.

```
function [ data ]=plectoneme ( f , delta , salt , L , Pc , multiplect )

% Calculates the response of a dsDNA chain under tension , in a
% solution with with given monovalent salt concentration.
% INPUT:
% f ..... tension in pN
% delta ..... stepsize in turns
% salt ..... salt concentration in mM
% L ..... chain length in nm
% Pc ..... torsional persistence length in nm
% (100–120)
% multiplect ..... optional flag = 1 (default) allow for
%      ultiplectonemes
%      = 0 at most 1 plectoneme
%
% OUTPUT:
% data ..... structure that contains all
%      the output.
% data.K2 ..... contains the last K^2 before the
%      transition
% data.nsign ..... array with the linking number
% data.extension ..... array with right
% data.energy ..... array with indeed
```

```

% data.m..... array with average number of
    plectonemes
% data.Lp..... array with average total
    plectoneme length
% data.slope..... array with slopes (backward
    difference )
% data.torque..... array with torques (also bakward
    diff)
% data.drop..... drop over transition (beware
    stepsize)
% data.dropSimpleL/H.... difference between no plectoneme ad
    plectoneme before (L) and after (H) the transition if possible
% data.salt..... salt conc. as a reminder
% data.f..... tension idem
% data.Pc..... torsional Plength idem
% data.plectonems..... "multi" or "single" as a reminder
%
% other data easily added, see end of the main routine
%
% Some definitions to increase readability of code
% dropflag used for calculating the drop in extension at the
    transition
BEFORE=1;
AFTER=0;
ISROD=0;
NOROD=1;
% Setting defaults for optional inputs
if nargin<6
    multiplect=1; % Switch , when 0 , only one plectoneme
end

% make init structure for internal use , data structure for export
init=Inititiateplec(f,salt,Pc);
lloop=init.Lloop/L;

mMax=floor(L/(4*init.lambda))+1;
Lps=zeros(1,mMax+1);
energies=zeros(1,mMax+1);
extensions=zeros(1,mMax+1);

data.K2=100; % to check if the Moroz Nelson Bound is satisfied ( $K^2 > 3$ ).
Lkminp=L*init.lk+init.Wloop;

```

```

ind=floor(Lkminp/delta);
data.nsign=(1:ind).*delta;
lk=data.nsign./L;
Kr=sqrt(f*init.Pb/init.kbt-(pi.*init.Pcp.*lk+init.B*init.f/(2*init.S)).^2);
data.extension=L.*(1+(init.f-2.*pi.*init.B.*lk.*init.kbt)./init.S-1./(2.*Kr).*(1+1./(64.*Kr.^2)).*(1-(2.*lk.*pi.*init.Pcp+init.B*init.f/init.S).*init.kbt.*init.B./(2.*init.Pb.*init.S))));
data.energy=L.*(2.*pi.^2.*init.Pc.*lk.^2-(init.f-2.*pi.*init.kbt.*init.B.*lk).^2./(2.*init.S.*init.kbt)-init.f./init.kbt+Kr./init.Pb.*(1-1./(4.*Kr))));
data.K2=Kr(ind)^2;
dropflag=BEFORE;
ind=ind+1; % indexes the output arrays
Lk=ind*delta;
mstart=0;% minimum number of plectonemes. Drop from the lower end
when their energy becomes too high
stopFlag=1;
while (stopFlag); % the main loop
    %first some initialization
    stopFlag=0;
    m=1;
    nu=Lk/L; % the linking number density
    if isequal(mstart,ISROD) % do we still need to calculate
        plectonemeless configuration
        [rhorod,K2,freed]=rhoTension(nu,init);
        if K2>init.k2min% are we far enough from bifurcation to
            make sense of the data, meaning K2>3 etc, or if no
            plectoneme can form check against the lowest admissable
            value
            stopFlag=1;
            energies(1)=L*freed;
            extensions(1)=rhorod*L;
        else % torsion too close to the bifurcation point.
            mstart=NOROD;
            energies(1)=Inf;
        end
    end
    % no rod anymore
    energies(1)=Inf;
end
ground=energies(1);
lplect=(nu-init.lk-init.Wloop/L)/init.lkdiff;
% Next we go through multiple plectoneme configurations with the
condition that the plectoneme length and the extension are

```

```

    positive and if we do not want mp configurations only the m=1
    case
    while lplect>0&& init.rhotail*(1-lplect)-m*lloop>0&&(
        multiplect||isequal(m,1))
        stopFlag=1;
        if isequal(multiplect,1) % entropy with hardcore repulsion
            between plectonemes
            FreeEnt=(+log(lplect/(m*init.unit/L))-m*log(lplect*(
                init.rhotail*(1-lplect)-m*lloop)/(init.unit/L)^2)+2*
                log(factorial(m)));
        else % no entropic gain from multiple plectonemes
            FreeEnt=0;
        end
        energies(m+1)=FreeEnt+L*(init.ftw+init.gt+lplect*init.delg
            )+m*init.Eloop;
        extensions(m+1)=L*(init.rhotail*(1-lplect)-m*lloop);
        Lps(m+1)=L*lplect;
        ground=min(energies(m+1),ground);
        m=m+1;
        lplect=(nu-init.lk-m*init.Wloop/L)/init.lkdif;
    end
%
% Collecting all the data for this round
%
    if stopFlag
        data.nsign(ind)=Lk;
        Z=exp(-(energies(mstart+1:m)-ground));
        Zt=sum(Z);
        data.extension(ind)=sum(extensions(mstart+1:m).*Z)/Zt;
        data.energy(ind)=sum(energies(mstart+1:m).*Z)/Zt;
        data.Lp(ind)=sum(Lps(mstart+1:m).*Z)/Zt;
        data.m(ind)=sum((mstart:m-1).*Z)/Zt;
% to estimate the drop in extension obver the transition. 2
% methods used , either look at the difference in average
% extension before and after
% or the difference between rod extension and one plectoneme
% extension just before or just after the transition
% the first is in principle more correct but only for
% infintesimal small step size , so compare it with the
% simplistic approach. Alternatively we could refine around the
% transition.
        if (isequal(dropflag,BEFORE) && m>1)% rod energy was the
            groundstate

```

```

        if ground<energies(1)% rod energy is no groundstate
            anymore
            dropflag=AFTER;
            data.drop=data.extension(ind-1)-data.extension(ind
            );
            data.dropSimpleH=extensions(1)-extensions(2);
        else
            data.dropSimpleL=extensions(1)-extensions(2);
            data.K2=min(K2,data.K2); % store the lowest
            Moroz-Nelson K^2, so we can check later how
            reliable the transition is
        end
    end
    Lk=Lk+delta;
    ind=ind+1;
end
end
data.slope=(data.extension(2:ind-1)-data.extension(1:ind-2))./(
    data.nsign(1:ind-2)-data.nsign(2:ind-1));
data.torque=init.kbt.*(data.energy(2:ind-1)-data.energy(1:ind-2))
    ./(2*pi*delta);
% finally define the data that we want to have output for. add a
% line for extra data interested in or reove the % in front
data.salt=salt;
data.f=f;
data.L=L;
data.Pc=Pc;
data.R=init.R;
switch multiplect
    case 0
        data.plectonemes='one';
    otherwise
        data.plectonemes='multi';
end
% Optional output, plectoneme parameters : R, alpha, sdr and lk
% data.R=init.R
% data.alpha=init.alphast
% data.sdr=init.sdrst
% data.lktail=init.lk
end

function init=Inititiateplec(f,salt,Pc)
%
```

```

% Defines the init structure that holds all kinds of data that is
% needed during the calculations.
% and the Data structure for output
% We use the inifinite chain model to get good values for the 4
% parameters
init=calcplectparm(f,salt,Pc);
init.k2min=2; % min of allowed K^2
tp=1-0.3799*(init.R/init.lambda+0.0112)^2;
init.Wloop=asin(tp)*2./pi; % writhe of the loop
init.Lloop=4*init.lambda*tp;
init.Eloop=2*init.Lloop*f/init.kbt;
init.unit=3.5; % the cutoff
init.lkdif=init.writhe+init.lks-init.lk;
end

function [rho,K2,freed]=rhoTension(lk,init)
% calculates the contraction of the tails, the twist energy density
% , K^2 as a check and the free energy density depending
% on linking density and material parameters
K2=init.f*init.Pb/init.kbt-(pi*init.Pcp*lk+init.B*init.f/(2*init.S
))^2;
Kr=sqrt(K2); % Kr is the K of Moroz-Nelson with
% corrections
rho=1+(init.f-2*pi*init.B*lk*init.kbt)/init.S-1/(2*Kr)
*(1+1/(64*Kr^2))*(1-(2*lk*pi*init.Pcp+init.B*init.f/init
.S)*init.kbt*init.B/(2*init.Pb*init.S));
freed=2*pi^2*init.Pc*lk^2-(init.f-2*pi*init.kbt*init.B*lk)
^2/(2*init.S*init.kbt)-init.f/init.kbt+Kr/init.Pb
*(1-1/(4*Kr));
end

```

File calcplectparm.m is used internally to get the plectoneme parameters.

```

function [init]=calcplectparm(f,cs,Pc)
% This function calculates the one plectoneme
% parameters in the infinite chain limit
%
% f force in pN
% cs monovalent salt in mM
% Pc torsional persistence length 100 is fine

```

```

[init]=initiate(f,cs,Pc); % initiation of init structure that
% carries all

```



```

% nonchanging parameters for internal use and the data structure
% that are used to export results
lkcr=(sqrt(f*init.Pb/init.kbt)-init.B*f/(2*init.S))/(pi*init.Pcp);
% more or less the bifurcation point
% There is a slight dependance of the plectoneme variables on the
% linking
% number density. We initiate it with something reasonable and
% then compare
% the final result with the old value and updates it till it
% converges .
lkstart=0.8*lkcr;
nu=lkcr+ .02; % to be safe
init.alphast=1; %init plectoneme angle
init.sdrst=1/(2*init.kappa); % init radial sd
init.R=1/init.kappa; % init plectoneme radius
lkmax=sqrt(f*init.Pb/init.kbt-1)/(pi*init.Pcp);% making sure we
% stay within bounds during minimization
options = optimset('Algorithm','interior-point','GradObj','off','GradConstr','off','Display','off','DerivativeCheck','off');
fe = @(parm) freeEnergy(parm,init,nu);
par=fmincon(fe,[lkstart;init.R;init.alphast;init.sdrst],[],[],[],[0;1+0.5/init.kappa;pi/4;0.1/init.kappa],[lkmax;init.Pb;7*pi/16;init.Pb],[],options);
init.lk=par(1);
init.R=par(2);
init.alphast=par(3);
init.sdrst=par(4);
[~,init.lks,init.rhostr,init.writhe]=freeEnergy(par,init,nu); %
% based on the just calculated parameters get the important
% quantities
nu=(init.writhe+init.lks+2*lkcr)/2;% Here we set the linking
% number we calculate the data for. in between lkcr and wr+lks+
% lkcr (is actually a bit too high
fe = @(parm) freeEnergy(parm,init,nu);

par=fmincon(fe,[init.lk;init.R;init.alphast;init.sdrst],[],[],[],[0;1+0.5/init.kappa;pi/4;0.1/init.kappa],[lkmax;init.Pb;7*pi/16;init.Pb],[],options);
init.lk=par(1);
init.R=par(2);
init.alphast=par(3);
init.sdrst=par(4);

```

```
[~,init.lks,init.rhostr,init.writhe,init.delg,init.gt,init.ftw]=
    freeEnergy(par,init,nu); % based on the just calculated
    parameters get the important quantities
init.K2pl=f*init.Pb/init.kbt-(pi*init.Pcp*init.lk+init.B*f/(2*init
.S))^2; % K^2 we need for fluctuation check
init.rhotail=1+(f-2*pi*init.B*init.kbt*init.lk)/init.S-1/(2*sqrt(
init.K2pl));
init.oneslope=init.rhotail/(init.writhe+init.lks-init.lk); % as is
    custom, we use the negative of the slope
end
```

```
function [freed,lks,rhostr,writhe,delg,gt,ftw]=freeEnergy(par,init
,nu)
    lk=par(1);
    R=par(2);
    alpha=par(3);
    sdr=par(4);
    ftw=2*pi^2*init.Pceff*lk^2; % twist energy based on lk to
        calculate lk strand
    gt=ftail(lk,init)-ftw; % this is gt from the text, the twist
        energy is seperated
    lambdaP=(init.Pb*(pi*R*sin(alpha))^2)^(1/3);
    lambdaR=(init.Pb*sdr^2)^(1/3);
    lambdaS=2*(lambdaR*lambdaP^3+lambdaR^2*lambdaP^2+lambdaR^3*
        lambdaP)/((lambdaR+lambdaP)*(lambdaR^2+lambdaP^2));
    lks=sqrt(ftw/(2*pi^2*init.Pcp*(1-lambdaS*init.Pcp/(4*init.Pb
        ^2))));
    rhostr=1-2*init.B*init.kbt*lks/init.S-1/(4*init.Pb)*(lambdaR+
        lambdaP)+2*lambdaS*init.B*pi*init.Pcp*init.kbt*lks/(init.S*
        init.Pb^2);
    fentr=3/8*(1/lambdaR+1/lambdaP);
    fbend=rhostr^4*init.Pb*cos(alpha)^4/(2*R^2);
    fel=elect(R,alpha,sdr,init);
    writhe=rhostr*sin(2*alpha)/(4*pi*R);
    delg=(fbend+fel+fentr-gt);
    lp=(nu-lk)/(writhe+lks-lk);
    freed=ftw+gt+lp*delg;
end
```

```
function ft=ftail(lk,init)
%
```

```
% calculates the free energy according to Moroz–Nelson
K=sqrt( init.f*init.Pb/ init.kbt-(pi*init.Pc*lk+init.B*init.f
/(2*init.S))^2);
ft=2*pi^2*init.Pc*lk^2-(init.f-2*pi*init.kbt*init.B*lk)^2/(2*
init.S*init.kbt)-init.f/ init.kbt+K/ init.Pb*(1-1/(4*K)-1/(64*
K^2));
```

```
end
```

```
function elect=elect(R,alpha,sdr,init)
% Ubbink Odijk  $\mu > 1/4$  with entropic correction term
%
% INPUT
% R      plectoneme radius
% csa    cosine of plect angle
% init   data structure
% dr     fluctuation tube radius  $dr^2 = 2*sdr^2$ 
%
% OUTPUT
% elect  free energy per length
```

```
w=2*init.kappa*R;
mu=tan(alpha)^2./4;
elect=init.Qb*(init.nu).^2./(2).*sqrt(2*pi./w)*exp(-w)*Z(mu)*exp
(4*init.kappa.^2*sdr^2);
end
```

```
function [init]=inititiate(f,cs,Pc)
% Function calculates the important structure. For internal use is
the init
% structure
[init.nu,init.kbt,init.kappa,init.Qb]=EffectiveCharge(cs); %
calculates the effective line charge according to Philip and
Wooding rs is the radius where potential = 1
init.f=f; % the tension
init.Pb=50+1/(4*init.kappa^2*max(init.Qb,0.17)); % persistence
length including OSF correction, taking care of Manning
condensation
init.lambda=sqrt(init.kbt*init.Pb/f); % deflection length for
chain under tension
init.S=1200; % stretch modulus in pN
init.B=-21; % stretch twist coupling, dimensionless see Wang PNAS/
Marko
init.Pc=Pc;
```

```

init.Pcp=Pc-init.kbt*init.B^2/init.S; %twist stretch coupling
    corrected torsional persistence length
init.Pceff=init.Pcp*(1-init.lambda*init.Pcp/(4*init.Pb^2));
end

```

```

function z=Z(m)
% Ubbinks and Odijks approximation
m1=0.207;
m2=0.054;
z=1+m1/m+m2/m^2;
end

```

File EffectiveCharge.m calculates the effective charge following [165].

```

function [nueff ,kbt ,kappa ,Qb]=EffectiveCharge(cs)
% Calculates the effective charge of DNA at a given salt
    concentration
% following the scheme of Philip and Wooding ,JCP 52,1970.
    matching asymptotics
%
%
% INPUT
% cs monovalent salt concentration in mM in range 1 till over 2500
%
% OUTPUT
% nueff..... effective charge of the centerline
% kbt..... thermal energy
% kappa..... inverse screening length
% Qb..... Bjerrum length

kbt=4.1; % in pNnm
rDNA=1; %radius of DNA in nm
nu=2./0.34; % in charges/ nm
ns=cs.*6.022*10^(-4); % number density in #/(nm)^3
q=1.602176487*10.^(-19); % elementary charge in [C]
perm=80.1; % permittivity of water at 20 C
eps0=8.85*10.^(-42); % dielectric constant of vacuum in [C]^2/([pN
    ]*[nm]^2)
Qb=(q.^2)./(4*pi*perm*eps0*kbt); % Bjerrum length in nm
kappa=sqrt(2*q.^2.*ns./(eps0*perm*kbt)); % inverse screening
    length in nm^-1
DPsi0=-2*Qb*nu/(kappa.*rDNA); % reduced boundary conditions
R0=rDNA*kappa;
if R0>0.6

```

```

        Rs =iscase5 (R0,DPsi0);
    else
        Rs=0;
    end
    if isequal (Rs,0);
        Rs = iscase3 (R0,DPsi0);
    end
    nueff=1/(2*Qb*besselk (0 ,Rs));

%
% The beta for cases 3 and 5
%
function bet=bet (rs)
bet=sqrt (exp (1) .* rs.^2-(2-rs.*besselk (1 ,rs) ./besselk (0 ,rs)).^2);

% Case 3
%
function [Rs ,pot]=iscase3 (R0,DPsi0)
Rs1=0.601973;
Rs2=1.552651;
Rb=min (Rs2 ,bound2 (R0));
if (dpsi3 (R0,Rs1 ,DPsi0)*dpsi3 (R0,Rb ,DPsi0)>=0);
    Rs=0;
    pot=0;
else
    [Rs ,~,flag]=fzero (@(rs) dpsi3 (R0 ,rs ,DPsi0) ,[Rs1 ,Rb]);
    bet1=bet (Rs);
    if (flag <0||Rs1>Rs||Rs>Rs2||(bet1^2)>exp (1)*Rs2.^2);
        Rs=0;
        pot=0;
    else
        pot=-2*log (R0 ./bet1*sin (bet1 ./2*log (Rs ./R0)+asin (bet1 ./
            sqrt (exp (1)) .*Rs)))));
    end
end

function dpsi=dpsi3 (R,rs ,DPsi0)
bet1=bet (rs);
dpsi=-2./R*(1-bet1./2*cot (bet1 ./2*log (rs ./R)+asin (bet1 ./
    sqrt (exp (1)) .*rs))))-DPsi0;

```

% Case 5

```
function [Rs, pot]=iscase5 (R0, DPsi0)
Rs2=1.552651;
Rb=bound (R0);
if (Rb<Rs2 || dps5 (R0, Rs2, DPsi0)*dps5 (R0, Rb, DPsi0) >=0);
Rs=0;
pot=0;
else
[Rs, ~, flag]=fzero (@(rs) dps5 (R0, rs, DPsi0), [Rs2, Rb]);
bet1=bet (Rs);
if (flag < 0 || (bet1 ^2) < exp(1)*Rs2.^2);
Rs=0;
pot=0;
else
pot=-2*log (R0 ./ bet1 * sin (bet1 ./2 * log (R0 ./ Rs)+asin (bet1
./ (sqrt (exp(1)) .* Rs)))));
end
end
```

```
function dps5=dps5 (R, rs, DPsi0)
bet1=bet (rs);
dps5=-2./R*(1+bet1 ./2 * cot (bet1 ./2 * log (R ./ rs)+asin (bet1 ./ (sqrt (exp
(1)) .* rs))))-DPsi0;
```

```
function rb=bound (R0)
fun=@(rs) R0-rs*exp (-2./bet (rs)*asin (bet (rs) ./ (sqrt (exp(1)) .* rs)))
;
rb=fzero (fun, [0.602, 100]) -0.0001;
```

```
function rb=bound2 (R0)
fun=@(rs) R0-rs.*exp (-2./bet (rs) .* (pi-asin (bet (rs) ./ (sqrt (exp(1))
.* rs)))));
rb=fzero (fun, [0.602, 100]) -0.0001;
```

Bibliography

- [1] Pierre Gilles de Gennes. “Suspensions colloïdales dans une solution de polymères”. In: *C.R. Acad. Sc.* 288 (June 1979), p. 359 (cit. on pp. 1, 4, 24).
- [2] J. Des Cloizeaux and G. Jannink. *Polymers in solution: their modelling and structure*. Oxford University Press, 2010 (cit. on pp. 1, 4).
- [3] Alexander Yu. Grosberg and A.R. Khokhlov. *Statistical physics of macromolecules*. AIP press Woodbury (NY), 1994 (cit. on pp. 1, 17, 18, 24).
- [4] M. Doi and S.F. Edwards. *The theory of polymer dynamics*. Oxford University Press, 1988 (cit. on p. 1).
- [5] H. Yamakawa. *Modern theory of polymer solutions*. Harper & Row (New York), 1971. HDL: 2433/50527 (cit. on p. 1).
- [6] P.J. Flory. *Principles of polymer chemistry*. Cornell Univ Pr, 1953 (cit. on p. 1).
- [7] A.R. Barron. “[Entropy and the central limit theorem](#)”. In: *Ann. Probab.* (1986), pp. 336–342. ISSN: 0091-1798. DOI: 10.1214/aop/1176992632 (cit. on p. 2).
- [8] S. Asakura and F. Oosawa. “[Interaction between particles suspended in solutions of macromolecules](#)”. In: *J. Polym. Sci.* 33.126 (1958), pp. 183–192. DOI: 10.1002/pol.1958.1203312618 (cit. on pp. 2, 24).
- [9] Eric Verlinde. “[On the Origin of Gravity and the Laws of Newton](#)”. In: *J. High Energy Phys.* 2011.4 (2011), pp. 1–27. DOI: 10.1007/JHEP04(2011)029 (cit. on p. 2).
- [10] JC Le Guillou and J. Zinn-Justin. “Critical exponents from field theory”. In: *Phys. Rev. B* 21 (1980), pp. 3976–3998. DOI: 10.1103/PhysRevB.21.3976 (cit. on p. 3).
- [11] J.L. Cardy and H.W. Hamber. “ $O(n)$ Heisenberg Model Close to $n = d = 2$ ”. In: *Phys. Rev. Lett.* 45.7 (1980), pp. 499–501. DOI: 10.1103/PhysRevLett.45.499 (cit. on p. 3).
- [12] PG De Gennes. “Exponents for the excluded volume problem as derived by the Wilson method”. In: *Phys. Lett. A* 38.5 (1972), pp. 339–340. DOI: 10.1016/0375-9601(72)90149-1 (cit. on p. 4).

- [13] K.G. Wilson and M.E. Fisher. “[Critical exponents in 3.99 dimensions](#)”. In: *Phys. Rev. Lett.* 28.4 (1972), pp. 240–243. DOI: 10.1103/PhysRevLett.28.240 (cit. on p. 4).
- [14] J.D. Watson and F.H.C. Crick. “[Molecular structure of nucleic acids](#)”. In: *Nature* 171.4356 (1953), pp. 737–738. DOI: 10.1038/171737a0 (cit. on p. 4).
- [15] O. Kratky and G. Porod. “Röntgenuntersuchung gelöster fadenmoleküle”. In: *Recl. Trav. Chim. Pays-Bas* 68.12 (1949), pp. 1106–1122. DOI: 10.1002/recl.19490681203 (cit. on p. 4).
- [16] L. Onsager. “The effects of shape on the interaction of colloidal particles”. In: *Ann. N. Y. Acad. Sci.* 51.4 (1949), pp. 627–659. DOI: 10.1111/j.1749-6632.1949.tb27296.x (cit. on pp. 5, 19).
- [17] M. Emanuel et al. “[The physics behind the larger scale organization of DNA in eukaryotes](#)”. In: *Phys. Biol.* 6 (2009), p. 025008. ISSN: 1478-3975. DOI: 10.1088/1478-3975/6/2/025008 (cit. on p. 5).
- [18] Curt A Davey et al. “[Solvent mediated interactions in the structure of the nucleosome core particle at 1.9 a resolution.](#)” In: *J. Mol. Biol.* 319.5 (June 2002), pp. 1097–113. ISSN: 0022-2836. DOI: 10.1016/S0022-2836(02)00386-8 (cit. on p. 7).
- [19] Helmut Schiessel. “[The physics of chromatin](#)”. In: *J. Phys.: Condens. Matter* 15 (2003), R699–R774. DOI: 10.1088/0953-8984/15/19/203 (cit. on pp. 7, 9).
- [20] Igor M Kulić and Helmut Schiessel. “Opening and Closing DNA: Theories on the Nucleosome”. In: *DNA interactions with polymers and surfactants*. Ed. by Rita Dias and Björn Lindman. John Wiley & Sons, 2008. Chap. 7, pp. 173–208. ISBN: 978-0-470-25818-7. DOI: 10.1002/9780470286364.ch7 (cit. on p. 7).
- [21] J Bednar et al. “[Nucleosomes, linker DNA, and linker histone form a unique structural motif that directs the higher-order folding and compaction of chromatin.](#)” In: *PNAS* 95.24 (Nov. 1998), pp. 14173–8. ISSN: 0027-8424. DOI: 10.1073/pnas.95.24.14173 (cit. on pp. 8, 9).
- [22] Boris Mergell, Ralf Everaers, and Helmut Schiessel. “[Nucleosome interactions in chromatin: fiber stiffening and hairpin formation.](#)” In: *Phys. Rev. E* 70.1 Pt 1 (July 2004), p. 011915. ISSN: 1539-3755. DOI: 10.1103/PhysRevE.70.011915 (cit. on pp. 8, 14).
- [23] Ken van Holde and Jordanka Zlatanova. “Chromatin fiber structure: Where is the problem now?” In: *Semin. Cell Dev. Biol.* 18.5 (Oct. 2007), pp. 651–8. ISSN: 1084-9521. DOI: 10.1016/j.semcdb.2007.08.005 (cit. on p. 9).
- [24] J. T. Finch and A. Klug. “[Solenoidal Model for Superstructure in Chromatin](#)”. In: *PNAS* 73 (June 1976), pp. 1897–1901. DOI: 10.1073/pnas.73.6.1897 (cit. on p. 9).

- [25] M. Kruithof et al. “[Single-molecule force spectroscopy reveals a highly compliant helical folding for the 30-nm chromatin fiber](#)”. In: *Nat. Struct. Mol. Biol.* 16.5 (2009), pp. 534–540. DOI: 10.1038/nsmb.1590 (cit. on pp. 9, 12).
- [26] C. L. Woodcock, L L Frado, and J B Rattner. “[The higher-order structure of chromatin: evidence for a helical ribbon arrangement.](#)” In: *J. Cell Biol.* 99.1 Pt 1 (July 1984), pp. 42–52. ISSN: 0021-9525. DOI: 10.1083/jcb.99.1.42 (cit. on p. 9).
- [27] A Worcel, S Strogatz, and D Riley. “[Structure of chromatin and the linking number of DNA.](#)” In: *PNAS* 78.3 (Mar. 1981), pp. 1461–5. ISSN: 0027-8424. DOI: 10.1073/pnas.78.3.1461 (cit. on p. 9).
- [28] D.Z. Staynov. “Possible nucleosome arrangements in the higher-order structure of chromatin”. In: *Int. J. Biol. Macromol.* 5 (1983), pp. 3–9. DOI: 10.1016/0141-8130(83)90071-5 (cit. on p. 9).
- [29] C. L. Woodcock et al. “[A Chromatin Folding Model that Incorporates Linker Variability Generates Fibers Resembling the Native Structures](#)”. In: *PNAS* 90 (Oct. 1993), pp. 9021–9025. DOI: 10.1073/pnas.90.19.9021 (cit. on p. 9).
- [30] Benedetta Dorigo et al. “[Nucleosome Arrays Reveal the Two-Start Organization of the Chromatin Fiber](#)”. In: *Science* 306 (Nov. 2004), pp. 1571–1573. DOI: 10.1126/science.1103124 (cit. on p. 9).
- [31] Philip J J Robinson et al. “[EM measurements define the dimensions of the “30-nm” chromatin fiber: evidence for a compact, interdigitated structure.](#)” In: *PNAS* 103.17 (Apr. 2006), pp. 6506–11. ISSN: 0027-8424. DOI: 10.1073/pnas.0601212103 (cit. on pp. 9, 11).
- [32] P T Lowary and J Widom. “[New DNA sequence rules for high affinity binding to histone octamer and sequence-directed nucleosome positioning.](#)” In: *J. Mol. Biol.* 276.1 (Feb. 1998), pp. 19–42. ISSN: 0022-2836. DOI: 10.1006/jmbi.1997.1494 (cit. on p. 9).
- [33] Van A T Huynh, Philip J J Robinson, and Daniela Rhodes. “[A method for the in vitro reconstitution of a defined “30 nm” chromatin fibre containing stoichiometric amounts of the linker histone.](#)” In: *J. Mol. Biol.* 345.5 (Feb. 2005), pp. 957–68. ISSN: 0022-2836. DOI: 10.1016/j.jmb.2004.10.075 (cit. on p. 9).
- [34] M. Depken and H. Schiessel. “[Nucleosome shape dictates chromatin fiber structure](#)”. In: *Biophys. J.* 96.3 (2009), pp. 777–784. DOI: 10.1016/j.bpj.2008.09.055 (cit. on pp. 10, 11).
- [35] J Dubochet and M Noll. “Nucleosome arcs and helices.” In: *Science* 202.4365 (Oct. 1978). Nucleosome wedge-angle, pp. 280–6. ISSN: 0036-8075. DOI: 10.1126/science.694532 (cit. on pp. 10, 12).

- [36] Andrew Routh, Sara Sandin, and Daniela Rhodes. “[Nucleosome repeat length and linker histone stoichiometry determine chromatin fiber structure.](#)” In: *PNAS* 105.26 (July 2008), pp. 8872–7. ISSN: 1091-6490. DOI: 10.1073/pnas.0802336105 (cit. on pp. 11, 12).
- [37] F Thoma, T Koller, and A Klug. “[Involvement of histone H1 in the organization of the nucleosome and of the salt-dependent superstructures of chromatin.](#)” In: *J. Cell Biol.* 83.2 Pt 1 (Nov. 1979), pp. 403–27. ISSN: 0021-9525. DOI: 10.1083/jcb.83.2.403 (cit. on p. 12).
- [38] Stéphanie Mangenot et al. “[Salt-induced conformation and interaction changes of nucleosome core particles.](#)” In: *Eur. Biophys. J.* 82.1 Pt 1 (Jan. 2002), pp. 345–56. ISSN: 0006-3495. DOI: 10.1016/S0006-3495(02)75399-X (cit. on p. 13).
- [39] Stéphanie Mangenot et al. “[Interactions between isolated nucleosome core particles: A tail-bridging effect?](#)” In: *Eur. Phys. J. E* 7.3 (2002), pp. 221–231. DOI: 10.1140/epje/i200101151 (cit. on p. 13).
- [40] Aurélie Bertin et al. “[Role of histone tails in the conformation and interactions of nucleosome core particles.](#)” In: *Biochemistry* 43.16 (Apr. 2004), pp. 4773–80. ISSN: 0006-2960. DOI: 10.1021/bi036210g (cit. on p. 13).
- [41] M Garcia-Ramirez, F Dong, and J Ausio. “[Role of the histone “tails” in the folding of oligonucleosomes depleted of histone H1.](#)” In: *J. Biol. Chem.* 267.27 (Sept. 1992), pp. 19587–95. ISSN: 0021-9258. medline: 1527076 (cit. on p. 13).
- [42] T M Fletcher and J C Hansen. “[Core histone tail domains mediate oligonucleosome folding and nucleosomal DNA organization through distinct molecular mechanisms.](#)” In: *J. Biol. Chem.* 270.43 (Oct. 1995), pp. 25359–62. ISSN: 0021-9258. DOI: 10.1074/jbc.270.43.25359 (cit. on p. 13).
- [43] F. Mühlbacher, C. Holm, and Helmut Schiessel. “[Controlled DNA compaction within chromatin: The tail-bridging effect](#)”. In: *Europhys. Lett.* 73.1 (2006), pp. 135–141. DOI: 10.1209/epl/i2005-10351-4 (cit. on p. 13).
- [44] Kerstin Bystricky et al. “[Long-range compaction and flexibility of interphase chromatin in budding yeast analyzed by high-resolution imaging techniques](#)”. In: *PNAS* 101.47 (Nov. 2004). DOI: 10.1073/pnas.0402766101 (cit. on pp. 13, 14, 23).
- [45] Irina Solovei et al. “[Spatial Preservation of Nuclear Chromatin Architecture during Three-Dimensional Fluorescence in Situ Hybridization \(3D-FISH\)](#)”. In: *Exp. Cell Res.* 276.1 (May 2002), pp. 10–23. DOI: 10.1006/excr.2002.5513 (cit. on p. 13).
- [46] Claudia Hepperger et al. “[Preservation of large-scale chromatin structure in FISH experiments.](#)” In: *Chromosoma* 116.2 (Apr. 2007), pp. 117–33. ISSN: 0009-5915. DOI: 10.1007/s00412-006-0084-2 (cit. on p. 13).

- [47] Gero Wedemann and J. Langowski. “[Computer simulation of the 30-nanometer chromatin fiber.](#)” In: *Biophys. J.* 82.6 (June 2002), pp. 2847–59. ISSN: 0006-3495. DOI: 10.1016/S0006-3495(02)75627-0 (cit. on p. 14).
- [48] Y Cui and Carlos Bustamante. “[Pulling a single chromatin fiber reveals the forces that maintain its higher-order structure.](#)” In: *PNAS* 97.1 (Jan. 2000), pp. 127–32. ISSN: 0027-8424. DOI: 10.1073/pnas.97.1.127 (cit. on p. 14).
- [49] Thomas Cremer et al. “[Analysis of chromosome positions in the interphase nucleus of Chinese hamster cells by laser-UV-microirradiation experiments.](#)” In: *Hum. Genet.* 62.3 (1982), pp. 201–9. ISSN: 0340-6717. DOI: 10.1007/BF00333519 (cit. on pp. 14, 22).
- [50] Miguel R. Branco and Ana Pombo. “[Intermingling of chromosome territories in interphase suggests role in translocations and transcription-dependent associations.](#)” In: *PLoS Biol.* 4.5 (May 2006), e138. ISSN: 1545-7885. DOI: 10.1371/journal.pbio.0040138 (cit. on p. 14).
- [51] Heiner Albiez et al. “Chromatin domains and the interchromatin compartment form structurally defined and functionally interacting nuclear networks”. In: *Chromosome Res.* 14.7 (Nov. 2006). DOI: 10.1007/s10577-006-1086-x (cit. on pp. 14, 21, 23).
- [52] G van den Engh, R K Sachs, and B J Trask. “Estimating genomic distance from DNA sequence location in cell nuclei by a random walk model”. In: *Science* 257.5075 (1992), pp. 1410–1412. DOI: 10.1126/science.1388286 (cit. on p. 14).
- [53] P Hahnfeldt et al. “[Polymer models for interphase chromosomes.](#)” In: *PNAS* 90.16 (Aug. 1993), pp. 7854–8. ISSN: 0027-8424. DOI: 10.1073/pnas.90.16.7854 (cit. on pp. 15, 18).
- [54] R K Sachs et al. “[A random-walk/giant-loop model for interphase chromosomes.](#)” In: *PNAS* 92.7 (Mar. 1995), pp. 2710–4. ISSN: 0027-8424. DOI: 10.1073/pnas.92.7.2710 (cit. on p. 15).
- [55] C. Munkel and J. Langowski. “Chromosome structure predicted by a polymer model”. In: *Phys. Rev. E* 57.5 (May 1998), pp. 5888–5896. DOI: 10.1103/PhysRevE.57.5888 (cit. on p. 15).
- [56] D E Comings. “Mechanisms of chromosome banding and implications for chromosome structure.” In: *Annu. Rev. Genet.* 12 (1978), pp. 25–46. ISSN: 0066-4197. DOI: 10.1146/annurev.ge.12.120178.000325 (cit. on p. 15).
- [57] H Caron et al. “[The human transcriptome map: clustering of highly expressed genes in chromosomal domains.](#)” In: *Science* 291.5507 (Feb. 2001), pp. 1289–92. ISSN: 0036-8075. DOI: 10.1126/science.1056794 (cit. on p. 15).
- [58] Julio Mateos-Langerak et al. “[Chromatin Folding in Relation to Human Genome Function](#)”. In: (2007). arXiv:0705.1656v1 [q-bio.GN] (cit. on pp. 15, 17–19).

- [59] J. Mateos-Langerak et al. “[Spatially confined folding of chromatin in the interphase nucleus](#)”. In: *PNAS* 106.10 (2009), p. 3812. DOI: 10.1073/pnas.0809501106 (cit. on p. 15).
- [60] Manfred Bohn, Dieter W Heermann, and Roel van Driel. “[Random loop model for long polymers](#).” In: *Phys. Rev. E* 76.5 Pt 1 (Nov. 2007), p. 051805. ISSN: 1539-3755. DOI: 10.1103/PhysRevE.76.051805 (cit. on p. 15).
- [61] M Cremer et al. “[Non-random radial higher-order chromatin arrangements in nuclei of diploid human cells](#).” In: *Chromosome Res.* 9.7 (2001), pp. 541–67. ISSN: 0967-3849. DOI: 10.1023/A:1012495201697 (cit. on p. 16).
- [62] M. Daoud et al. “Solutions of Flexible Polymers. Neutron Experiments and Interpretation”. In: *Macromolecules* 8.6 (1975), pp. 804–818. ISSN: 0024-9297. DOI: 10.1021/ma60048a024 (cit. on p. 16).
- [63] Rhonald Lua, Alexander L. Borovinskiy, and Alexander Yu. Grosberg. “[Fractal and statistical properties of large compact polymers: a computational study](#)”. In: *Polymer* 45 (2004), pp. 717–731. DOI: 10.1016/j.polymer.2003.10.073 (cit. on p. 17).
- [64] Angelo Rosa and Ralf Everaers. “[Structure and dynamics of interphase chromosomes](#).” In: *PLoS Comput. Biol.* 4.8 (2008), e1000153. ISSN: 1553-7358. DOI: 10.1371/journal.pcbi.1000153 (cit. on pp. 20, 21).
- [65] Erez Lieberman-Aiden et al. “[Comprehensive Mapping of Long-Range Interactions Reveals Folding Principles of the Human Genome](#)”. In: *Science* 326.5950 (2009), pp. 289–293. DOI: 10.1126/science.1181369 (cit. on p. 20).
- [66] A.Y. Grosberg, SK Nechaev, and EI Shakhnovich. “[The role of topological constraints in the kinetics of collapse of macromolecules](#)”. In: *J. Phys.* 49.12 (1988), pp. 2095–2100. DOI: 10.1051/jphys:0198800490120209500 (cit. on p. 20).
- [67] Pierre Gilles de Gennes. “[Kinetics of collapse for a flexible coil](#)”. In: *J. Phys., Lett.* 46.14 (1985), pp. 639–642. DOI: 10.1051/jphyslet:019850046014063900 (cit. on p. 20).
- [68] Thomas Cremer et al. “[Higher order chromatin architecture in the cell nucleus: on the way from structure to function](#).” In: *Biol. Cell* 96.8 (Oct. 2004), pp. 555–67. ISSN: 0248-4900. DOI: 10.1016/j.biolcel.2004.07.002 (cit. on p. 21).
- [69] J Nickerson. “[Experimental observations of a nuclear matrix](#).” In: *J. Cell Sci.* 114.Pt 3 (Feb. 2001), pp. 463–74. ISSN: 0021-9533. PMID: 11171316 (cit. on p. 21).
- [70] W F Marshall et al. “[Interphase chromosomes undergo constrained diffusional motion in living cells](#).” In: *Curr. Biol.* 7.12 (Dec. 1997), pp. 930–9. ISSN: 0960-9822. DOI: 10.1016/S0960-9822(06)00412-X (cit. on p. 22).
- [71] J R Paulson and U K Laemmli. “[The structure of histone-depleted metaphase chromosomes](#).” In: *Cell* 12.3 (Nov. 1977), pp. 817–28. ISSN: 0092-8674. DOI: 10.1016/0092-8674(77)90280-X (cit. on p. 22).

- [72] W C Earnshaw et al. "[Topoisomerase II is a structural component of mitotic chromosome scaffolds.](#)" In: *J. Cell Biol.* 100.5 (May 1985), pp. 1706–15. ISSN: 0021-9525. DOI: 10.1083/jcb.100.5.1706 (cit. on p. 22).
- [73] Tatsuya Hirano, Ryui Kobayashi, and Michiko Hirano. "Condensins, Chromosome Condensation Protein Complexes Containing XCAP-C, XCAP-E and a Xenopus Homolog of the Drosophila Barren Protein". In: *Cell* 88 (1997), pp. 511–521. DOI: 10.1016/S0092-8674(00)80233-0 (cit. on p. 22).
- [74] C Michaelis, R Ciosk, and K Nasmyth. "Cohesins: chromosomal proteins that prevent premature separation of sister chromatids." In: *Cell* 91.1 (Oct. 1997), pp. 35–45. ISSN: 0092-8674. DOI: 10.1016/S0092-8674(01)80007-6 (cit. on p. 22).
- [75] Michael G Poirier and John F. Marko. "[Mitotic chromosomes are chromatin networks without a mechanically contiguous protein scaffold.](#)" In: *PNAS* 99.24 (Nov. 2002), pp. 15393–7. ISSN: 0027-8424. DOI: 10.1073/pnas.232442599 (cit. on p. 22).
- [76] Tatsuya Hirano and T J Mitchison. "[Topoisomerase II does not play a scaffolding role in the organization of mitotic chromosomes assembled in Xenopus egg extracts.](#)" In: *J. Cell Biol.* 120.3 (Feb. 1993), pp. 601–12. ISSN: 0021-9525. DOI: 10.1083/jcb.120.3.601 (cit. on p. 22).
- [77] Daniel Gerlich et al. "[Condensin I stabilizes chromosomes mechanically through a dynamic interaction in live cells](#)". In: *Curr. Biol.* 16.4 (Feb. 2006), pp. 333–44. ISSN: 0960-9822. DOI: 10.1016/j.cub.2005.12.040 (cit. on p. 22).
- [78] Ronald Hancock. "Packing of the polynucleosome chain in interphase chromosomes: evidence for a contribution of crowding and entropic forces." In: *Semin. Cell Dev. Biol.* 18.5 (Oct. 2007), pp. 668–75. ISSN: 1084-9521. DOI: 10.1016/j.semcdb.2007.08.006 (cit. on p. 23).
- [79] T J Century, I R Fenichel, and S B Horowitz. "[The concentrations of water, sodium and potassium in the nucleus and cytoplasm of amphibian oocytes.](#)" In: *J. Cell Sci.* 7.1 (July 1970), pp. 5–13. ISSN: 0021-9533. medline: 5476863 (cit. on p. 23).
- [80] S V Buravkov, K Zierold, and V A Shakhlamov. "Digital image mapping of water and dry mass content using ultrathin freeze-dried cryosections". In: *Bull. Exp. Biol. Med.* 116.3 (Sept. 1993), pp. 1174–1177. ISSN: 0007-4888. DOI: 10.1007/BF00820254 (cit. on p. 23).
- [81] S Päufer et al. "Estimation of water content and water mobility in the nucleus and cytoplasm of *Xenopus laevis* oocytes by NMR microscopy." In: *Magn. Reson. Imaging* 13.2 (1995), pp. 269–76. ISSN: 0730-725X. DOI: 10.1016/0730-725X(94)00109-G (cit. on p. 23).

- [82] Michael G Poirier, Tamar Monhait, and John F. Marko. “[Reversible hypercondensation and decondensation of mitotic chromosomes studied using combined chemical-micromechanical techniques](#).” In: *J. Cell Biol.* 85.2 (2002), pp. 422–34. ISSN: 0730-2312. DOI: 10.1002/jcb.10132 (cit. on p. 23).
- [83] T D Allen et al. “[The nuclear pore complex: mediator of translocation between nucleus and cytoplasm](#).” In: *J. Cell Sci.* 113 (Pt 10) (May 2000), pp. 1651–9. ISSN: 0021-9533. PMID: 10769196 (cit. on p. 23).
- [84] P L Paine, L C Moore, and S B Horowitz. “Nuclear envelope permeability.” In: *Nature* 254.5496 (Mar. 1975), pp. 109–14. ISSN: 0028-0836. DOI: 10.1038/254109a0 (cit. on p. 23).
- [85] M J Hendzel et al. “Mitosis-specific phosphorylation of histone H3 initiates primarily within pericentromeric heterochromatin during G2 and spreads in an ordered fashion coincident with mitotic chromosome condensation.” In: *Chromosoma* 106.6 (Nov. 1997), pp. 348–60. ISSN: 0009-5915. DOI: 10.1007/s004120050256 (cit. on p. 23).
- [86] Shelley L Berger. “[Histone modifications in transcriptional regulation](#).” In: *Curr. Opin. Genet. Dev.* 12.2 (Apr. 2002), pp. 142–8. ISSN: 0959-437X. DOI: 10.1016/S0959-437X(02)00279-4 (cit. on p. 23).
- [87] S. Zimmerman and A. Minton. “Macromolecular Crowding: Biochemical, Biophysical, and Physiological Consequences”. In: *Annu. Rev. Biophys. Biomol. Struct.* 22 (1993), pp. 27–65. DOI: 10.1146/annurev.bb.22.060193.000331 (cit. on p. 24).
- [88] Theo Odijk. “[Protein-Macromolecule Interactions](#)”. In: *Macromolecules* 29 (1996), pp. 1842–1843. DOI: 10.1021/ma951467a (cit. on p. 24).
- [89] L D Murphy and S. Zimmerman. “Condensation and cohesion of lambda DNA in cell extracts and other media: implications for the structure and function of DNA in prokaryotes.” In: *Biophys. Chem.* 57.1 (Dec. 1995), pp. 71–92. ISSN: 0301-4622. DOI: 10.1016/0301-4622(95)00047-2 (cit. on p. 24).
- [90] Pernette J Verschure et al. “[Condensed chromatin domains in the mammalian nucleus are accessible to large macromolecules](#).” In: *EMBO Rep.* 4.9 (Sept. 2003), pp. 861–6. ISSN: 1469-221X. DOI: doi:10.1038/sj.embor.embor922 (cit. on p. 24).
- [91] Renko de Vries. “Depletion-induced instability in protein-DNA mixtures: Influence of protein charge and size”. In: *J. Chem. Phys.* 125 (2006). DOI: 10.1063/1.2209683 (cit. on p. 24).
- [92] Theo Odijk. “Osmotic compaction of supercoiled DNA into a bacterial nucleoid.” In: *Biophys. Chem.* 73.1-2 (July 1998), pp. 23–9. ISSN: 0301-4622. DOI: 10.1016/S0301-4622(98)00115-X (cit. on p. 24).
- [93] T R Strick et al. “[Stretching of macromolecules and proteins](#)”. In: *Rep. Prog. Phys.* 66.1 (2003), pp. 1–45. DOI: 10.1088/0034-4885/66/1/201 (cit. on p. 27).

- [94] S. B. Smith, L. Finzi, and C. Bustamante. “[Direct Mechanical Measurements of the Elasticity of Single DNA Molecules by Using Magnetic Beads](#)”. In: *Science* 258.5085 (Nov. 1992), pp. 1122–1126. DOI: 10.1126/science.1439819 (cit. on p. 27).
- [95] T. R. Strick et al. “[The Elasticity of a Single Supercoiled DNA Molecule](#)”. In: *Science* 271.5257 (Mar. 1996), pp. 1835–1837. DOI: 10.1126/science.271.5257.1835 (cit. on pp. 27, 57).
- [96] Steven B. Smith, Yuija Cui, and Carlos Bustamante. “[Overstretching B-DNA: The Elastic Response of Individual Double-Stranded and Single-Stranded DNA Molecules](#)”. In: *Science* 271 (Feb. 1996), pp. 795–799. eprint: 10.1126/science.271.5250.795 (cit. on pp. 27, 58).
- [97] M D Wang et al. “[Stretching DNA with optical tweezers](#)”. In: *Biophys. J.* 72.3 (1997), pp. 1335–1346. DOI: 10.1016/S0006-3495(97)78780-0 (cit. on p. 27).
- [98] Cluzel, Philippe and Lebrun, Anne and Heller, Christoph and Lavery, Richard and Viovy, Jean-Louis and Chatenay, Didier and Caron, François. “[DNA: An Extensible Molecule](#)”. In: *Science* 271.5250 (1996), pp. 792–794. DOI: 10.1126/science.271.5250.792 (cit. on p. 27).
- [99] T. Perkins et al. “[Stretching of a Single Tethered Polymer in a Uniform Flow](#)”. In: *Science* 268 (1995), p. 83. PMID: 7701345 (cit. on p. 27).
- [100] Matthias Rief et al. “[Reversible Unfolding of Individual Titin Immunoglobulin Domains by AFM](#)”. In: *Science* 276.5315 (1997), pp. 1109–1112. DOI: 10.1126/science.276.5315.1109 (cit. on p. 27).
- [101] C. Bustamante et al. “[Entropic elasticity of lambda-phage DNA](#)”. In: *Science* 265.5178 (1994), pp. 1599–15600. DOI: 10.1126/science.8079175 (cit. on p. 27).
- [102] Alexander Vologodskii. “[DNA Extension under the Action of an External Force](#)”. In: *Macromolecules* 27.20 (1994), pp. 5623–5625. DOI: 10.1021/ma00098a016 (cit. on p. 27).
- [103] John F. Marko and Eric D. Siggia. “[Stretching DNA](#)”. In: *Macromolecules* 28.26 (1995), pp. 8759–8770. DOI: 10.1021/ma00130a008 (cit. on p. 27).
- [104] Theo Odijk. “[Stiff Chains and Filaments under Tension](#)”. In: *Macromolecules* 28.20 (1995), pp. 7016–7018. DOI: 10.1021/ma00124a044 (cit. on p. 27).
- [105] C. Bouchiat et al. “[Estimating the Persistence Length of a Worm-Like Chain Molecule from Force-Extension Measurements](#)”. In: *Biophys. J.* 76 (Jan. 1999), pp. 409–413. DOI: 10.1016/S0006-3495(99)77207-3 (cit. on p. 27).
- [106] Robijn Bruinsma and Joseph Rudnick. “[DNA-Protein Cooperative Binding through Long-Range Elastic Coupling](#)”. In: *Biophys. J.* 76.4 (1999), pp. 1725–1733. DOI: 10.1016/S0006-3495(99)77334-0 (cit. on p. 27).

- [107] Jie Yan and John F. Marko. “[Effects of DNA-distorting proteins on DNA elastic response](#)”. In: *Phys. Rev. E* 68.1, 011905 (2003), p. 11905. DOI: 10.1103/PhysRevE.68.011905 (cit. on p. 27).
- [108] Ralf Metzler, Yacov Kantor, and Mehran Kardar. “[Force-Extension Relations for Polymers with Sliding Links](#)”. In: *Phys. Rev. E* 66.2 (2002), p. 22102. DOI: 10.1103/PhysRevE.70.011915 (cit. on p. 27).
- [109] I. M. Kulić and H. Schiessel. “[DNA spools under tension](#)”. In: *Phys. Rev. Lett.* 92.22 (2004), p. 228101. DOI: 10.1103/PhysRevLett.92.228101 (cit. on p. 27).
- [110] I.M. Kulic et al. “[Apparent Persistence Length Renormalization of Bent DNA](#)”. In: *Phys. Rev. E* 72.4 (2005), p. 041905. DOI: 10.1103/PhysRevE.72.041905 (cit. on p. 27).
- [111] Marcel E. Janson and Marileen Dogterom. “[Scaling of Microtubule Force-Velocity Curves Obtained at Different Tubulin Concentrations](#)”. In: *Phys. Rev. Lett.* 92.24 (2004), pp. 2481011–2481014. DOI: 10.1103/PhysRevLett.92.248101 (cit. on pp. 27, 47).
- [112] David R. Kovar and Thomas D. Pollard. “[Insertional assembly of actin filament barbed ends in association with formins produces piconewton forces](#)”. In: *PNAS* 101.41 (Oct. 2004), pp. 14725–14730. DOI: 10.1073/pnas.0405902101 (cit. on pp. 27, 47).
- [113] M J Footer et al. “[Direct measurement of force generation by actin filament polymerization using an optical trap](#)”. In: *PNAS* 104.7 (Feb. 2007), pp. 2181–2186. DOI: 10.1073/pnas.0607052104 (cit. on p. 27).
- [114] Theo Odijk. “[Microfibrillar buckling within fibers under compression](#)”. In: *J. Chem. Phys.* 108 (1998), p. 6923. DOI: 10.1063/1.476107 (cit. on pp. 27, 30, 35).
- [115] N. C. Seeman. “DNA in a material world”. In: *Nature* 421 (2003), pp. 427–431. PMID: 12540916 (cit. on p. 28).
- [116] R. P. Goodman, R. M. Berry, and A. J. Tuberfield. “The single-step synthesis of a DNA tetrahedron”. In: *Chem. Commun.* 12 (2004), pp. 1372–1373. DOI: 10.1039/B402293A (cit. on pp. 28, 47).
- [117] P J Hagerman. “[Flexibility of DNA](#)”. In: *Annu. Rev. Biophys. Biophys. Chem.* 17.1 (1988), pp. 265–286. DOI: 10.1146/annurev.bb.17.060188.001405 (cit. on p. 29).
- [118] Theo Odijk. “[Theory of lyotropic polymer liquid crystals](#)”. In: *Macromolecules* 19.9 (1986), pp. 2313–2329. DOI: 10.1021/ma00163a001 (cit. on p. 30).
- [119] Hagen Kleinert. *Path Integrals in Quantum Mechanics, Statistics, Polymer Physics, and Financial Markets*. 3rd. World Scientific, 2002 (cit. on pp. 30, 34, 36).
- [120] Milton Abramowitz and Irene A. Stegun, eds. *Handbook of mathematical functions*. Dover, 1970 (cit. on pp. 31, 36, 115, 117–119).

- [121] A. E. H. Love. *A Treatise on the Mathematical Theory of Elasticity*. Dover, 2003 (cit. on pp. 31, 32).
- [122] I. S. Gradshteyn and I. M. Ryzhik. *Table of Integrals, Series, and Products*. Academic Press, 2000 (cit. on pp. 34, 115).
- [123] F. M. Arscott. *Periodic Differential Equations*. Vol. 66. Int. Series of Monographs in Pure and Applied Mathematics. Pergamon, 1964 (cit. on p. 36).
- [124] Michael E. Peskin and Aniel V. Schroeder. *An Introduction to Quantum Field Theory*. Westview Press, 1995 (cit. on p. 38).
- [125] I.M. Kulić et al. “[Equation of state of looped DNA](#)”. In: *Phys. Rev. E* 75.1 (2007), p. 11913. DOI: 10.1103/PhysRevE.75.011913 (cit. on pp. 40, 93, 116).
- [126] Kurt Kremer and Gary S. Grest. “Dynamics of entangled linear polymer melts: A molecular-dynamics simulation”. In: *J. Chem. Phys.* 92.8 (1990), pp. 5057–5086. DOI: 10.1063/1.458541 (cit. on p. 45).
- [127] R.B. Bird, R.C. Armstrong, and O. Hassager. *Dynamics of polymeric liquids. Vol. 1: Fluid mechanics*. John Wiley and Sons Inc., New York, NY, 1987 (cit. on p. 45).
- [128] F Gittes et al. “[Flexural Rigidity of Microtubules and Actin Filaments Measured from Thermal Fluctuations in Shape](#)”. In: *J. Cell Biol.* 120 (1993), pp. 923–934. DOI: 10.1083/jcb.120.4.923 (cit. on p. 47).
- [129] Francesco Pampaloni et al. “[Thermal fluctuations of grafted microtubules provide evidence of a length-dependent persistence length](#)”. In: *PNAS* 103.27 (July 2006), pp. 10248–10253. DOI: 10.1073/pnas.0603931103 (cit. on p. 47).
- [130] G. Călugăreanu. “[L’intégrale de Gauss et l’analyse des nœuds tridimensionnels](#)”. In: *Rev. Roum. Math. Pures Appl.* 4.5 (1959) (cit. on p. 50).
- [131] G. Călugăreanu. “[Sur les classes d’isotopie des noeuds tridimensionnels et leurs invariants](#)”. In: *Czech. Math. J.* 11.4 (1961), pp. 588–625. HDL: 10338.dmlcz/100486 (cit. on p. 50).
- [132] G. Călugăreanu. “[A theorem on tridimensional linkage of closed curves](#)”. In: *Comun. Acad. Repub. Pop. Rom.* 11.7-12 (1961), p. 829. ISSN: 0567-6371 (cit. on p. 50).
- [133] William F. Pohl. “[The self-linking number of a closed space curve](#)”. In: *J. Math. Mech.* 17 (10 1968), pp. 975–985. ISSN: 0095-9057. DOI: 10.1512/iumj.1968.17.17061 (cit. on p. 50).
- [134] James White. “[Self-linking and Gauss-integral in higher dimensions](#)”. In: *Am. J. Math.* 91.3 (1969), pp. 693–728. DOI: 10.2307/2373348 (cit. on p. 50).
- [135] J.D. Jackson. *Classical electrodynamics*. Wiley, 1999 (cit. on pp. 50, 55).
- [136] S. Edwards. “Statistical Mechanics with topological constraints: II”. In: *J. Phys. A: Math. Theor.* 1 (1968), pp. 15–28. DOI: 10.1088/0305-4470/1/1/303 (cit. on p. 51).

- [137] HK Moffatt and R.L. Ricca. “[Helicity and the Călugăreanu invariant](#)”. In: *Proc. R. Soc. A* 439.1906 (1992), p. 411. DOI: 10.1098/rspa.1992.0159 (cit. on p. 51).
- [138] M. Epple. “[Orbits of asteroids, a braid, and the first link invariant](#)”. In: *Math. Intell.* 20.1 (1998), pp. 45–52. DOI: 10.1007/BF03024400 (cit. on p. 51).
- [139] Michael Spivak. *A Comprehensive Introduction to Differential Geometry*. Vol. 3. Publish or Perish, 1999 (cit. on p. 51).
- [140] MR Dennis and JH Hannay. “[Geometry of Călugăreanu’s theorem](#)”. In: *Proc. R. Soc. A* 461.2062 (2005), p. 3245. DOI: 10.1098/rspa.2005.1527 (cit. on p. 53).
- [141] F.B. Fuller. “[Decomposition of the linking number of a closed ribbon: a problem from molecular biology](#)”. In: *PNAS* 75.8 (1978), pp. 3557–3561. eprint: 10.1073/pnas.75.8.3557 (cit. on p. 54).
- [142] J. Aldinger, I. Klapper, and M. Tabor. “[Formulae for the calculation and estimation of writhe](#)”. In: *J. Knot Theor. Ramif.* 4.3 (1995), pp. 343–372. DOI: 10.1142/S021821659500017X (cit. on p. 54).
- [143] Simon L. Altmann. *Rotations, Quaternions, and Double Groups*. Dover, 2005 (cit. on p. 55).
- [144] EL Starostin. “Physical and numerical models in knot theory: including applications to the life sciences”. In: *Series on Knots and Everything*. World Scientific Pub Co Inc, 2005. Chap. [On the writhe of non-closed curves](#). DOI: 10.1142/9789812703460_0026 (cit. on p. 56).
- [145] Scott Forth et al. “[Abrupt buckling transition observed during the plectoneme formation of individual DNA molecules](#)”. In: *Phys. Rev. Lett.* 100.14 (2008), p. 148301. DOI: 10.1103/PhysRevLett.100.148301 (cit. on pp. 57, 59, 109, 110).
- [146] JF Leger et al. “[Structural transitions of a twisted and stretched DNA molecule](#)”. In: *Phys. Rev. Lett.* 83.5 (1999), pp. 1066–1069. DOI: 10.1103/PhysRevLett.83.1066 (cit. on p. 57).
- [147] Francesco Mosconi et al. “Measurement of the Torque on a Single Stretched and Twisted DNA Using Magnetic Tweezers”. In: *Phys. Rev. Lett.* 102.7 (2009), pp. 1–4. DOI: 10.1103/PhysRevLett.102.078301 (cit. on pp. 57, 59, 109).
- [148] Prashant K Purohit. “[Plectoneme formation in twisted fluctuating rods](#)”. In: *J. Mech. Phys. Solids* 56.5 (2008), pp. 1715–1729. ISSN: 0022-5096. DOI: 10.1016/j.jmps.2007.12.008 (cit. on p. 57).
- [149] N. Clauvelin, B. Audoly, and S. Neukirch. “[Elasticity and electrostatics of plectonemic DNA](#)”. In: *Biophys. J.* 96.9 (2009), pp. 3716–3723. DOI: 10.1016/j.bpj.2009.02.032 (cit. on p. 57).

- [150] Christopher Maffeo et al. “[DNA–DNA Interactions in Tight Supercoils Are Described by a Small Effective Charge Density](#)”. In: *Phys. Rev. Lett.* 105.15 (Oct. 2010), p. 158101. DOI: 10.1103/PhysRevLett.105.158101 (cit. on pp. 57, 91, 98, 105, 109).
- [151] B.C. Daniels et al. “[Discontinuities at the DNA supercoiling transition](#)”. In: *Phys. Rev. E* 80.4 (2009), p. 40901. DOI: 10.1103/PhysRevE.80.040901 (cit. on pp. 57, 58, 91, 126).
- [152] John F Marko. “Torque and dynamics of linking number relaxation in stretched supercoiled DNA”. In: *Phys. Rev. E* 76.2 (2007). DOI: 10.1103/PhysRevE.76.021926 (cit. on pp. 57, 105).
- [153] J Ubbink and Theo Odijk. “[Electrostatic–Undulatory Theory of Plectonemically Supercoiled DNA](#)”. In: *Biophys. J.* 76.5 (1999), pp. 2502–2519. DOI: 10.1016/S0006-3495(99)77405-9 (cit. on pp. 58, 65–67, 81, 94, 125).
- [154] J. Gore et al. “[DNA overwinds when stretched](#)”. In: *Nature* 442.7104 (2006), pp. 836–839. DOI: 10.1038/nature04974 (cit. on p. 58).
- [155] M.Y. Sheinin and M.D. Wang. “[Twist–stretch coupling and phase transition during DNA supercoiling](#)”. In: *Phys. Chem. Chem. Phys.* 11.24 (2009), pp. 4800–4803. DOI: 10.1039/b901646e (cit. on pp. 58, 92).
- [156] Michel Nizette and Alain Goriely. “[Towards a classification of Euler–Kirchhoff filaments](#)”. In: *J. Math. Phys.* 40.6 (1999), pp. 2830–2866. DOI: 10.1063/1.532731 (cit. on pp. 58, 62).
- [157] T. Odijk. “Polyelectrolytes near the rod limit”. In: *J. Polym. Sci., Polym. Phys. Ed.* 15.3 (1977). DOI: 10.1002/pol.1977.180150307 (cit. on pp. 61, 67).
- [158] J. Skolnick and M. Fixman. “[Electrostatic persistence length of a wormlike polyelectrolyte](#)”. In: *Macromolecules* 10.5 (1977), pp. 944–948. DOI: 10.1021/ma60059a011 (cit. on pp. 61, 67).
- [159] GHM Van der Heijden and JMT Thompson. “Helical and localised buckling in twisted rods: A unified analysis of the symmetric case”. In: *Nonlinear Dyn.* 21.1 (2000), pp. 71–99. ISSN: 0924-090X. DOI: 10.1023/A:1008310425967 (cit. on p. 62).
- [160] T. Odijk and A.C. Houwaart. “On the theory of the excluded-volume effect of a polyelectrolyte in a 1-1 electrolyte solution”. In: *J. Polym. Sci., Polym. Phys. Ed.* 16.4 (1978). DOI: 10.1002/pol.1978.180160405 (cit. on pp. 64, 67).
- [161] AG Cherstvy. “Looping charged elastic rods: applications to protein-induced DNA loop formation”. In: *Eur. Biophys. J.* (2011), pp. 1–12. DOI: 10.1007/s00249-010-0628-5 (cit. on p. 64).

- [162] Nicolas Clauvelin, Basile Audoly, and Sebastien Neukirch. “Mechanical response of plectonemic DNA: An analytical solution”. In: *Macromolecules* 41.12 (2008), pp. 4479–4483. ISSN: 0024-9297. DOI: 10.1021/ma702713x (cit. on p. 66).
- [163] G.S. Manning. “Limiting laws and counterion condensation in polyelectrolyte solutions I. Colligative properties”. In: *J. Chem. Phys.* 51 (1969), p. 924. DOI: 10.1063/1.1672157 (cit. on p. 67).
- [164] W.J. Moore. *Basic physical chemistry*. Prentice-Hall Englewood Cliffs, New Jersey, 1983 (cit. on p. 67).
- [165] JR Philip and RA Wooding. “Solution of the Poisson–Boltzmann equation about a cylindrical particle”. In: *J. Chem. Phys.* 52 (1970), p. 953 (cit. on pp. 67, 138).
- [166] NE Hoskin and S. Levine. “The Interaction of Two Identical Spherical Colloidal Particles. II. The Free Energy”. In: *Philos. Trans. R. Soc., A* 248.951 (1956), pp. 449–466. DOI: 10.1098/rsta.1956.0005 (cit. on p. 67).
- [167] S.L. Brenner and V.A. Parsegian. “[A physical method for deriving the electrostatic interaction between rod-like polyions at all mutual angles](#)”. In: *Biophys. J.* 14.4 (1974), pp. 327–334. DOI: 10.1016/S0006-3495(74)85919-9 (cit. on p. 67).
- [168] Wei Bu, David Vaknin, and Alex Travesset. “[How Accurate Is Poisson-Boltzmann Theory for Monovalent Ions near Highly Charged Interfaces?](#)” In: *Langmuir* 22.13 (2006), pp. 5673–5681. ISSN: 0743-7463. DOI: 10.1021/la053400e (cit. on p. 69).
- [169] JR Blundell and EM Terentjev. “[Buckling of semiflexible filaments under compression](#)”. In: *Soft Matter* 5.20 (2009), pp. 4015–4020. DOI: 10.1039/B903583D (cit. on p. 69).
- [170] Theo Odijk. “The statistics and dynamics of confined or entangled stiff polymers”. In: *Macromolecules* 16.8 (1983), pp. 1340–1344. DOI: 10.1021/ma00242a015 (cit. on p. 71).
- [171] TW Burkhardt. “Free energy of a semiflexible polymer confined along an axis”. In: *J. Phys. A: Math. Theor.* 28 (1995), pp. L629–L635. DOI: 10.1088/0305-4470/28/24/001 (cit. on pp. 71, 75).
- [172] J. David Moroz and Philip Nelson. “[Entropic Elasticity of Twist-Storing Polymers](#)”. In: *Macromolecules* 31 (1998), pp. 6333–6347. DOI: 10.1021/ma971804a (cit. on pp. 71, 91–93).
- [173] J.F. Marko. “DNA under high tension: overstretching, undertwisting, and relaxation dynamics”. In: *Phys. Rev. E* 57.2 (1998), pp. 2134–2149. DOI: 10.1103/PhysRevE.57.2134 (cit. on pp. 71, 73, 91, 93, 125).
- [174] I.J. Good. “Generalizations to several variables of Lagrange’s expansion, with applications to stochastic processes”. In: *Math. Proc. Camb. Philos. Soc.* 56.4 (1960), pp. 367–380. DOI: 10.1017/S0305004100034666 (cit. on pp. 84, 85).

- [175] I.M. Gessel. “A combinatorial proof of the multivariable Lagrange inversion formula”. In: *J. Comb. Theory, Ser. A* 45.2 (1987), pp. 178–195. DOI: 10.1016/0097-3165(87)90013-6 (cit. on pp. 84, 85).
- [176] S. Neukirch. “[Extracting DNA twist rigidity from experimental supercoiling data](#)”. In: *Phys. Rev. Lett.* 93.19 (2004), p. 198107. DOI: 10.1103/PhysRevLett.93.198107 (cit. on p. 91).
- [177] Sébastien Neukirch and John F. Marko. “[Analytical Description of Extension, Torque, and Supercoiling Radius of a Stretched Twisted DNA](#)”. In: *Phys. Rev. Lett.* 106.13 (Apr. 2011), p. 138104. DOI: 10.1103/PhysRevLett.106.138104 (cit. on pp. 91, 98).
- [178] T. Odijk and J. Ubbink. “[Dimensions of a plectonemic DNA supercoil under fairly general perturbations](#)”. In: *Phys. A* 252.1-2 (1998), pp. 61–66. DOI: 10.1016/S0378-4371(97)00588-8 (cit. on p. 94).
- [179] A Crut et al. “[Fast dynamics of supercoiled DNA revealed by single-molecule experiments](#)”. In: *PNAS* 104.29 (2007), pp. 11957–11962. DOI: 10.1073/pnas.0700333104 (cit. on p. 96).
- [180] T. Strick et al. “[Twisting and stretching single DNA molecules](#)”. In: *Prog. Biophys. Mol. Biol.* 74.1-2 (2000), pp. 115–140. PMID: 11106809 (cit. on p. 105).
- [181] C. Deufel et al. “[Nanofabricated quartz cylinders for angular trapping: DNA supercoiling torque detection](#)”. In: *Nat. Methods* 4.3 (2007), pp. 223–225. DOI: 10.1038/nmeth1013 (cit. on p. 109).
- [182] F. Mosconi et al. “[Torque determination on DNA with magnetic tweezers](#)”. In: *arXiv* (2008). arXiv:0809.0621v1 [cond-mat.soft] (cit. on pp. 110–112).

List of Tables

2.1	30 nm fiber geometry	10
3.1	Buckling force reduction	48
4.1	Properties of the 3 parts of White's equation	52
8.1	Indirect torque measurements using Maxwell relations,	109

List of Figures

2.1	A 5-ribbon fiber	11
2.2	3d-FISH data	18
3.1	Force below (a) and above (b) the Euler transition.	28
3.2	Relative extension shift	41
3.3	Decrease of the buckling force in 2-d	44
3.4	Comparison with simulations	46
4.1	Writhe and twist	50
5.1	Turn extension plot	59
5.2	Plectoneme	60
5.3	Relative energies of homoclinic solutions	64
5.4	The effective charge line density as function of salt concentration	68
5.5	R^* dependence on salt concentration	68
6.1	Flow of the roots $\sqrt{\xi_i}$ in the complex plane.	78
7.1	Multi-plectoneme factor	101
7.2	Contourplot of the number of plectonemes	102
8.1	Slopes with and without thermal contributions	104
8.2	Influence of the multi-plectoneme phase on the turn extension slope.	105
8.3	Number of plectonemes at 3 pN and 20 mM salt.	106
8.4	Turns extension curves at 20 mM salt.	107
8.5	Turns extension curves at 320 mM salt.	107
8.6	Turns extension curves for a long chain.	108
8.7	Direct torque measurements with optical tweezers	110
8.8	Magnetic tweezer torque measurements	111
8.9	Indirect torque measurement	112

Samenvatting

Het onderzoek waar dit proefschrift op gebaseerd is betreft bepaalde fysische eigenschappen van biopolymeren, in het bijzonder DNA. Een polymeer is een groot molecuul opgebouwd uit kleinere eenheden, monomeren. In de gevallen die hier besproken worden zijn deze eenheden lineair als een ketting aan elkaar gekoppeld resulterend in een flexibele slang met een doorsnede van enige nanometers (10^{-9} meter), maar een macroscopische lengte die in extreme gevallen meerdere centimeters is.

De modulaire opbouw van deze moleculen zorgt voor een grote flexibiliteit. In gevallen waar de lengte snel moet kunnen veranderen is de verbinding tussen de monomeren makkelijk te verbreken. Dit is nuttig in het geval dit moleculen zijn die dienst doen als transport baan in de cel, of slechts tijdelijk nodig zijn tijdens de celdeling. Met name microtubule's, holle moleculaire cilinders, kunnen razendsnel weer worden afgebroken. Structuur gevende actine's moeten hun lengte kunnen aanpassen aan hun omgeving. DNA hoeft slechts flexibel te zijn op evolutionair niveau, maar onverstoort op korte tijd om er voor te zorgen dat de gecodeerde informatie behouden blijft.

Één ding hebben de drie genoemde moleculen gemeen ze zijn alle drie uiterst stijf over lengtes vergelijkbaar met de monomeer lengte. De richting die het molecuul in de lengte heeft is behoorlijk persistent. Om aan te geven hoe lang een richting behouden blijft spreekt men wel van de persistente lengte als schaal waarover het polymeer als recht kan worden beschouwd. Deze lengte varieert van 50 nanometer voor DNA tot wel 1000 nanometer voor microtubule's. Die stijfheid is er niet voor niks: met een stok kan je duwen, met een touw nauwelijks. Dit soort stijve polymeren worden ook wel aangeduid als semi-flexibele polymeren.

Nu zijn deze moleculen nooit geïsoleerd in het luchtledige, maar bevinden zich in een omgeving met vele kleinere moleculen, zoals water en zouten, of eiwitten die zelf ook weer polymeren zijn maar meestal stevig opgevouwen. De continue botsingen met deze andere deeltjes in de cel valt met geen mogelijkheid precies te beschrijven. Al praktisch niet vanwege het enorme aantal moleculen in een cel. Maar het is ook niet nodig gezien het soort vragen die we beantwoord willen hebben. Die vragen zijn macroscopisch van aard, aangezien onze waarnemingen dat in het algemeen zijn. De botsingen met de omringende moleculen

kunnen op tijdschalen waarop onze metingen duren gezien worden als een ongecorrleerd bombardement vanuit de omgeving. De kracht van dit bombardement, de gemiddelde snelheid waarmee de kleinere moleculen zich voortbewegen en dus botsen is de temperatuur. Dat je van zo een gemiddelde kan spreken komt omdat die deeltjes ook veelvuldig met elkaar botsen en snelheid, of beter gezegd kinetische energie, met elkaar uitwisselen totdat deze overal ongeveer hetzelfde is. Het systeem is dan in evenwicht.

Beschouw nu even voor het gemak een zeer simpel model van een polymeer waarbij de monomeren korte stokjes zijn, allemaal van dezelfde lengte, die vrij scharnierend aan elkaar verbonden zijn. De richting die een monomeer gaat is uitgaande van volledig wrijvingsloze scharnieren geheel onafhankelijk van de richting van de andere monomeren. Het pad dat zo een ideaal polymeer volgt wordt ook wel een dronkenmans loop genoemd aangezien je, sequentieel langs het polymeer gaande, elk monomeer als een volledig willekeurige stap kan zien. Gemiddeld kom je natuurlijk nergens op die manier, maar als je niet naar het gemiddelde punt kijkt maar naar de gemiddelde afstand vanaf het beginpunt zonder op de richting te letten dan is het vrij eenvoudig te laten zien dat die afstand als de wortel van het aantal stappen gaat. Men zegt wel dat de grootte van zo een polymeer, bijvoorbeeld de afstand tussen de uiteindes, schaalt als de wortel van het aantal monomeren.

Ondertussen wordt dit polymeer van alle kanten thermisch gebombardeerd. In principe komen alle mogelijke configuraties voor, ook de helemaal gestrekte. Echter na het vastleggen van de eerste stap is er slechts één configuratie die helemaal gestrekt is terwijl een afstand die precies via de schalings relatie gaat voor een lang polymeer op heel veel manieren gerealiseerd kan worden. Zou je nu het polymeer gestrekt willen houden, dan moet je kracht uitoefenen tegen dat thermisch bombardement in. Deze thermische kracht die het polymeer naar zijn evenwichts configuraties drijft heet ook wel een entropische kracht. Nu is een wat realistischer model voor een polymeer een wandeling van een dronkaard, die geen plek twee keer bezoekt: een Self Avoiding Walk (SAW). Ook daarvoor is het via een trucje makkelijk allerlei grootheden te bepalen. Het zichzelf ontwijken heeft tot gevolg dat het polymeer opzwelt.

DNA was stijf tot aan de persistentie lengte. Als het molecuul lang genoeg is kan het beschreven worden als een ideaal polymeer met monomeren die lang maar dun zijn. In hoofdstuk 2 wordt uitgelegd hoe dat lange molecuul enigszins geordend in de kleine celkern van een mens kan zitten zonder dat het een grote wirwar wordt. Veel is vooralsnog onduidelijk. Er is waarschijnlijk een organisatie van het DNA op iets grotere schaal door middel van een zogenaamde 30 nm vezel, ook wel Chromatine genoemd. Hoewel deze vezel wel netjes in laboratoria geconstrueerd kan worden, is het helemaal niet zo zeker dat zo een nette structuur ook in de celkern aanwezig is. Op grotere schaal wordt een link gelegd met hoe een SAW zich in de celkern zou verdelen, maar het blijkt dat daar niet veel conclusies uit getrokken kunnen worden. Hoewel je de verdeling gedeeltelijk daarmee kan beschrijven is het onwaarschijnlijk dat zo een evenwichts statistiek echt kan gelden. Dit voornamelijk om dat er te weinig bewegingsruimte is om geheel in evenwicht te komen binnen een redelijke tijd. Helaas zijn

de meeste meetmethodes tamelijk destructief en hebben de neiging structuren te creëren of te vervormen zonder dat je daar controle over hebt.

In hoofdstuk 3 bekijken we de invloed van thermische fluctuaties op semi-flexibele polymeren die korter zijn dan hun persistentie lengte. Zonder de invloed van temperatuur kan je in de lengte richting van een elastische staaf kracht zetten tot aan een bepaalde waarde die afhangt van het materiaal en de lengte van de staaf. Daarna knikt de staaf. Deze knik overgang werd al door de Zwitserse wiskundige Leonhard Euler gevonden in de 18e eeuw. Bij een macroscopische stok zullen thermische fluctuaties niet veel veranderen aan deze knikkraft. Dit is anders bij biopolymeren aangezien daar de energieschaal veel dichter bij de thermische energie ligt. Mathematisch is het gebruikelijk een flexibele staaf als een ééndimensionale curve te beschouwen met een boete op buigen, uitgedrukt in een energie. Dit is een effectieve manier om de weerstand tegen buiging, die uiteindelijk een driedimensionale oorsprong heeft in een bruikbare formule te vertalen.

De Russische fysicus Landau heeft laten zien dat deze knik overgang verdwijnt bij eindige temperatuur. Er blijven desalniettemin signalen van een overgang aanwezig die je in experimenten als een overgang zou kunnen zien. Als redelijke keuze is de helling van de druk versus extensie curve gekozen die van karakter verandert bij een kracht die lager wordt bij toenemende temperatuur. Een andere interessante ontdekking is de toename van de extensie als gevolg van thermische fluctuaties bij krachten boven de knik overgang in twee dimensies. Het molecuul lijkt als het ware stijver te worden bij hogere temperatuur. Twee dimensies lijkt wat theoretisch maar in veel experimenten zit het polymeer opgesloten tussen twee glasplaten, daarbij een twee dimensionale geometrie realiserend.

Gecompliceerder wordt het verhaal wanneer torsie in het spel komt. Aangezien DNA (net als Actine overigens) op een natuurlijke wijze gedraaid is, de befaamde dubbele helix, is het duidelijk dat torsie een rol van betekenis speelt bij functies die DNA heeft als databank en het doorgeven van de gegevens die daarin zijn opgenomen. Bij transcriptie, het uitlezen van de 4 cijferige DNA code door een structureel nauw aan DNA gerelateerd boodschapper RNA dat zelf weer als blauwdruk fungeert voor de eiwitten die de meeste processen in ons lichaam controleren, moet de dubbele helix worden opengebrouwen. Dit veroorzaakt en kan gefaciliteerd worden door torsie langs de as van het molecuul. Nog heftiger is de duplicatie van DNA bij celdeling waar de twee helices uit elkaar worden getrokken. De fysica die hiermee gepaard gaat is echter aanzienlijk lastiger op het moment de torsie boven een bepaalde grens uitkomt. Bij lagere torsie en eindige spanning is het nog met middelen zoals die gebruikt zijn in hoofdstuk 3 redelijk te berekenen. Boven een zekere hoeveelheid twist in de keten, die in experimenten expliciet als draaiingen van het uiteinde van het molecuul worden toegevoegd, verandert de baan van het molecuul van een rechte keten in een opzij uitslingerende helix boven op de natuurlijke dubbel helix. Dit effect kent iedereen wel van de bedrading die tussen hoorn en toestel van een ouderwetse telefoon lopen. Deze is altijd in de war en maakt de meest onhandige slingeringen, plectonemen genaamd, die er trekkend niet uit te halen zijn. Een ware superkluwe! In Afbeelding 4.1 is aangegeven hoe je kan overgaan van een locale verdraaiing van de keten naar een draai die in het pad van de keten zelf zit. Dat

laatste kost ook energie maar het groeit slechts lineair met het aantal verdraaiingen, terwijl de locale verdraaiingen een kwadratisch verloop vertonen.

De rest van het proefschrift is een analyse van alle facetten die een rol spelen bij de vorming van deze plectonemen. Hierbij moet worden opgemerkt dat in de vele experimenten plectonemen niet, of met grote moeite, kunnen worden waargenomen. De waarneming waaraan de theorie getoetst dient te worden bestaat slechts uit de extensie, afhankelijk van het aantal draaiingen. Aangezien er zich interacties voordoen die niet meer lokaal zijn namelijk tussen de molecuul delen die het plectoneem vormen, ontkomen we aan het bovengenoemde vonnis van Landau. Een precieze analyse van met name de thermische fluctuaties laat zien dat er onder bijzondere omstandigheden niet één, maar vele plectonemen tevoorschijn komen. Een verrassend resultaat dat tegelijkertijd verklaart waarom het zo lastig is geweest om tot nu toe een goed model te produceren.

Publications

1. master thesis: Calculation of threepoint functions of chiral primaries in a symmetric orbifold <http://staff.science.uva.nl/~jdeboer/education/projects/projects/threep.pdf>
2. Emanuel, M. and Mohrbach, H. and Sayar, M. and Schiessel, H. and Kulic, I.M. Buckling of stiff polymers: Influence of thermal fluctuations Phys. Rev. E 76 2007
3. Emanuel, M. and Radja, N.H. and Henriksson, A. and Schiessel, H. The physics behind the larger scale organization of DNA in eukaryotes Phys. Biol. 6 2009
4. Emanuel, M. and Lanzani, G. and Schiessel H. Multi-plectoneme phase of double-stranded DNA under torsion , submitted 2012

Curriculum Vitae

Ik ben geboren in Den Haag op 9 mei 1958. Na anderhalf jaar op het gymnasium Haganum te hebben gezeten, verhuisden wij naar Parijs, waar ik een jaar op de internationale school in Saint-Germain-en-Laye zat. Teruggekomen naar Den Haag vervolgde ik mijn middelbare schooltijd op het 2e vrijzinnig christelijk lyceum, waar ik in 1976 eindexamen deed. In datzelfde jaar begon ik in de herfst een studie natuurkunde aan de universiteit Leiden, richting N4, een combinatie van natuurkunde scheikunde en wiskunde. Na het behalen van mijn kandidaats sloot ik mij voor korte tijd aan bij de vakgroep fysische chemie, waar een enthousiaste promovendus, Theo Odijk, de wereld aan het bestormen was. Toen deze onverwachts tijdelijk uitviel en ik geveld werd door een griep complicatie, besloot ik mij meer fysiek door het leven te begeven. Toen mijn toenmalige vriendin, en latere echtgenote, haar studie natuurkunde aan de VU in Amsterdam had afgerond verhuisden wij naar Finland waar wij de boerderij van haar ouders in Sammaljoki (200 inwonenden) overnamen. Ik had intussen al enige jaren ervaring met het akker/bosbouw bedrijf en na een korte opleiding aan de Ahlman landbouwschool van Tampere legde ik mij toe op het beheer van de boerderij. Daarnaast werd ik voorzitter van de plaatselijke landbouwvereniging.

Met name de toetreding tot de Europese Unie in de 1996 en de hiermee samenhangende financiële afhankelijkheid van Brussel deden mij uitzien naar een verandering van werkomgeving. Bij toeval belandde ik bij het instituut voor theoretische natuurkunde van de universiteit van Amsterdam, waar ik gesterkt door een kennismakingsgesprek besloot ik in Januari 2003 een master te beginnen. Na 2 weken, bleek dat ik verrassend weinig vergeten was en aangespoord door een van de spannendste colleges die ik ooit gevolgd heb, bij prof. dr. N.P. Landsman, in eerste instantie gepolst of ik bij mathematische fysica eventueel een promotie plek zou kunnen krijgen. De vooruitzichten waren in verband met de toen nog gevoerde politiek door het FOM echter verre van rooskleurig en daarom besloten mijn masters thesis te schrijven in een groep die een theorie bestudeerde waar ik nog nooit van gehoord had. In Augustus 2005 behaalde ik cum laude mijn masters onder supervisie van prof. dr. J. de Boer met een thesis getiteld “Calculation of threepoint functions of chiral primaries in a symmetric orbifold”

Het omzeilen van de starheid van het toenmalige FOM lukte met hulp van prof. dr. B. Nienhuis die mij in contact bracht met de verse hoogleraar in de biofysica aan het instituut Lorents prof. dr. H. Schiessel die mij met geld van de Universiteit Leiden een promotie plaats aanbood, waarvan hier het resultaat. Tijdens mijn promotie heb ik een zomerschool biofysica van een maand gevolgd in Boulder en een zomerschool van 2 weken in Cargese, Corsica naast de standaard twee keer drstp scholen en twee cursussen georganiseerd door de Casimir researchschool. In het begin van mijn promotie ben ik samen met mijn collega Timon Idema een werkgroep mathematische fysica begonnen die echter in schoonheid gestorven is. Als onderwijstaak heb ik prof. dr. H. Schiessel bijgestaan bij zijn college Statistische fysica voor masterstudenten, daarbij zelf 2 maal het college voorbereid en gegeven. Ik heb verscheidene malen een lezing gegeven tijdens meetings of congressen, 2 keer als stand in voor prof. dr. T. Odijk bij het ICTP in Triest en voor de KNAW in Amsterdam. Over de tweede helft van mijn proefschrift heb ik een lezing gegeven tijdens een SECAM conferentie in Lyon.

Inmiddels ben ik sinds anderhalf jaar verbonden aan het Theoretical Soft Matter and Biophysics Institute of Complex Systems, Forschungszentrum Jülich te Jülich, Duitsland

Dankwoord

Het onredelijke van een dankwoord zit meestal in de personen die ongewild niet genoemd zijn. Het lijkt me dan ook toepasselijk in eerste instantie mijn dank uit te spreken aan de niet met name genoemden. De aangesprokenen weten dat ze dat zijn. Mijn carrière is ontegenzeggelijk enigszins grillig geweest. Ik besef dat heel goed zonder ergens spijt van te hebben. Ik heb het geluk gehad vele bijzondere personen ontmoet te hebben maar ik wil dit dankwoord in eerste instantie beperken tot degene die van invloed zijn geweest op de totstandkoming van dit proefschrift.

Ten eerste natuurlijk Helmut Schiessel, die de gok nam om mij als promovendus aan te nemen en niet alleen een goede leermeester is geweest, maar ook een goede vriend. Geduldig en behulpzaam. Een groot aandeel in de totstandkoming van dit proefschrift heeft Theo Odijk met wie ik na ongeveer 25 jaar geheel onverwacht opnieuw het levenspad kruiste. Zijn inzichten, originaliteit en kennis zijn van onschatbare waarde geweest. De bijna wekelijkse koffie en/of Thai bij Theo leverde meer op dan de meeste andere dagen. Aan Jan de Boer heb ik te danken dat ik mijn masters begonnen ben, nonchalant achterover leunend “dan doe je toch gewoon je master”. Daarnaast fungeerde hij als masterthesis begeleider met een directheid die ik graag mag. Dankzij de inspirerende colleges van Klaas Landsman begon ik de studie direct leuk te vinden. Zijn colleges slepen je mee op een niveau dat je steeds net kan vastgrijpen en dat is niet alleen mijn opvatting. Er zijn niet veel anderen die een semester lang college kunnen geven om één stelling (Gelfand-Naimark) te bewijzen op een manier waarbij elke zitting een avontuur op zich was. Mijn hartelijke dank gaat natuurlijk ook uit naar Bernard Nienhuis, aan wiens inzet ik mijn promotieplaats te danken had en aan Gerhard Gompper die voor de rust gezorgd heeft om het ook daadwerkelijk af te ronden.

Een belangrijke pijler voor een wetenschappelijke scholing is het contact met je collegas. Veel baat heb ik gehad aan intensieve interactie met Martin, Nima, Peter en Giovanni. A special thanks to Ralf Seidel, without his extensive measurements half of the thesis would not have been written. The extensive correspondence sharpened my view on plectoneme formation.

Organisatorisch verloopt een promotie onderzoek op het Lorentz zo soepel dat je nauwelijks in de gaten hebt dat dat te danken is aan de inspanningen van Fran Ouwerkerk en Marianne

Gouw, die ernaast zorg voor dragen dat elke dag op het instituut een aangename is. Mijn oprechte dank.

De tijd van een promotie is zeer intensief en vergt veel van je omgeving, diezelfde omgeving geeft je ook steun. In eerste plaats dank aan mijn dochters, Verna en Laila wiens beider ongecompliceerd optimisme een grote drijfveer is geweest, ook natuurlijk aan mijn bijna zonen Bram en Daan met liefde . Mijn ouders wiens raad consequent in de wind werd geslagen, maar niettemin het volste vertrouwen in mij bleven houden, Miret en Kere met wie het contact door tijdgebrek te veel ontbrak, aan Kaarina en Ruth: zelfs van drie dagen fietsen in de regen in Noorwegen blijven mooie herinneringen over en last but not least Adriana, optimistisch ondanks een hard niet benijdenswaardig verleden, als steun en toeverlaat.

Rauha, rauha, rauha, rauha, rantarauha

Näin huutaa pääni hädissään mutta jalat vie ja taas mennään

— Hassisen Kone: “Levottomat jalat”